12-3-2014

Using Leaf-off LiDAR in Modeling Forest Canopy Structure and Assessing the Effect of Spatial Resolution in Landscape Analyses

Jason R. Parent
University of Connecticut - Storrs, jason.parent@uconn.edu

Using Leaf-off LiDAR in Modeling Forest Canopy Structure and Assessing the Effect of Spatial Resolution in Landscape Analyses

Jason Richard Parent, Ph.D.
University of Connecticut, 2014

Abstract

In recent years, the increasing availability of airborne Light Detection and Ranging (LiDAR) has allowed landscapes to be studied in unprecedented detail. These data are primarily acquired during leaf-off canopy conditions because it is optimal for modeling the bare earth terrain in deciduous forests. However, there has been limited research investigating the utility of leaf-off data for modeling forest canopy structure and land cover. Furthermore, given the far greater spatial and temporal abundance of moderate- and coarse-resolution remote sensing data, it would be advantageous to determine when coarser data can serve as a useful proxy for finer data in landscape analyses. Thus, the objectives of this dissertation were to examine existing and novel methods to use leaf-off LiDAR data in modeling forest canopy height, canopy closure, and land cover. For each of these objectives, the ability of coarser resolution data to predict high-resolution data was investigated. This research contributes to the field of remote sensing and landscape ecology by: 1) demonstrating that leaf-off LiDAR is effective in modeling canopy height for the variety of tree species common to temperate deciduous forests in the northeastern United States; 2) developing a novel technique that is the first to successfully model canopy closure in a deciduous forest; 3) developing the first fully automated algorithm capable of accurately classifying spatially high resolution land cover across a large geographic extent (i.e. eastern Connecticut); and 4) demonstrating that moderate-resolution Landsat-based data can serve as a good proxy for high resolution data in predicting land cover areas given a sufficiently large analysis window.

Using Leaf-off LiDAR in Modeling Forest Canopy Structure and Assessing the Effect of Spatial Resolution in Landscape Analyses

Jason Richard Parent

B.S., University of Connecticut, 2002

M.S., University of Connecticut, 2006

A Dissertation

Submitted in Partial Fulfillment of the

Requirements for the Degree of

Doctor of Philosophy

at the

University of Connecticut

2014

APPROVAL PAGE

Doctor of Philosophy Dissertation

Using Leaf-off LiDAR in Modeling Forest Canopy Structure and Assessing the Effect of Spatial Resolution in Landscape Analyses

Presented by

Jason Richard Parent, B.S., M.S.

Major Advisor _____
John C. Volin

Associate Advisor _____
Daniel L. Civco

Associate Advisor _____
John A. Silander

Associate Advisor _____
Chadwick D. Rittenhouse

Associate Advisor _____
Thomas E. Worthley

University of Connecticut
2014

ACKNOWLEDGEMENTS

I would like to thank the people and organizations that assisted me in the completion of this dissertation. My primary advisor, John Volin, helped guide my research and found the financial support needed for me to pursue my PhD. My co-advisors, Daniel Civco, Chadwick Rittenhouse, Tom Worthley, and John Silander generously donated their time and ideas to help improve the quality of my dissertation. Qian Lei deserves special thanks for providing valuable insights in developing my models and analyzing my data as well as leading the survey crew that collected the majority of the field data used in my research. I also thank the many people involved in collecting the field data needed for this research. Lindsay Dreiss, Jinwon Chung, and Thomas Meyer donated data from their field projects which greatly enhanced the quality of my validation data. Much of my field data was collected by the 2013 Stormwise field crew which included Qian Lei, Bojan Bojic, Elliot Olivas, Michael Heyn, Kyle Arvisais, Mathew Solmo, Gabe Sipson, Malcom Smith, Lindsay Chateauvert, and Michael Kelly. Funding for my PhD was provided by a fellowship from the UConn Graduate School, the Storrs Agricultural Experiment Station, a department teaching assistantship, and Northeast Utilities. Thanks to Mark Rudnicki for hiring me on the Stormwise project which provided my final three semesters of funding as well as made it possible to collect much of the field data used in my research.

TABLE OF CONTENTS

Chapter 1: Introduction

1-1. Overview

The continuous improvements in remote sensing technology, over the past few decades, have provided an increasingly detailed view of our landscapes. Airborne light detection and ranging (LiDAR), in particular, provides ecologists with information on forest structure that is unprecedented in both detail and extent. In addition, aerial imagery is now routinely collected which provides data across large areas that are capable of discerning features that are a fraction of a meter across. Advances in remote sensing technology, however, have outpaced the ability of ecologists and land managers to utilize fully this vast data resource. In addition, high-resolution data remain costly and significant challenges remain in terms of processing the data to derive useful products. Furthermore, the need for high-resolution data continues to be explored as new metrics are developed and applied in landscape analyses.

High-resolution sensors generate large amounts of data, which can be difficult to process over large areas using techniques developed for moderate resolution data. These high-resolution datasets are typically processed in smaller subsets in order to be manageable for conventional computers and software. In some cases a dataset may be divided into several thousand subsets for efficient processing. The processing can be further complicated because standard image processing software and methods for deriving land cover maps and other products from remote sensing data tend to require some level of human interpretation. In addition, software typically used by landscape researchers is not capable of processing LiDAR datasets covering large areas. New approaches are needed for processing both LiDAR and aerial imagery, which can be

automated using common GIS software. To address these needs, the first goal of this research is to develop methods of processing LiDAR and image data which can be automated using scripts.

The availability of high-resolution data has steadily increased in recent years; however, the relatively high cost of acquiring these data is likely to ensure that they continue to remain limited both temporally and spatially for the foreseeable future. Fortunately, remote sensing data collected by state or federal agencies are often made available to researchers. However, these data may be collected and optimized to meet a specific program need. LiDAR data, for example, are often collected by transportation departments, Army Corps of Engineers, or the Natural Resources Conservation Service for the primary purpose of modeling topography. LiDAR data collected for this purpose are acquired during leaf-off conditions and tend to have only low to moderate point densities. Thus, these data may not be ideal for modeling a forest canopy and the limitations of the data would need to be identified and possibly mitigated. The ability to use data, such as leaf-off LiDAR, for multiple applications would be extremely beneficial in helping to address the limited availability of these data. Therefore, a second goal of this research is to evaluate the potential of moderate-resolution leaf-off LiDAR to model forest canopy structure by testing conventional and novel metrics.

The limited availability and challenges of processing high-resolution data require that the needs for the data are justified. A great deal of research has investigated the effect of grain size on landscape analyses and has found that the results of such analyses tend to behave in predictable ways as the spatial resolution of the input data are reduced. In land cover analyses, for example, the less common features tend to be lost and common features tend to become more dominant as the spatial resolution of the data is reduced. However, the ability of low or moderate resolution data to suffice depends on the analysis and objectives of the research. Thus, as new

landscape or forest canopy metrics are developed, it is prudent to assess how a particular metric is affected by spatial resolution. Thus, the third goal of this research is to assess the influence of spatial resolution on the effectiveness of metrics developed in this research as well as in recently published work.

1-2. Description of datasets

1-2.1. Light Detection and Ranging (LiDAR)

Airborne LiDAR uses laser pulses to measure distances from an airborne sensor to the ground and features on the ground surface in order to provide a three-dimensional representation of the landscape. Data are recorded when significant amounts of energy are reflected off surface features and returned to the sensor. These "returns" are stored as point data containing various attributes including horizontal coordinates, elevation, return intensity, and return number. Each laser pulse has the potential to generate multiple returns, which occurs when the beam intercepts porous structures, i.e. vegetation. Only a portion of the beam is reflected for a given return while the remaining energy penetrates deeper into the vegetation canopy. Data providers typically use commercial or proprietary software to designate returns as ground, unclassified, noise, or water. LiDAR data may be used to model bare-earth or surface feature elevations and return characteristics (e.g. intensity, number of returns per pulse, etc.) can be strongly indicative of certain land cover features.

LiDAR data are most frequently used to create Digital Elevation Models (DEM) of the bare-earth surface and this was the primary purpose of the dataset that is used in this dissertation research (Dewberry 2011). These data were collected for the Natural Resources Conservation Service (NRCS) during leaf-off conditions in November 2010 (Dewberry 2011). Leaf-off

acquisition is ideal for creating DEM's since laser pulses are more likely to reach the ground surface as compared to when canopies are in full leaf. The dataset has an average density of approximately 1.5 points / m^2 and up to four returns are recorded for a given laser pulse. The dataset is considered "small footprint" LiDAR with a laser footprint diameter of approximately 0.5 meters. The data cover nearly all of Connecticut east of the Connecticut River excluding areas along the river floodplain and along the coast. The data provider created a 1-meter resolution bare-earth DEM with an estimated vertical accuracy of 9 cm in unvegetated terrain and 21 cm in forested terrain (Dewberry 2011).

1-2.2. Multispectral imagery

Land cover classification has traditionally been performed using multi-band imagery containing brightness information for the visible and infrared spectra. These images are collected via aircraft or satellite with a sensor that measures solar energy reflected off surface features. Certain land cover features have characteristic spectral signatures that may be used in their identification from the images. Vegetation, for example, is characterized by high reflectance in the near-infrared (NIR) and relatively low reflectance in the red wavelengths (Campbell and Wynne 2011). The Normalized Difference Vegetation Index (NDVI) makes use of this characteristic and is a highly effective tool in identifying vegetation (Tucker 1979). Classification of land cover from multi-spectral imagery is complicated by the presence of clouds, shadows, and land cover types that overlap in their spectral properties. These issues can be particularly problematic for the classification of high-resolution imagery.

This dissertation research uses Connecticut's 2012 multispectral orthophotos which have a spatial resolution of 0.3 meters. The imagery contains four spectral bands including blue,

green, red, and NIR. The data were acquired, for the entire state, during leaf-off conditions in the spring of 2012 and are particularly useful for identifying surface features under tree canopies.

1-2.3. Landsat-based land cover datasets

This research utilizes two land cover datasets based on Landsat satellite imagery: 1) the National Land Cover Database (NLCD) 2011 land cover[1] and 2) the Connecticut's Changing Landscape (CCL) 2010 land cover[2]. Both datasets have a 30-meter spatial resolution. The NLCD land cover includes the entire United States whereas the CCL land cover is specific to Connecticut. The CCL dataset has been augmented by ancillary data including road vector data that have been imbedded in the land cover.

1-3. Objectives and justification:

The proposed research has three broad objectives: 1) to overcome technical challenges in utilizing high-resolution remote sensing data in landscape analyses, 2) develop new metrics and applications for these data, and 3) assess the effect of spatial resolution on these new metrics. This research focuses on applications involving airborne LiDAR data including modeling of forest canopy structure and land cover mapping. The specific objectives of this research are to:

1. evaluate models of forest canopy height derived from leaf-off LiDAR and assess the effect of LiDAR spatial resolution on model performance;
2. develop and evaluate models of forest canopy closure derived from leaf-off LiDAR and assess the effect of LiDAR spatial resolution on model performance;

[1] Developed by the Multi-Resolution Land Characteristics Consortium. Data acquired from http://www.mrlc.gov/nlcd2011.php on August 18, 2014.
[2] Developed by the Center for Land Use Education and Research. Data acquired from http://clear.uconn.edu/Projects/landscape/index.htm on August 18, 2014.

3. develop and evaluate an automated approach for deriving 1-meter resolution land cover information using LiDAR and high-resolution orthophotos; and,
4. assess the impact of land cover spatial resolution on a selection of common landscape metrics (e.g. land cover fraction, average patch size, etc.).

The first two objectives of this research focus on modeling forest canopy structure. Measurements of forest canopy characteristics have important uses in forest research and management. The structure of a forest canopy strongly influences the ecological processes occurring in the understory, such as through its influence on understory light availability (Dreiss and Volin 2013; Canham et al. 1994; Pacala et al. 1994). In addition, canopy characteristics are correlated with forest biomass, tree density, habitat quality, and other stand conditions (Smith et al. 2008). Canopy height and closure are metrics commonly used in forest research; however, field techniques for measuring canopy height and closure have limitations that make it difficult to collect accurately large numbers of field observations. Heights are difficult to measure for leaning trees or for trees where the top of the crown is not easily visible. Canopy closure requires the use of hemispherical photography or quantum sensors that are best used under diffuse light conditions which occur at dawn, dusk, or under uniformly overcast skies (Anderson 1964; Rich 1989; Whitmore et al. 1993). While leaf-on LiDAR has been used in recent years to provide continuous and accurate information on canopy structure, research on the use of leaf-off LiDAR in this regard has been limited. Leaf-off LiDAR are optimal for modeling terrain which is one of the primary applications of LiDAR. Thus, leaf-off LiDAR are much more widely available than leaf-on data and leveraging these data for forest structure research would be highly advantageous. This research focuses on the use of leaf-off LiDAR to model canopy structure because these data comprise the majority of LiDAR datasets available.

The third and fourth objectives of this research focus on land cover mapping and the effects of land cover spatial resolution on landscape analyses. Data on land cover tend to be the backbone of landscape analyses with numerous uses including biodiversity conservation, natural resource management, climate and hydrological modeling, and environmental protection (Yu et al. 2014) as well as storm water management (Arnold and Gibbons, 1996; Booth et al. 2002) and urban planning (Angel et al. 2012, Angel et al. 2011). Land cover data are typically derived from moderate-resolution satellite imagery (Yu et al. 2014); however, an appropriate spatial resolution of the land cover data is necessary to depict all features that are relevant to a particular study and insufficient detail in the land cover data could invalidate the results. This research develops an algorithm for creating a 1-meter resolution 8-class land cover map which is fully automated and feasible to apply across large areas. These data depict buildings and other anthropogenic features and should provide opportunities for future research that is not possible with any previously existing land cover data. Furthermore, we use the 1-meter land cover data to provide insights into the effect that spatial resolution has on landscape metrics and to help assess whether metrics derived from coarse resolution land cover can successfully predict metrics derived from fine resolution data.

1-4. References

Anderson, M.C. (1964). Light Relations of Terrestrial Plant Communities and Their Measurement. Biological Reviews, 39(4), 425-481.

Angel, S., J. Parent, and D.L. Civco. 2010. Ten Compactness Properties of Circles: A Unified Theoretical Foundation for the Practical Measurement of Compactness. *Canadian Geographer*. Volume 54 (4), 441-461.

Angel, S., J. Parent, D.L. Civco, A.M. Blei. 2011. The Dimensions of Global Urban Expansion: Estimates and Projections for All Countries, 2000-2050. *Progress in Planning*. 75(2): 53-108.

Angel, S., J. Parent, D.L. Civco. 2012. The Fragmentation of Urban Landscapes: Global Evidence of a Key Attribute of the Spatial Structure of Cities, 1990-2000. *Environment and Urbanization* 24(1): 249-283.

Arnold, C.L., and C.J. Gibbons. 1996. Impervious surface coverage: the emergence of a key environmental indicator. Journal of the American Planning Association 62: 243-258.

Azuma, D.L. and E. Hanson. (2002). Compilation procedures for the western Oregon inventory, 1997. Unpublished Report on file at the Portland Forestry Sciences Lab, USDA Forest Service Pacific Northwest Research Station, 620 SW Main St., Suite 400, Portland, OR, 97205, 223 pp.

Brandtberg T, Warner TA, Landenberger RE, McGraw JB. (2003). Detection and analysis of individual leaf-off tree crowns in small footprint, high sampling density lidar data from the eastern deciduous forest in North America. Remote Sensing of Environment, 85: 290–303.

Booth, D.B., Hartley, D., and R. Jackson. 2002. Forest cover, impervious-surface area, and the mitigation of stormwater impacts. Journal of the American Water Resources Association 38 (3): 835-845.

Campbell, J.B. and R.H. Wynne. (2011). Introduction to Remote Sensing (Fifth Edition). The Guilford Press. New York, NY. p.483-484.

Canham C.D., A.C. Finzi, S.W. Pacala, D.H. Burbank. (1994). Causes and consequences of resource heterogeneity in forests: interspecific variation in light transmission by canopy trees. Canadian Journal of Forest Research, 24, 337–349.

Canham, C.D., J.S. Denslow, W.J. Platt, J.R. Runkle, T.A. Spies, P.S. White. (1990). Light regimes beneath closed canopies and tree-fall gaps in temperate and tropical forests. Canadian Journal of Forest Research, 20, 620–631.

Cross, A.M., D.C. Mason, and S.J. Drury. 1988, Segmentation of remotely sensed images by a split-and-merge process. International Journal of Remote Sensing, 9, 1329–1345.

Dewberry. (2011). Project Report for the U.S. Corp of Engineers High Resolution LiDAR Acquisition & Processing for Portions of Connecticut. USACE Contract W912P9-10-D-0534. Prepared by Dewberry. 71 pp.

Dreiss, L.M. and J.C. Volin. (2013). Influence of leaf phenology and site nitrogen on invasive species establishment in temperate deciduous forest understories. Forest Ecology and Management 296: 1-8.

Englund, S.R., O'Brien, J.J., Clark, D.B. (2000). Evaluation of digital and film hemispherical photography and spherical densiometry for measuring forest light environments. Canadian Journal of Forest Research, 30, 1999–2005.

Graham, Lewis. 2012. LIDAR Best Practices: Part VI – Object Classification. LIDAR News. http://www.lidarnews.com/content/view/9130/136/. Accessed on January 28, 2013.

Finney, M. (1998). Farsite: Fire area simulator-model development and evaluation. USDA Forest Service Research Paper RMRS-RP-4.

Hopkinson, C. and L.E. Chasmer. (2009). Testing LiDAR models of fractional cover across multiple forest ecozones. Remote Sensing of Environment, 113: 275-288.

Hopkinson, C. and L.E. Chasmer. 2007. Modelling Canopy Gap Fraction from Lidar Intensity. ISPRS Workshop on Laser Scanning. Finland. September 12-14, 2007.

Jennings S.B., Brown N.D., Sheil D. (1999). Assessing forest canopies and understory illumination: canopy closure, canopy cover and other measures. Forestry, 72(1), 59-74.

Kamusoko, C. and M. Aniya. 2009. Hybrid classification of Landsat data and GIS for land use/cover change analysis of the Bindura district, Zimbabwe. International Journal of Remote Sensing 30(1): 97-115.

Korhonen, L., I. Korpela, J. Heiskanen, M. Maltamo. (2011). Airborne discrete-return LiDAR data in the estimation of vertical canopy cover, angular canopy closure and leaf area index. Remote Sensing of Environment, 115: 1065-1080

Korhonen, L., Korhonen, K. T., Rautiainen, M., & Stenberg, P. (2006). Estimation of Forest Canopy Cover : a Comparison of Field Measurement Techniques, *40*(4), 577–588.

Lefsky, M. A., W.B. Cohen, S.A. Acker, G.G. Parker, T.A. Spies, D. Harding. (1999). LiDAR remote sensing of the canopy structure and biophysical properties of Douglas-fir Western hemlock forests. Remote Sensing of Environment, 70, 339-361.

Lieffers, V.J., Messier, C., Stadt, K.J., Gendron, F., Comeau, P.G. (1999). Predicting and managing light in the understory of boreal forests. Canadian Journal of Forest Research, 29, 796–811.

Lillesand, T.M. and Kiefer, R.W. 2000. Remote Sensing and Digital Image Interpretation, Wiley, New York, 724 p.

Morsdorf, F., B. Kötz, E. Meier, K. I. Itten, B. Allgöwer. (2006). Estimation of LAI and fractional cover from small footprint airborne laser scanning data based on gap fraction. Remote Sensing of Environment, 104: 50-61.

Naesset, E. (2005). Assessing sensor effects and effects of leaf-off and leaf-on canopy conditions on biophysical stand properties derived from small-footprint airborne laser data. Remote Sensing of Environment, 98: 356-370.

Nelson, R., W. Krabill, and G. Maclean. (1984). Determining forest canopy characteristics using airborne laser data. Remote Sensing of Environment, 15(3), 201-212.

Orka, H.O., E. Naesset, and O.M. Bollandsas. (2010). Effects of different sensors and leaf-on and leaf-off canopy conditions on echo distributions and individual tree properties derived from airborne laser scanning. Remote Sensing of Environment, 114: 1445-1461.

Pacala S, C. Canham, J. Silander, R. Kobe. (1994). Sapling growth as a function of resources in a north temperate forest. Canadian Journal of Forest Research, 24: 2172–2183.

Reynolds, R.T., R.T. Graham, M.H. Reiser, R.L. Bassett, P.L. Kennedy, D.A. Boyce Jr., G. Goodwin, R. Smith, E.L. Fisher. (1992). Management Recommendations for the Northern Goshawk in the Southwestern United States. USDA Forest Service General Technical Report RM-217.

Riaño, D., F. Valladares, S. Condes, E. Chuvieco. (2004). Estimation of leaf area index and covered ground from airborne laser scanner (LiDAR) in two contrasting forests. Agricultural and Forest Meteorology, 124: 269−275.

Rich, P.M. (1989). A Manual for Analysis of Hemispherical Canopy Photography. Los Alamos National Laboratory. 80p.

Sang, Weiguo; Sha Chen; Guangqi Li . (2008). Dynamic of leaf area index and canopy openness of three forest types in a warm temperate zone. Frontiers of Forestry in China, 6: 416-421.

Simova, P. and K. Gdulova. 2012. Landscape indices behavior: A review of scale effects. Applied Geography 34: 385-394.

Smith, M., J. Anderson, M. Fladeland. (2008). Chapter 14: Forest Canopy Structural Properties, in C.M. Hoover, ed., *Media Field Measurements for Carbon Monitoring,* Springer Science + Business Media B.V., p. 179-196.

Thomas, J.W., E.D. Forsman, J.B. Lint, E.C. Meslow, B.B. Noon, and J. Verner. (1990). A Conservation Strategy for the Northern Spotted Owl. Interagency Scientific Committee to Address the Conservation of the Northern Spotted Owl. U.S. Gov. Printing Office: 1990-791-171/20026.

Tucker, C. J. (1979). Red and photographic infrared linear combinations for monitoring vegetation. Remote Sensing of Environment 8(2): 127-150.

Vogt, P.; K.H. Riitters, C. Estreguil, J. Kozak, T.G. Wade, J.D. Wickham. 2006. Mapping spatial patterns with morphological image processing. Landscape Ecology 22: 171-177.

Wasser L, Day R, Chasmer L, Taylor A. (2013). Influence of Vegetation Structure on Lidar-derived Canopy Height and Fractional Cover in Forested Riparian Buffers During Leaf-Off and Leaf-On Conditions. PLoS ONE 8(1): e54776. doi:10.1371/journal.pone.0054776

Whitemore, T.C., N.D. Brown, M.D. Swaine, D. Kennedy, C.I. Goodwin-Bailey, W.K. Gong. (1993). Use of Hemispherical Photographs in Forest Ecology: Measurement of Gap Size and Radiation Totals in a Bornean Tropical Rain Forest. Journal of Tropical Ecology, 9, 131-151.

Wisdom, M.J., Holthausen, R.S., Wales, B.C., Hargis, C.D., Saab, V.A., Lee, D.C., Hann,W.J., Rich, T.D., Rowland, M.M., Murphy,W.J., Eames, M.R. (2000). Source habitats for terrestrial vertebrates of focus in the Interior Columbia Basin: broad-scale trends and management implications. USDA Forest Service, Pacific Northwest Research Station, Gen. Tech. Rep. PNWGTR- 485, 529 pp.

Yu, L., Liang, L., Wang, J., Zhao, Y., Cheng, Q., Hu, L., and Liu, S. (2014). Meta-discoveries from a synthesis of satellite-based land-cover mapping research, 35(13), 4573–4588. doi:10.1080/01431161.2014.930206.

Chapter 2: Modeling forest canopy height using moderate resolution leaf-off airborne light detection and ranging (LiDAR)

2-1. Abstract

Canopy height is an important metric in forest research and management with uses in estimating stand volume, scheduling silvicultural treatments, and assessing risk to utility infrastructure. In recent years, airborne LiDAR has been commonly used to model canopy height continuously and remotely across large areas. A number of studies have showed that LiDAR is effective in this regard when collected during leaf-on conditions but relatively few studies have investigated the potential for leaf-off airborne LiDAR to model canopy height. However, the majority of LiDAR datasets are collected primarily for terrain modeling and are thus acquired during leaf-off conditions. The few studies that have investigated the accuracy of leaf-off LiDAR in modeling canopy height have either examined broad classes of deciduous species or have used high resolution datasets that are not likely to be typical of LiDAR data collected for large scale terrain models. Therefore, in this paper, we assessed the accuracy of a canopy height model derived from a leaf-off airborne LiDAR dataset for several deciduous and coniferous species common to the forests of the northeastern United States. The LiDAR data were discrete return and moderate resolution (1.6 pts / m^2) collected for the primary purpose of modeling terrain.

We used airborne LiDAR to create a 1-meter resolution maximum canopy height model (CHM_{air}) for which grid cell values were determined based on the tallest feature in the cell. Maximum heights were measured in the field for 1,195 trees, which included 19 deciduous and coniferous species. Field measures of average canopy heights were determined, for circular plots with radii of 4 and 8 meters, using a maximum height CHM derived from a terrestrial laser

scanner (CHM_{terr}). The CHM_{air} underestimated maximum overall tree heights with a median difference of approximately 1.3 meters. Height biases were largest for white ash, red oak, and white oak. We did not find significant differences in biases corresponding to species' leaf-types (i.e. simple, compound, needle). Biases in maximum height estimates increased substantially as the CHM_{air} cell size increased above 1 meter. Estimates of mean canopy heights were significantly improved when either canopy density or average maximum return number (MRN) were used as co-predictors with average CHM_{air}. In multiple regression models predicting average canopy height, the RMSE values ranged from 1.26 – 1.78 m for plots 4 meters in radius; RMSE values ranged from 0.87 – 1.4 for plots 8 meters in radius. Degrading the resolution of CHM_{air} had no significant effect on the median differences between the average CHM_{air} and the average CHM_{terr} for cell sizes of 2, 4, and 8 meters. However, the variance of the differences increased substantially for CHM_{air} cell sizes larger than 2 meters. Although average MRN showed good potential for improving estimates of mean canopy height in our study area, future work should investigate its utility of as a co-predictor of average canopy height for a diversity of forest types.

2-2. Introduction

Measures of forest canopy height have many uses in forest research and management. Canopy height is correlated with several important forest stand characteristics including stand volume, canopy fuel load, stand age, successional state, site quality, and it is an important measure in scheduling silvicultural treatments (Smith et al. 2008, Anderson et al. 2005, Popescu and Wynne 2004). We have also found in our ongoing research that canopy height is a useful predictor of tree-related damage to utility infrastructure (Parent, Volin, Rudnicki, and Worthley, unpublished data).

Heights are typically measured for individual trees in the field by using a variety of mechanical or electronic clinometers, hypsometers, or height meters (Smith et al. 2008, Avery and Burkhart 1983). Measurements may be made for all trees or for a sample of trees within a plot or stand area. Average canopy height is typically computed either as the average of all heights within the sample or as the mean sample height weighted by basal area (see Naesset 2004).

Tree height can be difficult to measure accurately in the field even with the use of precision instruments and it is time consuming and expensive (Anderson et al. 2006). These ground-based measurements can be further complicated by random errors introduced by field personnel (Hyyppa and Inkinen 1999). For instance, during leaf-on conditions in closed-canopy forests, the top of tree crowns are often obscured by the canopy which greatly increases the chances for human error (Anderson et al. 2006). Leaning trees can also be problematic when the apex of the crown is offset from the base of the stem.

In recent years, ground-based laser scanners have provided a potential alternative for field-based measurements of canopy height (Hopkinson et al. 2004). These scanners are capable of mapping the forest canopy and understory with survey-grade precision and millimeter-level resolution. Leaf-on conditions, however, may prevent mapping of the top of the canopy and, therefore, result in negatively biased height estimates. In addition, the high cost of terrestrial scanners is likely to ensure that their use for measuring canopy heights will remain limited in the foreseeable future.

Small-footprint discrete-return airborne LiDAR has been used in recent years to model forest canopy height continuously and remotely over large areas (Lim et al. 2003). Most literature focuses on the use of leaf-on LiDAR data to model height because the foliage will help

minimize the penetration of laser pulses into the forest canopy before generating a detectable return. These studies have consistently found that leaf-on airborne LiDAR underestimates canopy height by about 1-4 meters depending on the type of forest (Wasser et al. 2013, Goodwin et al. 2006, Suarez et al. 2005; Popescue and Wynne 2004, Gaveau and Hill 2003, Nissan 1996). The biases in LiDAR-based canopy height in some studies have been reduced by incorporating species classifications or canopy density metrics in the models of canopy height (Orka et al. 2010, Naesset 2005). Studies have found that LiDAR-based estimates of height are robust to variation in beam footprint diameter and sensor platform altitude (Goodwin et al. 2006, Nissan 1996) suggesting that the results of LiDAR studies are generally applicable to small-footprint LiDAR datasets.

LiDAR data acquired for the purpose of modeling forest canopy height are ideally collected during leaf-on conditions for deciduous forests. However, the primary intent of most LiDAR acquisitions is to create digital elevation models (DEM) and, thus, the data are typically collected during leaf-off conditions in order to maximize the likelihood of laser pulses reaching the ground (Hodgson et al. 2003). Terrain elevation is also an important tool in assessing forest conditions and is needed to measure canopy height. Thus, the ability to use leaf-off LiDAR data for modeling forest canopy structure would be highly advantageous as it would allow a large data resource to be leveraged in forest monitoring efforts. Furthermore, future forest monitoring could be done more efficiently by eliminating the need for supplementary leaf-on LiDAR data.

Several studies have used leaf-off LiDAR data to model canopy height in deciduous forests and have shown these data to be effective even in forests with a significant deciduous tree component (Wasser et al. 2013; Orka et al. 2010; Naesset 2005; Brandtberg 2003). In a mixed deciduous/coniferous forest in the northeastern U.S., Wasser et al. (2013) found that height

models based on leaf-off LiDAR underestimated average canopy height by 0.1 to 3.0 meters with coniferous trees having the smallest bias and compound-leaf deciduous trees having the largest bias. Brandtberg (2003) estimated maximum tree heights and found no significant differences in errors among oak (*Quercus spp.*), red maple (*Acer rubrum*), and yellow poplar (*Liriodendron tuliperifera*) species while Orka et al. (2010) found their canopy height models had slightly larger errors for aspen (*Populus spp.*) than for either birch (*Betula spp.*) or spruce (*Picea spp.*).

The density of leaf-off canopies may be expected to vary among deciduous tree species as a result of different branching structures. LiDAR pulses are likely to penetrate deeper into canopies with lower densities before intersecting biomass that is sufficient to generate a detectable return. The findings by Wasser et al. (2013) supports this expectation because their data showed that LiDAR-based heights are underestimated significantly more for compound-leaf species than for species with simple leaves or needles. Species with compound leaves tend to have a lower spatial density of branches as a result of their larger leaves (White 1983), which would presumably account for the larger biases found for compound leaf species. Orka et al. (2010) found that inclusion of a tree species variable (spruce vs. deciduous) significantly improved their models of canopy height. Naesset (2005) addressed the problem of varying canopy densities by incorporating a canopy density metric as a co-predictor in their estimates of mean canopy height. Canopy density was measured with LiDAR, using either first- or last-returns, as the ratio of canopy returns to the total number of returns in an analysis window. Canopy returns were defined based on a height threshold; the optimal height threshold was determined using stepwise multiple regression analyses and was found to vary depending on whether first- or last-return data were used. From this work, Naesset (2005) found canopy

density to be a significant predictor of mean canopy height for models using leaf-off LiDAR data.

Previous studies that modeled canopy height, using leaf-off LiDAR, have examined either a limited number of species (Orka et al. 2010; Naesset 2005) or broad categories of trees (Wasser et al. 2013). Naesset (2005) studied Norwegian boreal forests where deciduous species comprised an average of 30-40% of the tree volume and included deciduous species only as a broad class in the analysis. Orka et al. (2010) also investigated a Norwegian forest and included only two deciduous genera, birch and aspen, in their analysis. Wasser et al. (2013) included a variety of deciduous and coniferous species in their study but only analyzed them in terms of broad classes - compound leaf, simple leaf, and needle-leaf. Brandtberg et al. (2003) included genus-level assessments for oaks, maple, and yellow poplar; however, the LiDAR data used in their study included 12 returns / m^2 which is a considerably higher sampling density than typical for datasets obtained for mapping terrain elevation. The variety in canopy structure among deciduous species warrants broader species- or genus-specific investigations into the utility of leaf-off LiDAR in estimating forest canopy height. Furthermore, the utility of low to moderate resolution leaf-off LiDAR data, in this application, should be of great interest given the rapidly increasing availability of these data as a result of terrain mapping efforts. Thus, the primary objective of this study was to examine the effectiveness of a moderate resolution (1.5 returns / m^2) leaf-off LiDAR dataset in predicting maximum and mean forest canopy heights in a temperate deciduous forest. Using forest stands comprised of up to 17 deciduous and two evergreen species, we focused on species-level assessments to determine the importance of inter-species variation on the accuracy of canopy height models. We assessed the robustness of height models to simulated degradations of LiDAR spatial resolutions. Furthermore, a secondary

objective of this study was to test the effectiveness of canopy density as a co-predictor of canopy height. The LiDAR data used in this study were collected for the primary purpose of modeling terrain and thus we aim to determine if datasets collected for terrain modeling have utility in modeling average and maximum canopy heights.

2-3. Methods

All data processing and analyses was performed using scripts written in Python v2.7 with ArcGIS 10.1. All statistical analyses were conducted in Python using SciPy v0.13 and Matplotlib v1.3.1.

2-3.1. Study Area

The study area for this research was located in eastern Connecticut in the northeastern United States and covers an area of approximately 4800 km^2 (Figure 2-1). Forestlands in this region are dominated by deciduous forests with oak/hickory (*Quercus spp*. and *Carya spp*.) and other hardwood forest species such as elm/ash/maple (*Ulmus spp.*, *Fraxinus spp.*, and *Acer spp.*) in addition to some coniferous species including white pine (*Pinus strobus*) and eastern hemlock (*Tsuga canadensis*) (Wharton et al. 2004, Dreiss and Volin 2013). Topography can be characterized as hilly with elevations ranging from sea level in the south to 330 meters in the north.

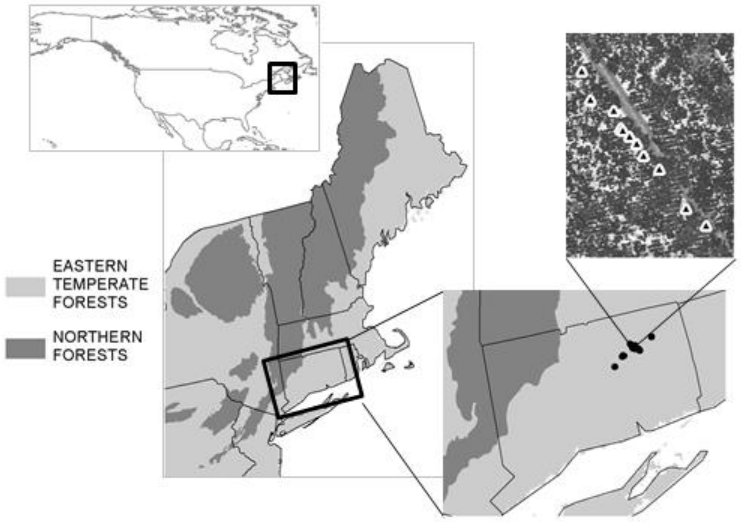

Figure 2-1: The forests of the northeastern USA are dominated by temperate deciduous and northern deciduous/coniferous forests (bottom left). The field sites are located in the temperate forests of northeastern Connecticut, USA (72.3^0 W, 41.7^0 N) (bottom right). White triangles indicate locations of trees at one of the field sites (top right).

2-3.2. Field data collection – tree locations and canopy height

Field data were collected during three sets of surveys conducted in May-July of 2010, November 2012, and May-June of 2013. Each survey used geodetic traverses to obtain survey-quality coordinates for the locations at which canopy heights were measured. Traverses were oriented using two reference points for which coordinates were established by taking static observations, for a minimum of 45 minutes, with a survey-grade GPS receiver[3]. Static GPS observations were post-processed using the Online Positioning User Service (OPUS)[4]. A total station was then used to traverse the study sites and obtain coordinates for the sample measurements.

[3] The GPS receivers used for the 2010, 2012, and 2013 surveys were a Topcon HiPer Lite+, a Leica viva gs-15, and a Sokkia GRX-1 respectively.
[4] See http://www.ngs.noaa.gov/OPUS/

The 2010 survey was conducted on the University of Connecticut's Storrs campus where sample trees were located in open or semi-open areas. A total station was used to measure the coordinates of tree stem location as well as the maximum tree height. The species that were sampled included red maple (*Acer rubrum*), sugar maple (*Acer saccharum*), white ash (*Fraxinus americana*), honey locust (*Gleditsia triacanthos*), white pine (*Pinus strobus*), pin oak (*Quercus palustris*), white oak (*Quercus alba*), and red oak (*Quercus rubra*).

The 2012 survey was conducted on an approximately 0.5 ha forest patch on the University of Connecticut's Plant Science Farm. The forest patch was surveyed using a Leica ScanStation C10 terrestrial laser scanner. The Leica ScanStation C10 measurements have a positional accuracy of 6mm and a scan resolution of 7mm (Leica 2014). Scans were conducted from control markers that traversed the site. The control markers had been surveyed previously using a total station and GPS in a geodetic traverse. The locations of all trees in the study area with a diameter-at-breast-height (DBH) larger than 4 cm were surveyed using a total station. The canopy trees on the site were comprised mainly of red maple, shagbark hickory (*Carya ovata*), and white ash.

The 2013 survey included 11 sites in northeastern Connecticut located on public forest lands. Canopy trees along road or field edges were included in the survey and only trees with clearly visible crowns that were not overtopped by neighboring trees were used for this study. The canopy at the sites ranged from semi-closed to closed canopy. The height of the tallest portion of the tree crown was measured using a tripod-mounted Lasertech - Impulse LR200 hypsometer. The maximum tree height often did not correspond to a location directly above the base of the stem because forest edge trees tend to lean toward the canopy opening. Therefore, a prism reflector was positioned at the approximate location beneath the tallest part of the crown

and was used as the target for both the total station and the hypsometer. The species recorded in the survey included red maple, sugar maple, black birch (*Betula lenta*), yellow birch (*Betula alleghaniensis*), shagbark hickory, pignut hickory (*Carya glabra*), mockernut hickory (*Caraya tomentosa*), white ash, white pine, big-toothed aspen (*Populus grandidentata*), quaking aspen (*Populus tremuloides*), black cherry (*Prunus serotina*), white oak, red oak, and black oak (*Quercus velutina*), eastern hemlock (*Tsuga canadensis*), and American elm (*Ulnus americana*).

2-3.3. *Airborne LiDAR dataset*

The airborne LiDAR data were acquired for nearly 4600 km^2 in eastern Connecticut during leaf-off conditions from November 3 – December 11, 2010 (Dewberry 2011). The data were collected with a Leica ALS60 Airborne Laser Scanner at an altitude of approximately 2000 meters above ground level. At this altitude, the ALS60's beam divergence of 0.22 millirads creates a footprint of roughly 44 cm on the ground. The scanner's pulse rate was 117.9 kHz and the flight line overlap was 50%. The data provider eliminated data with gaps between the geometrically usable portions of the swaths. The maximum scan angle of the sensor was 16.5^0 from nadir and it recorded up to 4 returns per laser pulse. The dataset has an overall density of 1.56 returns / m^2 with a maximum point spacing of 0.7 meters, excluding water bodies. The horizontal accuracy of the dataset is equal to or better than 1 meter RMSE. The project's principle contractor processed the LiDAR data to create a bare-earth DEM, at a 1-meter resolution, with building features removed. Dewberry (2011) evaluated the accuracy of the DEM using 62 surveyed ground control points distributed through non-vegetated, grass, and forested terrains. The vertical RMSE for the DEM, based on ground control points, was estimated at 5 cm in non-vegetated terrain, 17 cm for grassy terrain, and 21 cm in forest terrain. The primary purpose of the LiDAR dataset was to develop the bare-earth DEM for use in conservation

planning, floodplain mapping, dam safety assessments, and hydrological modeling (Dewberry 2011).

2-3.4. Airborne and terrestrial LiDAR-based canopy height models

A canopy height model, based on airborne LiDAR (CHM_{air}), was created following the methods described in Parent and Volin (2014). The CHM_{air} was created by subtracting the bare-earth DEM, created by Dewberry (2011), from a digital surface model (DSM) that we created from the airborne LiDAR data. The DSM corresponded to the maximum elevations in the tree canopy and was aligned to the DEM grid and had the same 1-meter resolution. The cell values for the DSM were determined by taking the maximum of all non-ground first-return points within a given cell. Because the overall density of the LiDAR dataset was 1.56 returns / m^2, the majority of non-water pixels in the DSM grid contained at least one first-return point. The first-returns were filtered to remove points that obviously did not correspond to features on the earth's surface (e.g. large birds in flight). These anomalous points were identified by comparing each first-return to all points within a 2.5 meter radius. Points were discarded if they were more than 30 meters taller than any other points within the neighborhood. We selected the 30-meter threshold because it approximates the upper limit of canopy heights in northeastern forests and thus it represented a reasonable maximum elevation difference for points along forest gaps and edges. Considering the point spacing of our airborne LiDAR data, we assumed that continuous data gaps larger than 3 meters in radius were likely to correspond to water, which tends to absorb LiDAR energy (Campbell and Wynne 2011). The bare-earth DEM values were assigned to the cells in these larger data gaps that were presumed to correspond to water bodies. A test of 52 1x1 km sample areas showed that only 12.9%, on average (std. dev. = 3.4), of the areas consisted of data gaps for which there was no first-return data. More than 91% of these gaps were less than 1

meter in radius; approximately 7% of the gaps were 1-2 meters in radius; and approximately 1% of the gaps were 2-3 meters in radius. Thus, we interpolated the values for cells in the DSM data gaps, smaller than 3 meters in radius, by taking the median of the known values in the cells' eight nearest neighbors. Cells with fewer than three known nearest neighbors were filled using a 2^{nd} or 3^{rd} interpolation pass.

We used the terrestrial laser scanner data to create a DSM that corresponded to the maximum tree canopy surface. The DSM grid had a spatial resolution of 15 cm and the elevation of the highest data point within a grid cell was assigned as the cell value. We considered grid cell values to be anomalous if the elevation was more than two meters higher than any of its surrounding neighbors. Cells with anomalous values were identified using a roving 3x3 window and values were replaced with the median of the known values in the eight nearest neighbors. We did not attempt to fill the null data gaps in the DSM because our validation analysis did not require a continuous surface. A 15-cm resolution canopy height model based on the terrestrial laser scanner (CHM_{terr}) was created by subtracting Dewberry's (2011) airborne LiDAR DEM from the terrestrial scanner DSM.

2-3.5. Airborne canopy height model validation – maximum and average height

The CHM_{air} was used to obtain the airborne LiDAR height estimates for each tree sampled in the 2010, 2012, and 2013 field surveys. Buffers with a 2-meter radius were created around the tree stem locations (2010, 2012) or the locations of the field height measurement (2013). The buffer accounted for the 1-meter horizontal position accuracy of the airborne LiDAR dataset as well as potential offsets between the surveyed coordinates and the crown apex. The height for a given sample location was taken to be the maximum value of the CHM_{air} grid cells that were contained in the buffer.

The CHM_{terr} served as the field validation data for the trees in the 2012 survey. Tree stem locations were buffered by 2-meters and tree heights were taken to be the maximum value of the CHM_{terr} within the buffer. The 2-meter buffer in this case was used to help account for offsets between the surveyed coordinates, corresponding to the tree stem, and the crown apex.

The 2012 CHM_{terr} was used to validate the airborne LiDAR estimates of mean canopy height. We performed the validation using circular plots with radii of 4- and 8-meters. The plots were uniformly distributed throughout the study area, in a grid pattern, and there was no overlap between plots. Average plot values were calculated for both the CHM_{terr} and the CHM_{air}. Null data values in the CHM_{terr} were ignored when computing the average and plots were discarded if more than 10% of the area consisted of CHM_{terr} grid cells with null data values.

2-3.6. Estimating canopy density

Previous research suggested that canopy density can be used to correct height estimates based on airborne LiDAR (Naesset 2005). Thus, we estimated canopy density using the canopy-to-total-return-ratio (CTRR) which has been used in various forms in the literature (Morsdorf et al. 2006, Hopkinson and Chasmer 2009, Korhonen et al. 2011, Wasser et al. 2013, Parent and Volin 2014). We calculated the CTRR as the ratio of canopy first-returns to the total number of first returns in the 4- and 8-meter sample plots. Returns were considered to be in the canopy if they had heights greater than three meters.

We tested a second approach of estimating canopy density based on our suspicion that the total number of returns generated from a given laser pulse would provide an indication of canopy density. Pulses should penetrate further into less dense canopies and thereby have greater opportunity to generate multiple returns. Thus, we developed a 1-meter raster grid in which the

cell values were the maximum return number (MRN) of the airborne LiDAR pulses contained within the cell. We created two versions of the MRN raster which included pulses with scan angles of $0\text{-}5^0$ and $0\text{-}10^0$ from nadir, respectively. The $MRN_{0\text{-}5^o}$ and $MRN_{0\text{-}10^o}$ grids were averaged for the 4- and 8-meter sample plots.

2-3.7. The effect of CHM spatial resolution on maximum and average height estimates

The point spacing of a LiDAR dataset determines the spatial resolution of the canopy height model that can be derived from it. We simulated the effect of lower density LiDAR datasets by increasing the cell size of the CHM_{air} grid to 2-, 4-, and 8-meters. To degrade the resolution of the original CHM_{air}, we created grids with the desired cell sizes and aligned to the original CHM. We randomly selected a value from a single 1-meter pixel that coincided with the larger pixel and this value was assigned to the larger pixel. The resulting CHM_{air} grids were used to validate maximum and average canopy heights.

2-4. Results

2-4.1. Maximum canopy height validation

The 2010 field survey included a total of 360 sample trees representing eight deciduous species that ranged in height from 4 to 28 meters. The field data were strongly correlated with the CHM_{air} heights with a regression model $r^2 = 0.90$ and RMSE = 1.59 (Figure 2-2). The regression model slope and y-intercept was 0.92 and 1.02 respectively. There was no significant bias in the CHM_{air} height estimates when compared to the field heights ($p=0.42$). The median difference between the CHM_{air} and field height was -0.06m with a standard deviation of 1.64m (Figure 2-3). We found no significant biases for species with more than 15 sample points which included red maple, sugar maple, white ash, honey locust, pin oak, and red oak (Figure 2-4).

However, there was a significant difference between pin oak and red maple (p=0.03) with pin oak having a median of 0.36m and red maple having a median of -0.33m. No significant differences were found among other pairs of species. There was no bias in CHM_{air} heights for simple, compound, or coniferous leaf types and no significant differences were found among leaf types (Figure 2-5).

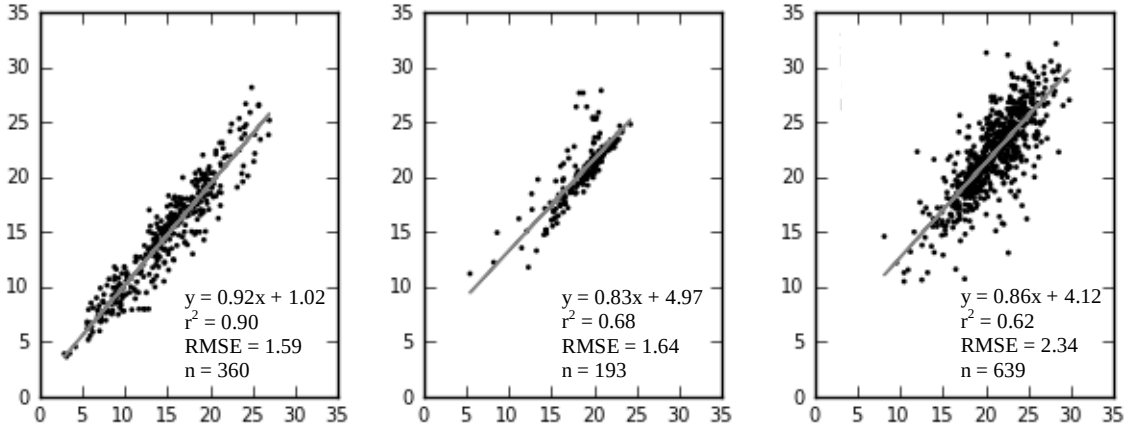

Figure 2-2: Maximum height linear regression model results the 2010 (left), 2012 (middle), and 2013 (right) field surveys. The x-axis shows airborne LiDAR height and the y-axis shows the validation height.

The 2012 terrestrial LiDAR survey included 193 trees representing three deciduous species with heights ranging from 11 to 28 meters. The linear regression model between tree height estimates from CHM_{terr} and CHM_{air} had an r^2=0.68 and RMSE=1.64m with a slope=0.83 and y-intercept=4.97 (Figure 2-2). CHM_{air} significantly underestimated tree heights ($p<0.001$) for the overall dataset with a median difference of -1.28 m with a standard deviation of 1.72m (Figure 2-3). The distribution of differences had a significant negative skew ($p<0.001$), towards underestimation by CHM_{air}, due to some large negative outliers. The underestimates by CHM_{air} were significant for each of the species sampled with difference distributions skewed for each species (Figure 2-6). There were no significant difference among species which included red maple, shagbark hickory, and white ash (Figure 2-6).

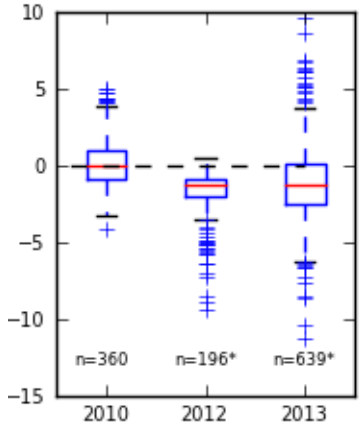

Figure 2-3: Differences among 2010, 2012, and 2013 surveys for the CHM_{air} maximum height minus the validation height. Asterisks indicate medians that are significantly different from zero ($p<0.05$).

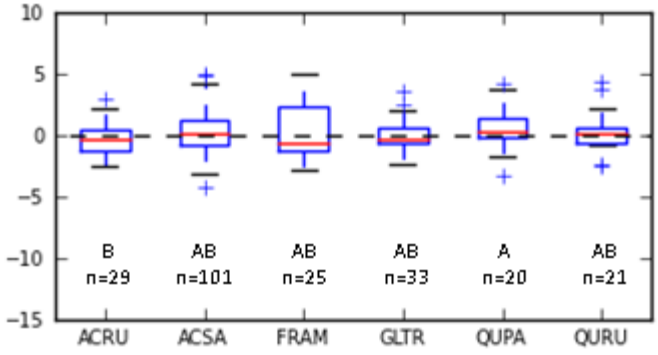

Figure 2-4: Differences among species for the 2010 vegetation survey for the CHM_{air} maximum height minus the validation height. Only species with at least 15 samples are included: red maple (ACRU), sugar maple (ASCA), white ash (FRAM), honey locust (GLTR), pin oak (QUPA), and red oak (QURU). Letters denote statistically separable groups. The median was not significantly different from zero for any species ($p<0.05$).

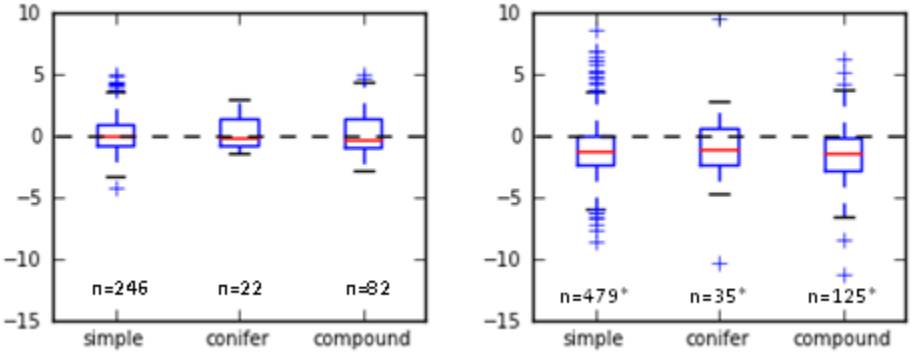

Figure 2-5: Differences among leaf type for CHM_{air} maximum height minus the validation height for the 2010 (left) and 2013 (right) vegetation surveys. Asterisks indicate medians that are significantly different from zero ($p<0.05$). The medians were not significantly different among leaf types for either survey.

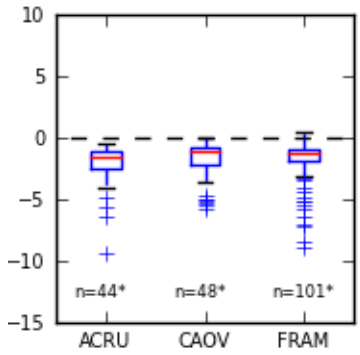

Figure 2-6: Differences among species for the 2012 vegetation survey for the CHM_{air} maximum height minus the validation height by species. Species include red maple (ACRU), shagbark hickory (CAOV), and white ash (FRAM). Asterisks indicate medians that are significantly different from zero ($p<0.05$). The medians were not significantly different among species.

The 2013 field survey included 639 sample trees representing 17 deciduous species with heights ranging from 11 to 32 meters. The linear regression model had an $r^2=0.62$ and RMSE=2.34m with a slope of 0.86 and y-intercept of 4.12 (Figure 2-2). Overall, the CHM_{air} significantly underestimated the field heights ($p < 0.001$) with a median difference of -1.26m and standard deviation of 2.38m (Figure 2-3). The underestimate was significant for all species except for black cherry ($p=0.80$) and black oak ($p=0.15$) (Figure 2-7). White ash, white oak, and red oak had the largest underestimates with median differences of -2.1, -1.68, and -1.78 meters, respectively. Black cherry had the smallest underestimate with a median difference of -0.07 meters (Figure 2-7). CHM_{air} significantly underestimated heights for all leaf types including simple, compound, and needle leaf species (Figure 2-5). However, no significant differences were found among leaf types.

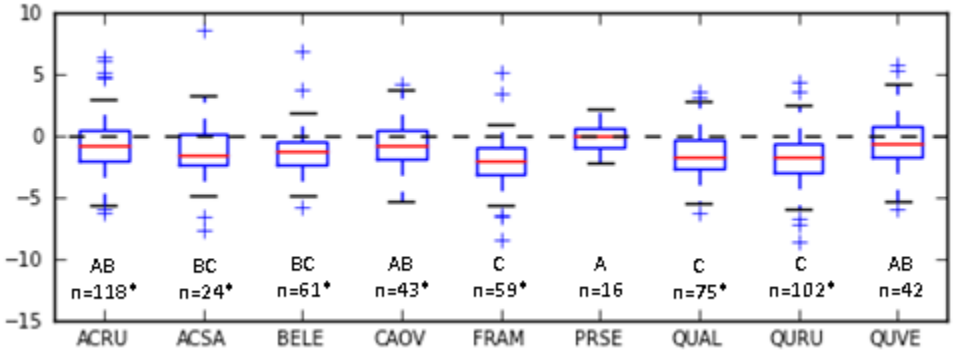

Figure 2-7: Differences among species for the 2013 vegetation survey for the CHM_{air} maximum height minus the validation height. Only species with at least 15 sample points are included: red maple (ACRU), sugar maple (ASCA), black birch (BELE), shagbark hickory (CAOV), white ash (FRAM), black cherry (PRSE), white oak (QUAL), red oak (QURU), and black oak (QUVE). Letters denote statistically separable groups. Asterisks indicate medians that are significantly different from zero ($p<0.05$).

The ability of the CHM_{air}, to predict maximum canopy height, declined steadily and sharply as the cell size of the CHM_{air} was increased to 2-, 4-, and 8-meters (Figure 2-8). Across all survey data, as the CHM_{air} grid cell size increased, the airborne LiDAR predictions became progressively more biased towards underestimation of the validation heights (Figure 2-8, Table 2-1). Variation in the predictions increased, especially for the 2012 field survey for which tree heights were estimated from CHM_{terr} (Figure 2-8, Table 2-1).

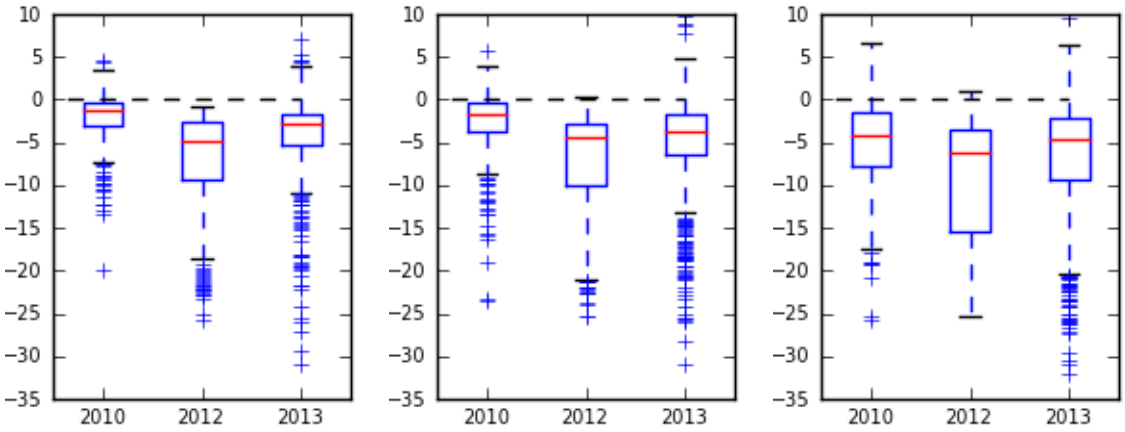

Figure 2-8: The CHM_{air} maximum height minus the validation height by CHM cell size for the 2010, 2012, and 2013 vegetation surveys. CHM_{air} cell sizes are 2- (left), 4- (middle), and 8- (right) meters.

Table 2-1: The CHM_{air} maximum height minus the validation height for CHM_{air} cell sizes of 1-, 2-, 4-, and 8-meters.

Survey	1m		2m		4m		8m	
	median	stdev	median	Stdev	median	stdev	median	stdev
2010	-0.06	1.64	-1.34	3.05	-1.77	3.86	-4.15	5.04
2012	-1.28	1.72	-4.85	4.66	-4.5	6.78	-6.17	7.73
2013	-1.26	2.38	-2.93	4.66	-3.71	5.73	-4.55	7.07

2-4.2. Average canopy height validation

The average CHM_{air} height was a strong predictor of average CHM_{terr} height for both the 4- and 8-meter plots; however, correlations improved as plot size increased. For models using average CHM_{air} height as the only predictor, the r^2 values were 0.64 and 0.72 for the 4- and 8-meter radius plots, respectively (Table 2-2). The CTRR and average $MRN_{0\text{-}5^o}$ were found to be highly significant co-predictors of CHM_{terr} for each plot size. Models that used CHM_{air} and average $MRN_{0\text{-}5^o}$ as predictors had r^2 values of 0.82 and 0.89 for the 4 and 8-meter radius plots, respectively (Table 2-2). Models using CTRR as the co-predictor had slightly lower performance with r^2 values of 0.77 and 0.81, respectively. Average $MRN_{0\text{-}10^o}$ was a highly significant predictor for the 4-meter radius plots but it was not significant for the 8-meter plots ($p=0.135$). Models that included the average $MRN_{0\text{-}10^o}$ for the 4- and 8-meter plots had r^2 values of 0.69 and 0.74, respectively. The coefficients for average $MRN_{0\text{-}5^o}$, average $MRN_{0\text{-}10^o}$, and CTRR were negative in all models (Table 2-2).

The differences between average CHM_{air} and CHM_{terr} heights increased with CHM_{air} grid cell sizes larger than 2 meters (Figure 2-9). The medians and standard deviations were very similar for the 1- and 2-meter CHM_{air}'s regardless of plot size. There was no significant change in the median difference as the spatial resolution of the CHM_{air} was decreased to 8-meters

although coarser resolutions tended to have more extreme differences between CHM_{air} and CHM_{terr} (Figure 2-9).

Table 2-2: Models of average canopy height models for validation plots with radii of 4- and 8-meters. Predictors include average CHM_{air} height, average maximum return number ($MRN_{0\text{-}5^0}$ and $MRN_{0\text{-}10^0}$), and canopy-to-total-return-ratio (CTRR).

Independent variables	Coefficients and levels of significance							
	4 meter models				8 meter models			
	1	2	3	4	1	2	3	4
avg. CHM_{air} height	0.86	1.09	0.94	1.12	0.92	1.20	0.98	1.32
Signif.	*<0.001*	*<0.001*	*<0.001*	*<0.001*		*<0.001*	*<0.001*	*<0.001*
avg. $MRN_{0\text{-}5^0}$	--	-5.48	--	--	--	-7.10	--	--
Signif.		*<0.001*				*<0.001*		
avg. $MRN_{0\text{-}10^0}$	--	--	-4.81	--	--	--	-4.07	--
Signif.			*0.001*				*0.135*	
CTRR	--	--	--	-8.22	--	--	--	-9.48
Signif.				*<0.001*				*0.005*
Constant	2.99	9.13	6.30	5.18	2.06	10.38	5.00	3.48
Signif.	*0.002*	*<0.001*	*<0.001*	*<0.001*	*0.153*	*<0.001*	*<0.001*	*0.011*
Number of Obs.	68	68	68	68	22	22	22	22
Adjusted r^2	0.64	0.82	0.69	0.77	0.72	0.89	0.74	0.81
RMSE	1.78	1.26	1.63	1.41	1.4	0.87	1.32	1.12

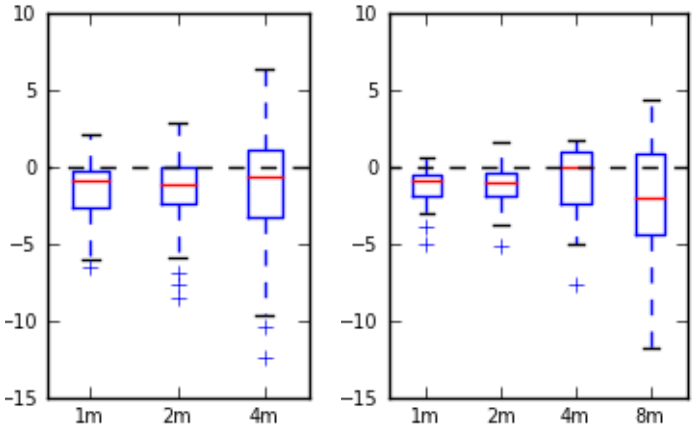

Figure 2-9: Differences among cell sizes in the CHM_{air} mean height minus the validation height for plots with 4 (left) and 8 (right) meter radii. Data are from the 2012 vegetation survey for which terrestrial LiDAR data provided continuous height measurements and enabled mean height to be measured. The x-axis shows the CHM cell size. The medians did not differ significantly with cell size for either plot size.

2-5. Discussion

This study has expanded on the broad leaf-type and genus-level investigations of previous work to include species-level assessments for the variety of deciduous species found in eastern Connecticut. Furthermore, our study used LiDAR data that are typical of those collected for terrain modeling applications whereas much of the previous research has been done using data of higher spatial resolution. Our research confirmed that leaf-off LiDAR-based canopy height models can successfully estimate maximum and mean canopy heights for deciduous trees with only relatively slight negative biases. The CHM_{air} maximum canopy height estimates demonstrated a negative bias for the 2012 and 2013 data, which is consistent with previous research particularly in studies that used leaf-off data (Wasser et al. 2013; Orka et al. 2010; Naesset 2005; Brandtberg 2003). Airborne LiDAR can be expected to underestimate canopy height because a laser pulse must penetrate some distance into a tree canopy before contacting biomass with sufficient surface area to generate a detectable return signal. The magnitude of the height underestimation by CHM_{air} was similar for the 2012 and 2013 surveys because the 2012 survey occurred after the end of the growing season and the 2013 survey occurred at the beginning of the following growing season. Furthermore, the sites of these field surveys were located predominately in mature forest stands and, thus, there is likely to have been little growth in canopy height between the time of the airborne LiDAR acquisition and the field surveys. The CHM_{air} did not show the expected negative height bias for the 2010 field survey; however, which was likely due to the field survey being conducted during the growing season prior to the LiDAR acquisition. Many of the trees in the 2010 survey were not mature and, thus, height growth may have been significant between the time of the field survey and the LiDAR acquisition, which would mask a bias in CHM_{air} heights.

Wasser et al. (2013) found that leaf-off airborne LiDAR underestimated average canopy heights more in stands dominated by compound-leaf species than in stands dominated by simple-leaf species. Compound leaf species tend to have a lower density of branches as a result of having larger leaves (White 1983), which may allow laser pulses to pass through the leaf-off canopy more easily. In contrast to Wasser et al. (2013), we found no significant differences in CHM_{air} biases among simple, compound, and coniferous leaf types in estimates of maximum canopy heights. We suspect that the species composition in the field plots of Wasser et al. (2013) may account for the discrepancies between our results; their simple-leaf plots were dominated by red maple, black cherry, and red oak whereas their compound-leaf plots were dominated by black walnut (*Juglans nigra*), green ash (*Fraxinus pennsylvanica*), and honey locust. Our study found that red maple and black cherry are among the species for which the CHM_{air} provides the least biased estimates. Furthermore, shagbark hickory was not a dominant species in Wasser et al. (2013)'s compound-leaf plots and we found the CHM_{air} to have one of the lowest biases for this species. Thus Wasser et al. (2013)'s simple-leaf plots tended to be dominated by species with low CHM_{air} bias and the compound-leaf plots excluded at least one species that had low CHM_{air} bias. Our results, therefore, suggest that broad leaf-type classifications may not be sufficient for predicting the degree of bias expected in estimates of maximum canopy heights from leaf-off airborne LiDAR.

The CHM_{air} substantially underestimated maximum canopy heights for a number of validation points in the 2012 survey. These outliers are likely due to validation points that corresponded to crown edges instead of the tree tops as in the case of leaning trees in which the main body of the crown is not located over the base of the stem. The airborne LiDAR lacked the spatial resolution needed to detect the lower density of branches found at the edge of the crown

whereas they would be easily detected with the millimeter-level resolution of the terrestrial laser scanner. The inability of airborne LiDAR to detect the canopy edges was likely exacerbated by the substantial white ash component of the forest stand which, as our data suggest, is more easily penetrated by LiDAR than other species that we have sampled.

CHM_{air} maximum height estimates tended to become more negatively biased as the spatial resolution was decreased and the height difference distributions became strongly skewed by numerous large negative outliers. The outliers are likely due in part to the location of the validation points being along forest edges. The method we used to degrade the CHM_{air} resolution selected a random value within the larger grid cell in order to simulate a LiDAR dataset with a coarser resolution. Thus, the chance of selecting a value that corresponds to the ground rather than the tree canopy increases with the CHM_{air} cell size. Our data showed that estimates of average canopy height had little bias with CHM_{air} grid cell sizes as large as 4-meters. There was almost no discernible difference in average height estimates from CHM_{air}'s with 1- and 2-meter cell sizes. These results suggest that LiDAR datasets with return densities as coarse as 0.25 pts / m^2 can be effective in modeling average canopy height. For maximum canopy height estimates, a LiDAR point density equal to or greater than 1 pt / m^2 is needed to minimize the occurrence of large negatively biased outliers.

Naesset (2005) found that canopy density, along with LiDAR height, was a significant co-predictor of average canopy height in leaf-off conditions. The bias of the leaf-off airborne LiDAR should be inversely proportional to the density of the canopy because a laser pulse will have less penetration in dense canopies before generating an initial return to the sensor. Our results confirm that canopy density is a significant predictor in models of average canopy height. The CTRR method of estimating canopy density is similar to the method used by Naesset (2005)

for study plots that tended to be dominated by coniferous species. In our models, the coefficient for CTRR was negative which reflects the tendency of airborne LiDAR to underestimate heights for canopy areas with low density. The large positive constants, in models using CTRR, ensures that average heights are initially overestimated and must be adjusted downward based on the canopy density. A larger negative adjustment must be made for denser canopies, with high CTRR values, in order to reduce the positive adjustment made by the model constant. In lower density canopies, a larger proportion of the model constant is needed to offset the negative bias in the average CHM_{air} predictor and thus low CTRR values reduce the final model estimate by a smaller amount.

We proposed the maximum return number (MRN) as an indicator of canopy density and thus expected it to be a successful co-predictor of canopy height. Leaf-off canopies with high branch densities are likely to prevent much laser energy from penetrating the canopy beyond the initial first return. Thus, we predicted MRN would be low for high density canopies and high in low density canopies for which laser energy is able to penetrate deeper into the canopy. While MRN turned out to be a successful co-predictor of average canopy height, the positive model constant and the negative MRN coefficient was unexpected. With a positive constant and negative MRN coefficient, the MRN predictor would seem to reduce the effect of the constant more for dense canopies than for less dense canopies. However, based our initial expectations, the effect of the constant should be reduced the most for dense canopies where CHM_{air} should have the smallest bias. Further investigation led us to suspect that MRN actually distinguishes plots with canopy edge areas from plots that do not include canopy edges. The model results are consistent with an inability of the airborne LiDAR, in this study, to detect low density leaf-off branches along the canopy edge which results in the laser pulses passing through the canopy

edges without generating a canopy-level return. It seems these pulses generate the first, and typically only, return from the dense understory vegetation. Laser pulses that intercepted closed canopy areas tended to penetrate the leaf-off canopy and generate multiple returns. Thus, plots with low average MRN tended to contain canopy edges or gaps whereas plots with high average MRN values tended to correspond to closed canopy forest. CHM_{air} substantially underestimated average heights in areas where LiDAR was unable to detect the canopy edge. The regression model positively adjusted the average height for plots which contain a larger proportion of canopy edge or gap areas as indicated by low average MRN. Examination of LiDAR intensity imagery within the sample plots provided qualitative support for our suspicions. However, further work is needed to more rigorously establish the means by which MRN improved average canopy height estimates, in this study, and whether MRN is a significant co-predictor of average canopy height for other study sites.

The success of MRN as a predictor of average canopy height for the 2012 data is likely due to the study area containing only deciduous trees. Coniferous trees tend to generate relatively low MRN values but have little bias in height estimates from airborne LiDAR (Wasser et al. 2013, Naesset 2005). MRN alone would not be able to distinguish coniferous canopies, for which airborne LiDAR has relatively low bias, from leaf-off deciduous canopy edges for which airborne LiDAR is significantly biased. Thus, in areas with a significant coniferous tree component, a model would need to combine MRN with information on coniferous tree locations. Studies have found that coniferous canopies can be mapped effectively using aerial imagery or airborne LiDAR (Yao et al. 2012, Orka et al. 2009, Brandtberg 2007). A further complication of using MRN in models of average canopy height is that performance is greatly reduced when LiDAR scan angles are 10 or more degrees off nadir. Restricting the data to scan angles of less

than 10 degrees eliminates data between the flight lines. With the maximum scan angle restricted to 5 degrees off nadir, approximately one-third of the area within the extent of our dataset has no data. With a 10 degree maximum scan angle, only about 5% of the area has no data.

2-6. Conclusions

In this study we have evaluated the effectiveness of leaf-off discrete-return airborne LiDAR in modeling canopy height in deciduous forests. We have expanded upon previous literature by assessing height model biases at the species-level and for a larger variety of deciduous tree species than have been studied previously. Furthermore, the spatial resolution of the data we used is more typical of LiDAR data used in terrain modeling than that data that have been used in many of the previous studies. Our research confirms that leaf-off LiDAR tended to underestimate canopy height with median differences as large as 2-meters and 1-meter for maximum and average heights, respectively. We found that maximum height biases varied significantly within broad leaf-type categories (i.e. simple, compound, needle) as well as within genera. Predictions of average canopy height were improved by incorporating a measure of canopy density (i.e. CTRR) or average maximum return number (MRN) as co-predictors in the model. Estimates of maximum canopy height tended to become severely biased as the CHM_{air} cell size was increased above 1-meter. Average canopy height estimates were more robust to degradation of the CHM_{air} spatial resolution for cell sizes as large as 4-meters. Further work is needed to assess the significance of CTRR and MRN as co-predictors of average canopy height across a broader deciduous forest area.

2-7. Acknowledgements

The authors would like to thank Qian Lei, Elliot Olivas, Michael Heyn, Kyle Arvisais, Mathew Solmo, Gabe Sipson, Bojan Bojic, Malcom Smith, Lindsay Chateauvert, and Michael Kelly for their work in field surveys during which the data for this study were collected. We also thank Thomas Meyer for providing us with the terrestrial LiDAR dataset. Field work was supported, in part, by Northeast Utilities. We thank the Natural Resources Conservation Service for making the airborne LiDAR data available to us. Finally, we thank John Silander and Chadwick Rittenhouse for their helpful reviews of this manuscript.

2-8. References

Andersen, H.-E., McGaughey, R. J., & Reutebuch, S. E. (2005). Estimating forest canopy fuel parameters using LIDAR data. Remote Sensing of Environment, 94(4), 441–449. doi:10.1016/j.rse.2004.10.013

Andersen, H.-E., Reutebuch, S. E., & McGaughey, R. J. (2006). A rigorous assessment of tree height measurements obtained using airborne lidar and conventional field methods. Canadian Journal of Remote Sensing, 32(5), 355–366. doi:10.5589/m06-030

Avery T.E., Burkhart H.E. (1983). Forest Measurements (3rd edition). McGraw-Hill, New York.

Brandtberg, T. (2007). Classifying individual tree species under leaf-off and leaf-on conditions using airborne lidar. ISPRS Journal of Photogrammetry and Remote Sensing, 61(5), 325–340. doi:10.1016/j.isprsjprs.2006.10.006

Brandtberg, T. (2003). Detection and analysis of individual leaf-off tree crowns in small footprint, high sampling density lidar data from the eastern deciduous forest in North America. Remote Sensing of Environment, 85(3), 290–303. doi:10.1016/S0034-4257(03)00008-7

Campbell, J.B. and R.H. Wynne. (2011). Introduction to Remote Sensing (Fifth Edition). The Guilford Press. New York, NY. 483-484.

Dewberry. (2011). Project Report for the U.S. Corp of Engineers High Resolution LiDAR Acquisition & Processing for Portions of Connecticut. USACE Contract W912P9-10-D-0534. Prepared by Dewberry. 71 pp.

Gaveau, D. L. and Hill, R. (2003). Quantifying canopy height underestimation by laser pulse penetration in small-footprint airborne laser scanning data. Canadian Journal of Remote Sensing, 29(5), 650–657. doi:10.5589/m03-023

Goodwin, N. R., Coops, N. C., & Culvenor, D. S. (2006). Assessment of forest structure with airborne LiDAR and the effects of platform altitude. Remote Sensing of Environment, 103(2), 140–152. doi:10.1016/j.rse.2006.03.003

Hodgson, M. E., Jensen, J. R., Schmidt, L., Schill, S., & Davis, B. (2003). An evaluation of LIDAR- and IFSAR-derived digital elevation models in leaf-on conditions with USGS Level 1 and Level 2 DEMs. Remote Sensing of Environment, 84(2), 295–308. doi:10.1016/S0034-4257(02)00114-1

Hopkinson, C. and L.E. Chasmer. (2009). Testing LiDAR models of fractional cover across multiple forest ecozones. Remote Sensing of Environment, 113: 275-288.

Hopkinson, C., Chasmer, L., Young-Pow, C., and Treitz, P. (2004). Assessing forest metrics with a ground-based scanning lidar. Canadian Journal of Forest Research, 34(3), 573–583. doi:10.1139/x03-225

Hyyppa, J., & Inkinen, M. (1999). Detecting and estimating attributes for single trees using laser scanner. Photogrammetric Journal of Finland, 16(2), 27–42.

Korhonen, L., Korpela, I., Heiskanen, J., & Maltamo, M. (2011). Airborne discrete-return LIDAR data in the estimation of vertical canopy cover, angular canopy closure and leaf area index. Remote Sensing of Environment, 115(4), 1065–1080. doi:10.1016/j.rse.2010.12.011

Leica. 2014. Leica ScanStation C10: The All-in-One Laser Scanner for Any Application. Leica Geosystems. Heerbrugg, Switzerland. Accessed online (March 2014) at http://hds.leica-geosystems.com/en/Leica-ScanStation-C10_79411.htm.

Lim, K., Treitz, P., Wulder, M., St-Onge, B., & Flood, M. (2003). LiDAR remote sensing of forest structure. Progress in Physical Geography, 27(1), 88–106. doi:10.1191/0309133303pp360ra

Næsset, E. (2005). Assessing sensor effects and effects of leaf-off and leaf-on canopy conditions on biophysical stand properties derived from small-footprint airborne laser data. Remote Sensing of Environment, 98, 356–370. doi:10.1016/j.rse.2005.07.012

Nilsson, M. 1996: Estimation of tree heights and stand volume using an airborne LiDAR system. Remote Sensing of Environment 56, 1–7.

Morsdorf, F., B. Kötz, E. Meier, K. I. Itten, B. Allgöwer. (2006). Estimation of LAI and fractional cover from small footprint airborne laser scanning data based on gap fraction. Remote Sensing of Environment, 104: 50-61.

Ørka, H. O., Næsset, E., & Bollandsås, O. M. (2009). Classifying species of individual trees by intensity and structure features derived from airborne laser scanner data. Remote Sensing of Environment, 113(6), 1163–1174. doi:10.1016/j.rse.2009.02.002

Parent, J.R., and Volin, J.C. 2014. Assessing the Potential for Leaf-off LiDAR Data to Model Canopy Closure in Temperate Deciduous Forests. ISPRS Journal of Photogrammetry and Remote Sensing 95: 134-145. DOI: 10.1016/j.isprsjprs.2014.06.009

Popescu, S. C. and Wynne, R. H. (2004). Seeing the Trees in the Forest: Using Lidar and Multispectral Data Fusion with Local Filtering and Variable Window Size for Estimating Tree Height. Photogrammetric Engineering & Remote Sensing, 70(5), 589–604.

Smith, M., J. Anderson, M. Fladeland. (2008). Chapter 14: Forest Canopy Structural Properties, in C.M. Hoover, ed., Media Field Measurements for Carbon Monitoring, Springer Science + Business Media B.V., p. 179-196.

Suárez, J. C., Ontiveros, C., Smith, S., & Snape, S. (2005). Use of airborne LiDAR and aerial photography in the estimation of individual tree heights in forestry. Computers & Geosciences, 31(2), 253–262. doi:10.1016/j.cageo.2004.09.015

Wasser, L., Day, R., Chasmer, L., & Taylor, A. (2013). Influence of vegetation structure on lidar-derived canopy height and fractional cover in forested riparian buffers during leaf-off and leaf-on conditions. PloS One, 8(1), 1-13. doi:10.1371/journal.pone.0054776

White, P.S. (1983). Corner's Rules in Eastern Deciduous Trees: Allometry and Its Implications for the Adaptive Architecture of Trees. Bulletin of the Torrey Botanical Club, 110 (2): 203-212.

Yao, W., Krzystek, P., & Heurich, M. (2012). Tree species classification and estimation of stem volume and DBH based on single tree extraction by exploiting airborne full-waveform LiDAR data. Remote Sensing of Environment, 123, 368–380. doi:10.1016/j.rse.2012.03.027

Chapter 3: Assessing the Potential for Leaf-off LiDAR Data to Model Canopy Closure in Temperate Deciduous Forests

3-1. Abstract

Estimates of canopy closure have many important uses in forest management and ecological research. Field measurements, however, are typically not practical to acquire over expansive areas or for large numbers of locations. This problem has been addressed, in recent years, through the use of airborne Light Detection and Ranging (LiDAR) technology which has proven effective in modeling canopy closure remotely. The techniques developed to use LiDAR for this purpose have been designed and evaluated for datasets acquired during leaf-on conditions. However, a large number of LiDAR datasets are acquired during leaf-off conditions since their primary purpose is to generate bare-earth Digital Elevation Models. In this paper, we develop and evaluate techniques for leveraging small-footprint leaf-off LiDAR data to model leaf-on canopy closure in temperate deciduous forests.

We evaluate three techniques for modeling canopy closure: 1) the *canopy-to-total-return-ratio (CTRR)*, 2) the *canopy-to-total-pixel-ratio (CTPR)*, and 3) the *hemispherical-viewshed (HV)*. The first technique has been used widely, in various forms, and has been shown to be effective with leaf-on LiDAR datasets. The CTRR technique that we tested uses the first-return LiDAR data only. The latter two techniques are new contributions that we develop and present in this paper. These techniques use canopy height models (CHM) to detect significant gaps in the forest canopy which are of primary importance in estimating closure.

The techniques we tested each showed good promise for predicting canopy closure using leaf-off LiDAR data with the CTPR and HV models having particularly high correlations with closure estimates from hemispherical photographs. The CTRR model had performance on par with results from previous studies that used leaf-on LiDAR, although, with leaf-off data the model tended to be negatively biased with respect to species having simple and compound leaf types and positively biased for coniferous species. The CTPR and HV models also showed some slight negative biases for compound-leaf species. The biases for the CTPR and HV models were mitigated when the CHM data were smoothed to fill in small gaps. The CHM-based models were robust to changes in the CHM model resolution which suggests that these methods may be applicable to a variety of small-footprint LiDAR datasets. In this research, the new CTPR and HV methods showed a strong ability to predict canopy closure using leaf-off data, however, future work will be needed to test the applicability of the models to variations in LiDAR datasets, forest types, and topography.

3-2. Introduction

Measurements of canopy structure have important uses in ecological research and in forest management. Canopy structure strongly influences ecological processes in the forest understory by affecting light availability and microclimate which are dominant factors in plant growth and survival (Canham et al. 1994; Pacala et al. 1994). Canopy closure is one metric that is commonly used in characterizing canopy structure and is defined as the proportion of the sky hemisphere obscured by vegetation when viewed from a single point (Jennings et al. 1999)[5]. This

[5] As other authors have noted, there remains confusion in the literature regarding the terms canopy closure, canopy cover, fractional cover, etc. These issues have been addressed in the literature (e.g. see Jenning et al. 1999) and are beyond the scope of this paper. We have carefully evaluated all studies cited in this paper to ensure that they are applicable to our research on canopy closure as defined in Jennings et al. (1999).

metric can be used to estimate light penetration into the forest understory and is an indicator of forest canopy density (Canham et al. 1990; Lieffers et al. 1999; Englund et al. 2000). Canopy closure is commonly used as an ecological indicator (Smith et al. 2008) and as a parameter in biosphere models (Turner et al. 2004, Bonan 1993).

Canopy closure is measured in the field using various instruments including quantum sensors and hemispherical photography (see Smith et al. 2008). For optimal results, field measurements must typically be made under the evenly diffuse sky lighting that occurs at dawn, dusk, or under uniformly overcast skies (Anderson 1964; Rich 1989; Whitmore et al. 1993). These restrictions on data collection make it difficult to collect large numbers of observations particularly in remote areas.

Airborne light detection and ranging (LiDAR) has made it possible to model canopy closure remotely and continuously across large areas (Lefsky et al. 1999). Several methods have been proposed to use LiDAR, acquired during leaf-on conditions, in modeling canopy closure. One common technique calculates canopy closure as the ratio of the number of canopy returns to the total number of returns for a given area (Riano et al. 2004, Morsdorf et al. 2006, Hopkinson and Chasmer 2007, Hopkinson and Chasmer 2009, Korhonen et al. 2011, Wasser et al. 2013[6])[7]. Canopy returns are defined as returns higher than a specified height threshold which is typically considered to be 1.3 meters. Some studies have found somewhat improved performance by restricting the return types used to either first- or last-return data (Morsdorf et al. 2006;

[6] Although Wasser et al. (2013) use the term fractional cover in their paper, their results show that they are modeling canopy closure according to the definition given by Jennings et al. (1999). They report their metric for annulus rings 1-6 which corresponds to zenith angles of $0\text{-}54^0$.

[7] In our review of these methods, we include Riano et al. (2004) and Morsdorf et al. (2006) who measured effective Leaf Area Index (LAI) rather than canopy closure. Sang et al. (2008) found effective LAI to be very highly correlated with canopy closure in forest environments and, thus, these studies support the use of the methods for canopy closure.

Hopkinson and Chasmer 2009). Hopkinson and Chasmer (2009) modeled canopy closure using LiDAR return intensity which is the amount of energy received by the LiDAR sensor for a given return. They estimated canopy closure from the ratio of the power of ground returns to the total power of the pulses for a given unit of area. An adjustment may be made to this ratio to account for power loss on the return trip of the pulse through the canopy. With this adjustment, the power ratio model has nearly a 1:1 relationship with field-based measurements and, unlike other techniques, needs little calibration (Hopkinson and Chasmer 2007, Hopkinson and Chasmer 2009). McLane et al. (2009) proposed a method that uses LiDAR profiles to estimate canopy closure over transects. They calculated canopy closure using forest profiles for which height was estimated continuously along transects with a linear interpolation method. Canopy closure was calculated for the transects as the ratio of overstory segment distance to understory segment distance with the overstory defined as having heights greater than 1.4 meters.

The LiDAR-based techniques, for modeling canopy closure, typically sample LiDAR returns within a circular analysis window that is centered on a given location-of-interest. The size of the analysis window should be large enough to provide an adequate sample of LiDAR points. Morsdorf et al. (2006) found that a circular window with a 15 meter radius was optimal whereas Riaño et al. (2004) found the ideal window radius tended to be approximately equal to the height of the forest canopy. Hopkinson and Chasmer (2009) achieved good success in their models using a window radius of 11.3 meters.

LiDAR data are most commonly acquired to generate bare-earth digital elevation models (DEM). LiDAR is most effective, in this regard, when the data are collected during leaf-off conditions because laser pulses are more likely to result in ground returns in deciduous forest areas. The ability to leverage leaf-off LiDAR in modeling canopy structure would greatly expand

the currently available data resources and allow forest terrain and canopy structure to be monitored more efficiently with the use of a single dataset. However, despite the potential benefit, we have not found any studies that have successfully used leaf-off LiDAR data to predict leaf-on canopy closure in a temperate deciduous forest. One published study attempted to model canopy closure, from leaf-off data, using a return-based technique but the effort was not successful (Wasser et al. 2013). The primary objective of this paper is to re-investigate the potential for leaf-off LiDAR to model leaf-on canopy closure and to propose new techniques by which leaf-off data can be leveraged for this purpose.

We hypothesize that a method based on a Canopy Height Model (CHM) will be more effective in modeling canopy closure than methods based on raw LiDAR returns. We expect a CHM-based closure model to be less sensitive to leaf-off conditions than return-based models. Laser pulses are more likely to penetrate leaf-off canopies and thus yield relatively fewer canopy returns which can bias canopy closure estimates. An individual pulse that passes unobstructed through the canopy, while its neighboring pulses do not, may indicate a very small gap between branches that is likely to be closed during leaf-on conditions. A CHM grid cell value is typically based on multiple LiDAR returns which can reduce the effects of isolated pulses that pass through very small gaps in the leaf-off canopy. Studies have found that leaf-off LiDAR is effective in deriving CHMs although tree heights tend to be underestimated (Wasser et al. 2013, Orka et al. 2010, Hill and Broughton 2009, Naesset 2005). A CHM used to estimate canopy closure would serve to detect canopy gaps and, thus, we suspect that small underestimates in height are unlikely to cause a problem for a canopy closure model. In this paper, we propose two methods of using a CHM to model canopy closure and compare these new methods to a return-based technique that has commonly been used in the literature. We test each method using leaf-

off LiDAR data and evaluate the methods for robustness to LiDAR data resolution, tree genus, and leaf type (i.e. simple, compound, and needle).

3-3. Methods

3-3.1. Study area

The study area for this research was located in eastern Connecticut, which is located in the northeastern United States and covers an area of approximately 4800 km^2 (Figure 3-1). This region is dominated by deciduous forests with oak/hickory (*Quercus spp*. and *Carya spp*.) and other hardwood forest types comprising the majority of forest land (Wharton et al. 2004). Elm/ash/red maple (*Ulmus spp.*, *Fraxinus spp.*, and *Acer rubrum*) and white/red pine (*Pinus strobus* and *Pinus resinosa*) forest types also cover significant areas (Wharton et al. 2004). Topography can be characterized as hilly with elevations ranging from sea level in the south to 330 meters in the north.

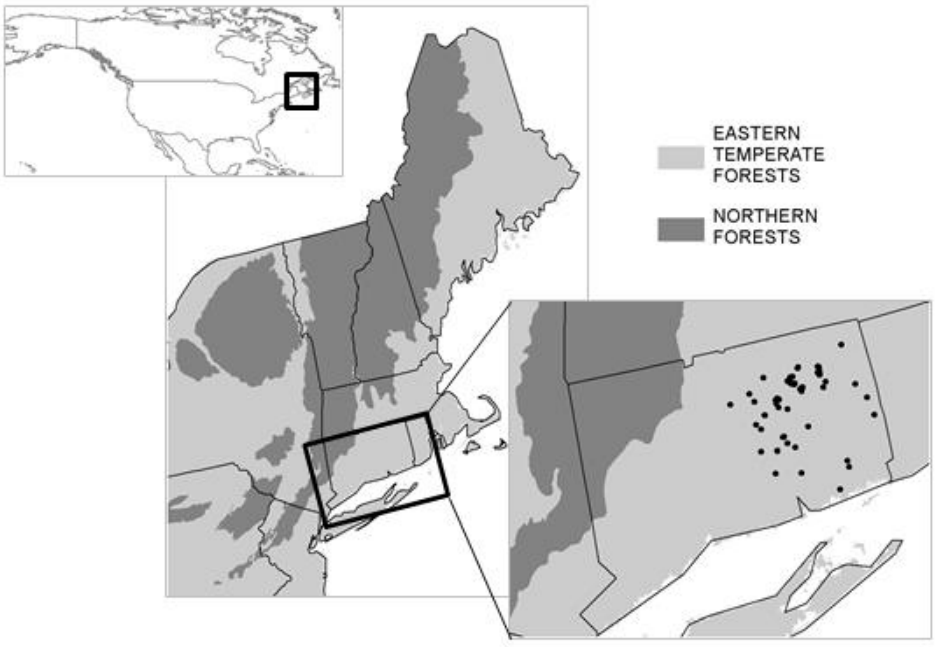

Figure 3-1: The forests of the northeastern USA are dominated by temperate deciduous and northern deciduous/coniferous forests (left). The field sites are located in the temperate forests of

eastern Connecticut (72.3° W, 41.7° N) (right). The black dots indicate locations of field sites (n=152).

3-3.2. Hemispherical photograph acquisition

Digital hemispherical photographs were obtained during three field surveys conducted during June and July of 2010, 2012, and 2013. Hemispherical photographs were collected from a single location at the center of each site using a Nikon 5000 camera with an FC-E8 lens. The camera was mounted on a tripod and leveled using a two-axis camera-mounted bubble level. Camera heights were either 1.4 or 2 meters above ground level[8] and locations directly under low, overhead branches were avoided. The camera exposure time was set to automatic and, whenever possible, photographs were taken under overcast conditions to help ensure diffuse light conditions. The sites were located at least 100 meters apart in or near mature forest stands and on relatively flat terrain. Field observations and high-resolution aerial imagery, acquired in 2010 and 2012, were used to confirm that no sites were located in areas that showed obvious signs of change in canopy structure within the past 3 years. The 2010, 2012, and 2013 field surveys included 36, 16, and 101 sites, respectively.

The field surveys differed in the techniques used to map the coordinates of the camera location. The 2010 survey obtained mapping-grade coordinates of the camera locations by using a Trimble Juno ST handheld GPS receiver[9]. For each camera location, 60 GPS readings were collected at 5 second intervals. The points were differentially-corrected, using a National Geodetic Survey continuously operating reference station located within 50 km of the sites, and averaged during post-processing using Trimble's Pathfinder Office software. Trimble reports the

[8] The 36 sites in the 2010 survey used a camera height of 1.4 m; all other sites used a camera height of 2 m.
[9] For instrument information, see http://www.trimble.com/junost.shtml

horizontal accuracy of the Juno receiver as 2-5 meters after post-processing which is on par with a 3rd party assessment that reported average RMSE values of around 4 meters for the Juno under closed tree canopies (Weih et al. 2009). All sites for the 2010 survey were located under closed forest canopies. The 2012 and 2013 surveys both obtained survey quality coordinates, with sub-meter accuracy, for the camera locations. The 2012 camera positions were located on National Geodetic Survey benchmarks which in previous research had been surveyed using a survey-grade Topcon GPS receiver with 6-hour static occupations (Arifuzzaman 2010). These sites had open or semi-open forest canopies with locations along or near forest edges. The horizontal position accuracies for these locations were on the order of a few centimeters. The 2013 survey obtained camera positions through geodetic traverses with a total station and survey-grade Sokkia GRX-1 GPS receiver. The GPS receiver was used to establish the two reference locations required to orient each traverse. The reference points were located in open fields and static GPS observations were collected at each location for at least 45 minutes. These data were post-processed with the Online Positioning User Service (OPUS)[10]. Traverses were made along roads or forest edges that intersected public forest lands. Hemispherical photographs were taken at locations in the forest approximately 20 meters from the forest edge. Camera positions were shifted as needed to be at a location visible to the total station.

The method of characterizing the forest type at each site also differed among the three field surveys. The 2010 and 2012 surveys were located in or near forest stands dominated by one or two tree genera. Although quantitative forest inventories were not conducted, the dominant species were estimated to comprise at least 70 percent of the basal area of the forest around each site (see Dreiss and Volin 2013). The stand types for these two surveys included oak/hickory

[10] See http://www.ngs.noaa.gov/OPUS/

(*Quercus spp.* and *Carya spp.*), sugar maple (*Acer saccharum*), quaking aspen (*Populus tremuloides*), white ash (*Fraxinus americana*), black locust (*Robinia pseudoacacia*), and pine/hemlock (*Pinus spp.* and *Tsuga canadensis*). For the 2013 survey, quantitative forest inventories were conducted for variable-radius plots centered at the hemispherical camera location. A wedge prism was used to identify trees that were located in each plot with each countable tree representing a fixed amount of basal area. The 2013 plots tended to consist of mixed deciduous species with oaks, maples, and hickories being major forest components.

3-3.3. Hemispherical photograph processing

The field surveys collected approximately 400 hemispherical photographs for the 152 field sites with all sites having 2-4 redundant images each taken with the camera's automatic exposure setting. Each image was checked for quality and discarded if over-exposure or excessive under-exposure was observed. The large number of hemispherical photographs made it necessary to use a semi-automated approach to classify the images. Therefore, we developed methods in ESRI's ArcGIS 10.1 that are analogous to the techniques used in standard software that specializes in hemispherical photograph classification, such as Gap Light Analyzer[11] or CAN-EYE[12]. Performing the analyses in ArcGIS allowed us to use Python scripts to automate much of the process while leveraging the more advanced image processing capabilities of ArcGIS.

3-3.3.1. Delineating the field-of-view (FOV)

The approximate position of the camera's optical center was identified from the hemispherical photographs by drawing a square bounding the extent of the hemispherical field-

[11] See http://www.caryinstitute.org/science-program/our-scientists/dr-charles-d-canham/gap-light-analyzer-gla
[12] see http://www6.paca.inra.fr/can-eye

of-view (FOV). Diagonal lines were drawn connecting the corners of the square and the intersection of the lines was taken to be the optical center. A circle was drawn with a diameter equal to the width of the square and centered on the approximate location of the optical center to delineate the image FOV (Figure 3-2). Our methods of identifying the optical center and delineating the FOV are analogous to the procedures used in the Gap Light Analysis software (see Frazer et al. 1999).

Figure 3-2: Illustration of the procedure used to circumscribe the field-of-view of a hemispherical photograph. The center of the image was located at the intersection of diagonal lines that connected the corners of a square bounding the field-of-view. The image center was used as the center of the circle with a radius equal to one-half the width of the square.

The Nikon FC-E8 hemispherical lens, used in this study, has been reported to have a nearly polar projection (Herbert 1987). Inoue et al. (2004) developed and applied a method to calibrate images from the FC-E8 lens and compared canopy closure estimates derived from both calibrated and uncalibrated images. Estimates from the calibrated and uncalibrated images were highly correlated ($r^2 = 0.99$, 1:1 relationship) with average and maximum differences of 0.66% and 1.58%, respectively (Inoue et al. 2004). Although these differences were found to be

statistically significant, we do not consider them to be of practical importance. Thus, we assumed the FC-E8 lens has a polar projection for which the radius of a ring (r) is related to its corresponding zenith angle (ϕ) as follows:

$$\frac{r}{R} = \frac{\phi}{90^{o}} \quad (1)$$

R is the radius of the entire FOV and 90° is the maximum possible zenith angle in a hemispherical image. We used this relationship to calculate the radius of a circle that corresponded to the zenith angles of 0-75° and created the circle by buffering our approximation of the image's optical center.

3-3.3.2. Classifying hemispherical images

Hemispherical image analysis software tends to use a single-band thresholding algorithm which has a limited ability to incorporate multiple spectral bands (Pueschel et al. 2012). The blue band is usually preferred when using a single band to classify hemispherical images because this part of the spectrum has been found to offer maximum contrast between sky and canopy (Jonckheere et al. 2005). However, the use of all three visible spectral bands (RGB) results in a better image classification than from the use of any single band, particularly in sunlit areas of the image (Jonckheere et al. 2005; Kucharick et al. 1997). The Iteratively Self Organizing Data (ISODATA) algorithm is a common tool in image classification for partitioning multispectral data into classes with spectrally similar properties (Tou and Gonzalez 1974). We used the ISODATA algorithm, in ArcGIS, to partition each hemispherical image into 20 classes. Each partitioned image was then overlain over the original image and examined to identify the class or classes that corresponded to sky. An image was discarded if any single class contained an unacceptable mix of sky and canopy pixels. Partitioned images were then reclassified into a

binary image depicting sky and canopy. Each binary image was clipped to the 0-75° FOV circle and canopy closure (CC) was calculated as:

$$CC = \frac{total\ pixels - sky\ pixels}{total\ pixels} \quad (2)$$

Canopy closure was calculated for each suitable image and closure values were averaged when redundant images were available for a given site.

3-3.3.3. Analyzing sensitivity of canopy closure to the accuracy of the optical center location

The optical center of the camera should serve theoretically as the center of the 0-75° FOV and errors in locating the optical center could affect the result of canopy closure calculations. Our methods can determine only the approximate location of the optic center; therefore, we tested the sensitivity of the canopy closure calculations to varying the position of the FOV center. We assumed that image center identified by our procedure has an error of less than 5° and we created a grid encompassing the area within a 5° radius of our image center. The center of the 0-75° FOV circle was iteratively shifted to the center of each of the 5,129 pixels within the 5° radius and canopy closure was calculated for the portion of the image that was contained within the circle. Our preliminary analyses showed that sites with low to moderate canopy closure are most affected by shifts in the location of the FOV center. Therefore, we performed this sensitivity analysis for the 16 sites located along a forest edge.

3-3.4. LiDAR data description and processing

The LiDAR data were acquired for nearly 4600 km^2 in eastern Connecticut during leaf-off conditions from November 3 – December 11, 2010 (Dewberry 2011). The data were

collected with a Leica ALS60 Airborne Laser Scanner[13] at an altitude of approximately 2000 meters above ground level. At this altitude, the ALS60's beam divergence of 0.22 millirads creates a footprint of roughly 44 cm on the ground. The scanner's pulse rate was 117.9 kHz and the flight line overlap was 50%. The data provider eliminated data with gaps between the geometrically usable portions of the swaths. The maximum scan angle of the sensor was 16.5° from nadir and it recorded up to 4 returns per laser pulse. The dataset has an overall density of 1.56 returns / m^2 with a maximum point spacing of 0.7 meters. The project's principle contractor processed the LiDAR data to create a bare-earth DEM, at a 1-meter resolution, with building features removed. Dewberry (2011) evaluated the accuracy of the DEM using 62 surveyed ground control points distributed through unvegetated, grass, and forested terrains. The vertical RMSE for the DEM, based on the ground control points, was estimated at 5 cm in non-vegetated terrain, 17 cm for grassy terrain, and 21 cm in forest terrain. The primary purpose of the LiDAR dataset was to develop the bare-earth DEM for use in conservation planning, floodplain mapping, dam safety assessments, and hydrological modeling (Dewberry 2011).

In this research, all processing and modeling of LiDAR data was performed using scripts written in Python v2.7 with ArcGIS 10.1. All statistical analyses were conducted in Python using SciPy v0.13 and Matplotlib v1.3.1. The LiDAR data were subset into 1 kilometer-squared tiles by the data vendor and the products we derived from the data corresponded to these tile areas.

3-3.5. Canopy height model

The new canopy closure modeling techniques that we propose rely on a CHM to distinguish between canopy and non-canopy pixels as well as determine whether features are tall

[13] see http://www.leica-geosystems.com/en/Leica-ALS60-Airborne-Laser-Scanner_57629.htm

enough to be in the FOV. We created a CHM by subtracting a bare-earth DEM from a digital surface model (DSM) that corresponded to the tree canopy. The DSM grid was aligned to the DEM and had the same 1 meter resolution. The pixel values for the DSM were calculated by taking the maximum of all non-ground first-return points within a given pixel. Because the overall density of the LiDAR dataset was 1.56 pts / m^2, the majority of non-water pixels in the DSM grid contained at least one first-return point. In small footprint LiDAR, airborne objects (e.g. large birds) can occasionally cause first-returns that do not correspond to features on the earth's surface. First-return points that contained obvious elevation anomalies were identified by comparing each point to all other first-return points within a 2.5 meter radius. If any first-return elevation was more than 30 meters higher than any of its neighbors, then the point was discarded. The 30-meter threshold was selected because it approximates the upper limit of canopy heights in northeastern forests and thus it represented a reasonable maximum elevation difference for points along forest gaps and edges. In the 52 1x1 km tiles that we used in this study, the percentage of DSM pixels without any first-return averaged 12.9% with a standard deviation of 3.4%. We assumed that data gaps larger than 3 meters in radius corresponded to bodies of water, which absorb LiDAR energy, and we assigned the bare-earth DEM values to the pixels in these gaps. For the remaining smaller data gaps, the fractions of the total small gap area with radii of ≤1, 1-2, and 2-3 meters were on average 0.91, 0.07, and 0.01, respectively. We interpolated the values for pixels in the DSM data gaps, smaller than 3 meters in radius, by taking the median of the known values in the pixels' eight nearest neighbors. Pixels with fewer than 3 known nearest neighbors were filled using a 2^{nd} or 3^{rd} interpolation pass.

The forest canopy creates a ceiling on a FOV; therefore, an estimate of the horizontal extent of a given hemispherical FOV must account for canopy height. We created a mean height

model to provide estimates of the canopy height at the locations of our field sites. The model was derived from the CHM using ArcGIS's focal statistics tool to calculate the average pixel height within a roving window. We only included pixels with heights taller than 3 meters in the average because shorter pixels are unlikely to be within a 0-75° FOV as we avoided taking hemispherical photographs directly under low branches. The mean height model was created using two passes of the focal statistics tool. The first pass used a window with a radius of 15 meters. A second pass, using a 25-meter radius window, was applied only to pixels that received a null data value from the first pass because the 15-meter window contained no pixels taller than 3 meters. The second pass was used to account for the larger horizontal extent of a 0-75° FOV in semi-open or open areas where there are no nearby trees to obstruct the FOV.

3-3.6. Modeling canopy closure with LiDAR

We tested three different approaches in modeling canopy closure: 1) the *canopy-to-total-return-ratio*, 2) the *canopy-to-total-pixel-ratio*, and 3) the *hemispherical-viewshed*. The first technique is based on the raw LiDAR returns and has been found to perform well in estimating canopy closure across a range of deciduous and coniferous forest types with leaf-on conditions (Riaño et al. 2004, Morsdorf et al. 2006, Hopkinson and Chasmer 2007, Hopkinson and Chasmer 2009, Korhonen et al. 2011, Wasser et al. 2013). We developed the latter two methods specifically for leaf-off LiDAR data. These methods use the canopy gaps, detectable by a CHM, to model canopy closure and to our knowledge they have not been attempted previously. We tested all three modeling approaches for the 0-75° zenith zone which is commonly used for estimating canopy closure.

3-3.6.1. Modeling canopy closure – the analysis window

Modeling canopy closure with the CHM-based closure models requires that the horizontal extent of the FOV be delineated and used as the analysis window within which canopy closure is calculated. The analysis window serves to normalize the CHM-based metrics; therefore, the window must accurately depict the on-the-ground projection of the FOV in order for model predictions to be comparable to the field-based measurements. Intuitively, the size of the analysis window should be based on the height of the overhead canopy because the FOV used for canopy closure measurements (i.e. 0-75°) has the shape of an inverted cone. The cone is truncated by any overhead visual obstructions; thus, the cross-sectional area of the cone's base depends on the height of the cone which is limited by the forest canopy. The theoretical radius (r) of the FOV can be calculated based on the canopy height (h) and the maximum zenith angle of interest (ϕ):

$$r = h \tan(\Phi) \qquad (3)$$

In our models, we use the mean canopy height model (see section 2.5) to provide the canopy height at a given location. We use equation 3 to determine the analysis window radius for the CHM-based methods only. For the return-based method, we found that using a window radius based on canopy height resulted in no significant improvement over using a fixed window radius. Unlike for the CHM-based methods, the analysis window for the return-based method does not need to precisely delineate the FOV because the window is only used to obtain a sample of LiDAR returns that is representative of the local canopy. For our data, the CTRR method was relatively insensitive to the window sizes between 10 and 20 meters.

3-3.6.2. The canopy-to-total-return-ratio (CTRR)

The *canopy-to-total-return-ratio* (CTRR) has been proposed and tested in previous studies and we use it in our research to provide a baseline for comparison to our new methods. The CTRR method is essentially a measure of the optical porosity of a canopy which can be a proxy for canopy closure. We calculated the CTRR as the fraction of LiDAR first-returns in the analysis window that correspond to the tree canopy. LiDAR first-return data are less likely to be affected by variations in LiDAR data acquisition parameters and studies have found that use of only first-returns has yielded better performance than when all returns are included (Morsdorf et al. 2006; Hopkinson and Chasmer 2009). We made the assumption that LiDAR returns with heights greater than 3 meters corresponded to the canopy and all other returns were considered to be non-canopy. This assumption was based on the observation that heights less than 3 meters were unlikely to be in the 0-75° FOV when the camera height is 2 meters and photographs are not taken directly under low branches. We calculated the CTRR using all first return points within a 15 meter radius of a given point of interest.

3-3.6.3. The canopy-to-total-pixel-ratio (CTPR)

The *canopy-to-total-pixel-ratio* (CTPR) is similar conceptually to the CTRR with the exception that it uses a CHM to distinguish canopy from non-canopy rather than using the raw LiDAR point data. We assumed that CHM pixels with heights greater than 3 meters corresponded to the canopy and all other pixels were non-canopy. An initial estimate of canopy closure was made for a given site by calculating the fraction of pixels within a 15 meter radius that were canopy pixels. The initial estimate was used to identify the site as being either closed

or open with an estimate above a threshold of 0.8[14] indicating a closed forest site and an estimate below the threshold indicating an open or semi-open site. Vegetation tends to obstruct the view at high zenith angles in a closed forest site whereas the view in an open or semi-open site tends to be relatively unobscured. Based on our preliminary tests, we used a maximum zenith angle of 60° for closed forest sites and a maximum angle of 75° for open sites. The maximum zenith angle, along with the local mean canopy height (section 2.5), was used to calculate the radius of a circular analysis window (eqn. 3) used in the final closure calculation. Closure was calculated as the fraction of this analysis window that consisted of canopy pixels.

3-3.6.4. The hemispherical viewshed (HV)

A circular analysis area is less likely to be valid when the desired FOV includes larger zenith angles. Wide-angle FOV's tend to not translate well into an on-the-ground area because the dimensions of the FOV at these oblique angles depend on the distances to the nearest features which can vary with direction (Figure 3-3). Also, for a given direction, the line-of-sight ends at the nearest solid feature. Thus, an on-the-ground projection for wide angle FOV's (i.e. zenith > 45°) circumscribes an area lacking tree cover and is not well suited as an analysis area for calculating canopy closure (Figure 3-3).

[14] The threshold was determined based on preliminary analyses for which the early version of the CTPR method tended to substantially underestimate the closure of sites with closures below 0.8.

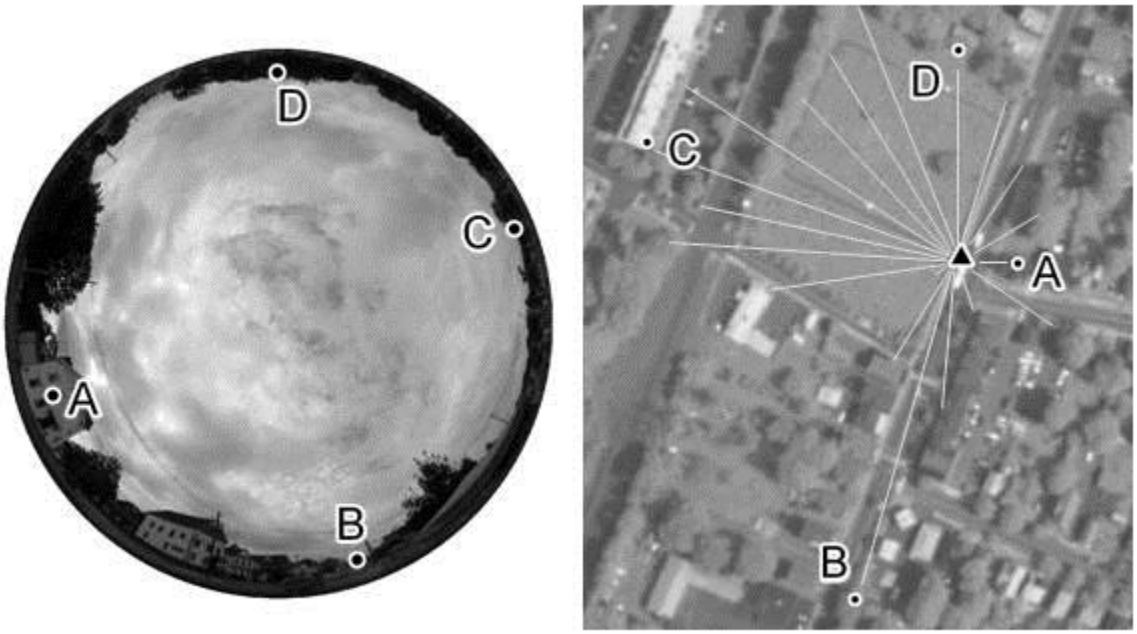

Figure 3-3: The shape and area of the on-the-ground projection of the hemispherical field-of-view depends on the proximities of the features visible in the image. This is clearly evident in the aerial image (right) which shows the location of a set of landmarks annotated on the hemispherical photograph (left). The approximate on-the-ground projection of the field-of-view is indicated, in the aerial image, by the radial lines originating at the camera location.

The *hemispherical-viewshed* (HV) method attempts to address more effectively the problem of defining an analysis window for hemispherical FOV's. This method consists of two parts; the first estimates canopy closure in the 0-45° zenith zone using a circular analysis window with a radius calculated from the local mean canopy height (section 3-3.5) and the maximum zenith of 45° (eq. 3). We considered canopy pixels to be all pixels taller than the minimum height needed to be visible in the overall 0-75° FOV. This minimum height (H_{min}) was calculated as:

$$H_{min} = \frac{d}{\tan \phi} - h_c \qquad (4)$$

where d is the distance to the location-of-interest, ϕ is the maximum zenith angle (i.e. 75°) in the overall FOV, and h_c is the camera height which we assumed to be 2 meters. We calculated canopy closure for the 0-45° zenith zone ($C_{0\text{-}45^\circ}$) as the ratio of canopy pixel area to the total area of the analysis window.

The second part of the *hemispherical-viewshed* method calculates canopy closure in the 45-75° zenith zone. In this zone, canopy closure is considered to be the fraction of directions in which lines-of-sight are blocked by features outside the radius of the 0-45° analysis window (Figure 3-4). The minimum height required for a given pixel to be visible in the 45-75° FOV was calculated using equation 3. Pixels with heights greater than the minimum were considered to be visually-obstructive pixels. The azimuths between the location-of-interest and each obstructive pixel were calculated. The angular width (σ) of each of these pixels was calculated as:

$$\sigma = 2 \text{ atan } (w / 2d) \qquad (5)$$

where d is the distance to the location-of-interest and w is the pixel width. The azimuths and angular widths were rounded off to the nearest whole degree. The number of degrees of azimuth for which lines-of-sight are blocked by a given pixel was calculated as the azimuth plus or minus one-half the angular width. The canopy closure ($C_{45\text{-}75^\circ}$) was calculated as the fraction of azimuths with blocked lines of site.

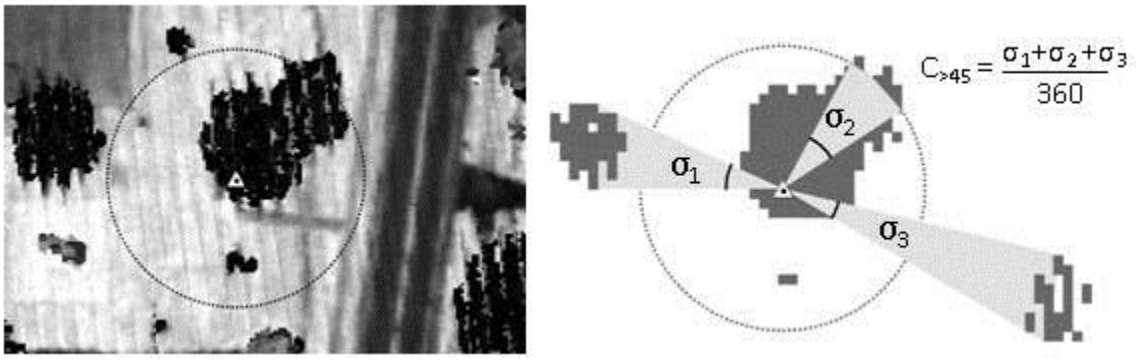

Figure 3-4: Canopy closure, for the >45° zenith zone, is calculated as the fraction of azimuths that are blocked by pixels outside the 0-45° analysis window (dotted circle). Trees appear as groups of dark pixels in the LiDAR return intensity image (left). In the image to the right, dark gray pixels are taller than the minimum height needed to be visible in the viewshed (see eqn. 3) and light gray cones indicate lines-of-sight obstructed by pixels outside the 0-45° analysis window.

The canopy closures for the 0-45° and the 45-75° zenith zones were combined into an overall canopy closure ($C_{0\text{-}75^o}$) using a linear weighted combination with weights ($W_{0\text{-}45^o}$, $W_{45\text{-}75^o}$) equal to the proportion of area within each zone, such that:

$$C_{0\text{-}75^0} = (C_{0\text{-}45^0} * W_{0\text{-}45^0}) + (C_{45\text{-}75^0} * W_{45\text{-}75^0}) \quad (6)$$

In the polar projection of a hemispherical photograph, 36% and 64% of the area are contained within the 0-45° and 45-75° zones, respectively. Thus, we used values of 0.36 and 0.64 for $W_{0\text{-}45^0}$ and $W_{45\text{-}75^0}$, respectively.

3-3.6.5. Assessing and mitigating errors in position measurements

The 2-5 meter accuracy level of the Juno GPS receiver was a potential source of error for the models because the true site coordinates could be off by as much as 5 meters from the measured coordinates. To evaluate and mitigate GPS errors, we modeled canopy closure for all pixels within 5 meters of the 36 locations measured with the Juno receivers. Variations in closure estimates, within these error zones, were evaluated and the mean canopy closure values were

used in the validation of each model. The sub-meter coordinate accuracies of the remaining 116 sites are well below the resolution of the models and, thus, the model values at the GPS coordinates were used in model validation.

3-3.6.6. Sensitivity of CTPR and HV to CHM resolution

The characteristics of airborne LiDAR datasets can vary with the mission and sensor specifications used during acquisition. These characteristics can potentially have significant effects on the performance of canopy closure models. Thus, we tested the robustness of the CHM-based canopy closure models to variations in LiDAR datasets. The point-based models have been thoroughly evaluated in the literature, using various LiDAR datasets, and because the focus of this study is on the CHM-based models, we do not test the robustness of CTRR to variations in LiDAR datasets.

The main consequence for the CHM-based canopy closure models, that we perceived would result from variations in LiDAR datasets, is in the resolution of the CHM that can be derived from the data (see section 4). To simulate this consequence, we used the 1 meter CHM to generate CHMs with pixel sizes of 2, 4, 6, 8, and 10 meters. To degrade the resolution of the original CHM, we created grids with the desired pixel sizes and aligned to the original CHM. We randomly selected a value from a single 1 meter pixel that coincided with the larger pixel and this value was assigned to the larger pixel. The CTPR and HV methods were tested on the CHMs that were resampled to coarser resolutions.

3-3.6.7. Effect of CHM smoothing on CTPR and HV

LiDAR pulses penetrate a forest canopy more readily during leaf-off conditions and a CHM derived from leaf-off data may be expected to contain “false gaps” resulting from pulses

that pass through small spaces between branches that would be blocked during leaf-on conditions. We hypothesized that false gaps could be mitigated by smoothing the CHM prior to its use in calculating canopy closure. Thus we smoothed the 1-meter CHM using a circular window in ArcGIS's focal statistics tool. The average value of the pixels that fell within the roving window was used as the new value for the pixel at the center of the window. We created 3 smoothed CHMs using windows with radii of 1, 2, and 3 meters. The CTPR and HV methods were tested on each of these smoothed CHMs.

3-4. Results

The canopy closure in the field sites, as determined from hemispherical photographs, spanned the full range of values, from 0.0 to approximately 1.0 (Figure 3-5). The sites had predominantly closed forest canopies with only 23 of the 153 sites having closures less than 0.8. This heteroscedasticity was addressed in our model evaluations by using cross validation analyses to assess the consistency of model performance with varying sets of training data.

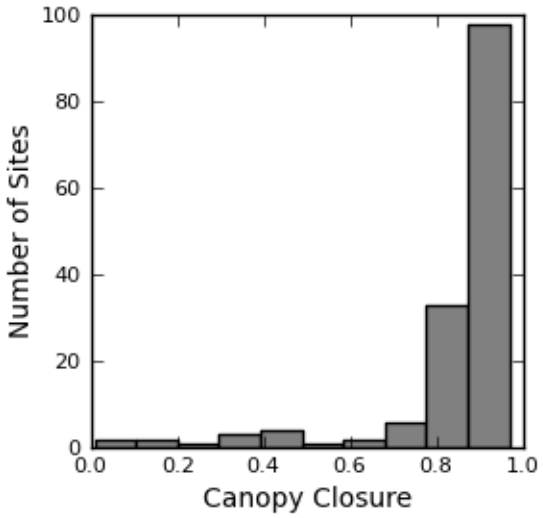

Figure 3-5: The canopy closure for the 152 field sites (as measured from hemispherical photographs) covers the full range from 0.0 to 1.0.

The error in our approximation of the optical center is likely to have had a negligible effect on the canopy closure calculated from the hemispherical photographs. For the 16 field sites located along forest edges, canopy closure varied little as the FOV center was shifted within a 5° radius of our approximated optical center. The standard deviations for closure values within the 5° radius ranged from 0.00 to 0.02 with a mean deviation of 0.01. The maximum range of closure values for any of the 16 sites was 0.07. Errors in the FOV center can be expected to have even less of an impact for closed canopy sites.

LiDAR predictions of canopy closure are not likely to be significantly affected by the 2-5 meter error of the Juno GPS receivers. The CTPR and HV models showed little variation for locations within 5-meters of the coordinates reported for the 36 sites mapped by the Juno receivers. The average standard deviation and average range of closures within the 5-meter buffers was 0.011 and 0.027, respectively, for the CTPR model. The average standard deviation and range of closures for the HV model was 0.002 and 0.004, respectively.

3-4.1. The canopy-to-total-return-ratio

The linear regression model for CTRR method had an $r^2 = 0.67$ and RMSE = 0.10 (Figure 3-6). Performance was consistent in a 4-fold cross-validation analysis with only slight variation in r^2 and no variation in RMSE (Table 3-1). Model slopes ranged from 0.72-0.84 and the y-intercept varied from 0.27-0.36 (Table 3-1). The model significantly underestimated closure for sites in which more than 60% of the basal area consisted of tree species with compound-leaves ($p = 0.02$) or simple-leaves ($p = 0.03$) (Figure 3-7). The model also significantly overestimated closure for sites dominated by coniferous species ($p=0.002$) (Figure 3-7). The model residuals had positive correlations with the basal areas of *Pinus spp.* ($r=0.80$)

and *Tsuga spp.* (r = 0.40) (Table 3-2). This positive correlation indicates that closure is increasingly overestimated as the basal area of a site becomes more dominated by a given genus. Negative correlations were found between the residuals and basal area of *Betula* (r= -0.46), *Fraxinus* (r= -0.48), and *Populus* (r= -0.39) species.

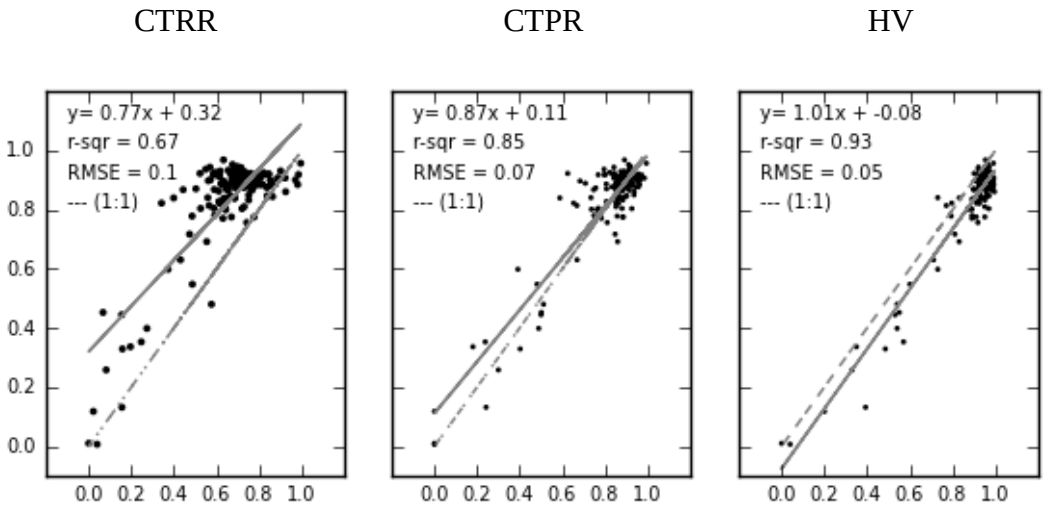

Figure 3-6: Linear regression models for the CTRR, CTPR, and HV methods.

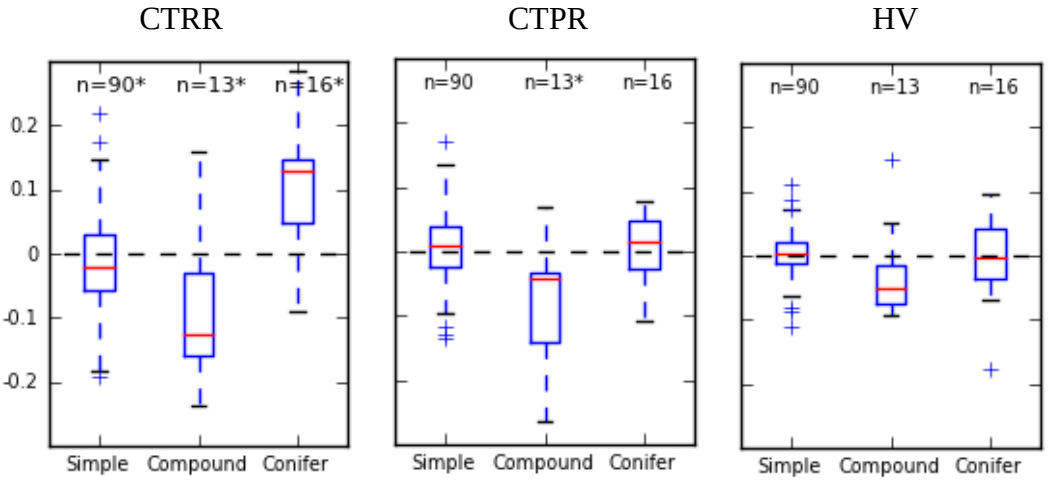

Figure 3-7: Residual boxplots for the CTRR, CTPR, and HV models. * indicates the residuals are significantly different than zero with 95% confidence. The CTPR and HV models are based on the unsmoothed, 1-meter CHM. The sites included for each leaf type had at least 60% of the basal area that was comprised of species exhibiting a given leaf type.

Table 3-1: Parameters of linear regression models created in a 4-fold cross validation analysis. Results for the CTPR and HV models are based on a 1-meter unsmoothed CHM.

CTRR				CTPR				HV			
m	***b***	***r^2***	***RMSE***	***m***	***b***	***r^2***	***RMSE***	***m***	***b***	***r^2***	***RMSE***
0.84	0.27	0.74	0.10	0.88	0.10	0.88	0.07	1.02	-0.08	0.93	0.05
0.77	0.32	0.65	0.10	0.87	0.12	0.84	0.07	1.04	-0.11	0.92	0.05
0.74	0.34	0.66	0.10	0.89	0.10	0.82	0.07	1.00	-0.07	0.92	0.04
0.72	0.36	0.64	0.10	0.84	0.14	0.85	0.07	0.99	-0.06	0.94	0.05

3-4.2. The canopy-to-total-pixel-ratio

The CTPR model performance was intermediate with respect to the CTRR and HV models. The CTPR model had an $r^2 = 0.85$ and RMSE = 0.07 with a slope of 0.87 and y-intercept of 0.11 (Figure 3-6). The model performed consistently in the cross validation analysis with the slope varying from 0.84-0.89, the y-intercept varying from 0.10-0.14, the r^2 from 0.82-0.88, and the RMSE remained at 0.07 (Table 3-1). Closure was significantly underestimated for sites dominated by compound-leaf species (p=0.01) while there were no significant biases for simple-leaf (p=0.08) or conifer species (p = 0.80) (Figure 3-7). Residuals were negatively correlated with the basal area of *Fraxinus spp.* (r = -0.65), *Betula spp.* (r = -0.43), and *Carya spp.* (r = -0.36) but no strong correlations were found for any other genera (Table 3-2).

The performance of the CTPR model was improved by smoothing the CHM prior to calculating canopy closure. The model created from a CHM smoothed by a 1-meter radius window had an $r^2 = 0.91$ and RMSE = 0.05 (Table 3-3). The performance improved slightly further when a 2-meter radius window was used to smooth the CHM; the model had an $r^2 = 0.92$ and RMSE = 0.05 (Table 3-3, Figure 3-8). Smoothing the CHM reduced the residual bias for compound-leaf species and there were no significant biases for any leaf type when the CTPR model used a CHM smoothed using a window of 2 meters in radius (Figure 3-8).

The CTPR method was very robust to changes in the CHM resolution (Table 3-4) and model performance declined gradually with increasing CHM pixel size up to 10 meters. The CTPR model based on a CHM with a 2 meter resolution had an $r^2 = 0.82$ and RMSE's of 0.08. When using a 10-meter CHM, the CTPR model had an $r^2 = 0.60$ and RMSE = 0.11 (Table 3-4).

Table 3-2: Spearman tests for correlations between residuals and leaf type or genus. The sites included for each leaf type or genus had at least 10% of the basal area that was comprised of species exhibiting a given leaf type or genus.

Leaf type / Genus	n	CTRR		CTPR		HV	
		r	P	r	p	r	p
Simple	121	0.13	0.17	0.12	0.21	0.01	0.89
Compound	51	0.39	0.00	-0.43	0.00	-0.26	0.07
Needle	45	-0.47	0.00	0.07	0.63	-0.06	0.70
Betula	18	-0.46	0.05	-0.43	0.08	-0.15	0.56
Fraxinus	12	-0.48	0.23	-0.65	0.02	-0.45	0.15
Tsuga	17	0.40	0.11	0.22	0.40	-0.09	0.73
Pinus	20	0.80	0.0	0.00	0.99	-0.01	0.96
Populus	9	-0.39	0.30	0.23	0.56	0.32	0.40
Acer	62	-0.11	0.42	0.00	0.99	0.06	0.63
Carya	29	-0.25	0.20	-0.36	0.06	-0.05	0.80
Quercus	76	-0.05	0.65	0.00	0.99	0.03	0.82

Table 3-3: Regression coefficients and performances of CTPR and HV models based on a smoothed CHM.

Window radius	**CTPR**				**HV**			
	m	***b***	***r^2***	***RMSE***	***m***	***b***	***r^2***	***RMSE***
0	0.87	0.11	0.85	0.07	1.01	-0.08	0.93	0.05
1	0.83	0.09	0.91	0.05	0.93	-0.02	0.95	0.04
2	0.82	0.08	0.92	0.05	0.93	-0.03	0.95	0.04

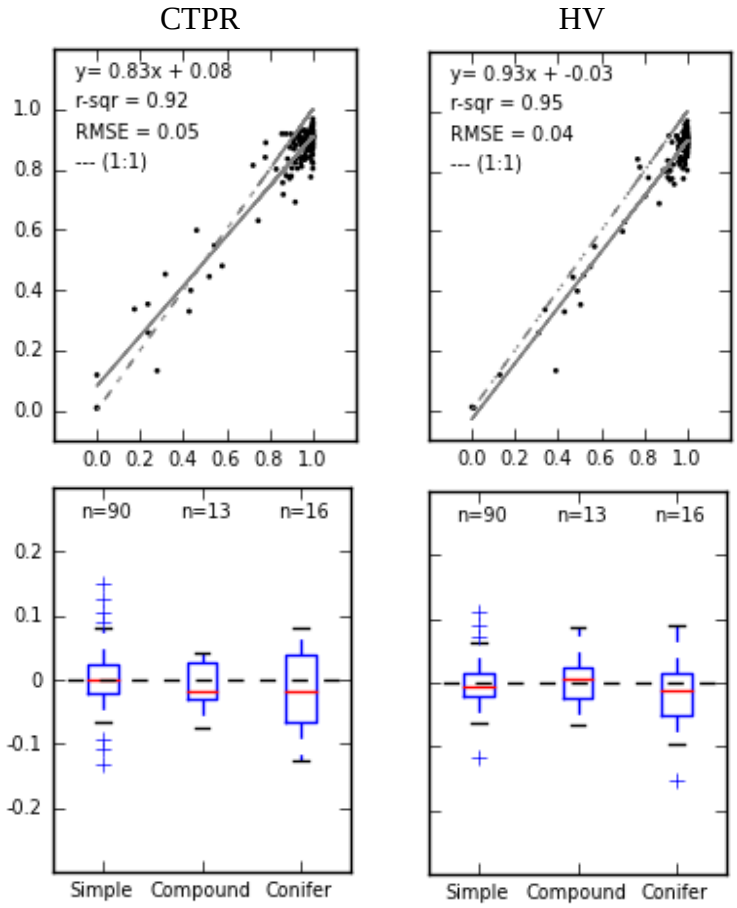

Figure 3-8: Linear regression models and residual boxplots, by leaf type, for the CTPR and HV methods based on a CHM smoothed by a 2 meter filter. The models did not have any significant residual biases. The sites included for each leaf type had at least 60% of the basal area that was comprised of species exhibiting a given leaf type.

Table 3-4: Regression coefficients and performances for CTPR and HV models using CHM's of varying spatial resolutions. Models are presented for 3 CHM's, at each pixel resolution, which were derived by randomly sampling a value from coincident pixels of the 1 meter CHM.

CHM pixel size	**CTPR**				**HV**			
	m	***b***	***r^2***	***RMSE***	***m***	***b***	***r^2***	***RMSE***
1	0.87	0.11	0.85	0.07	1.01	-0.08	0.93	0.05
2	0.86	0.13	0.82	0.08	0.83	0.09	0.83	0.07
4	0.78	0.20	0.74	0.09	0.79	0.13	0.82	0.08
6	0.78	0.21	0.72	0.10	0.74	0.21	0.80	0.08
8	0.75	0.22	0.69	0.10	0.73	0.25	0.78	0.08
10	0.68	0.29	0.60	0.11	0.63	0.41	0.57	0.12

3-4.3. The hemispherical viewshed

The HV model had the best performance of all the methods with an r^2 of 0.93 and RMSE of 0.05 (Figure 3-6). The regression model had a nearly 1:1 relationship between the canopy closures estimated from LiDAR and the hemispherical photographs with a slope of 1.01 and y-intercept of -0.08. The model was very consistent in cross validation analysis with only slight variations in the regression coefficients, r^2, and RMSE (Table 3-1). Model residuals for sites dominated by compound-leaf species (basal area > 60 percent) were slightly underestimated but the bias was not significant (p=0.06) (Figure 3-7). There were no significant biases in model residuals for sites dominated by simple-leaf (p=0.51) or needle-bearing species (p=0.76) (Figure 3-7). Model residuals tended to be negatively correlated with *Fraxinus spp.* (r = -0.45) and positively correlated with basal area for *Populus spp*. (r = 0.32). No strong correlations were found between the residuals and the basal area of any other genus (Table 3-2).

Smoothing the CHM improved the HV model slightly with $r^2 = 0.95$ and RMSE = 0.04 when the CHM was smoothed with a 1- or 2-meter window (Table 3-3, Figure 3-8). The residual bias for compound-leaf species was reduced slightly by the smoothing the CHM. There was no change in model performance when the radius of the smoothing window was increased from 1 to 2 meters.

The HV model performance declined sharply as the CHM pixel size was increased to 2 meters with an corresponding $r^2 = 0.83$ and RMSE = 0.07 (Table 3-4). The decline in performance was more gradual as CHM pixel size increased from 2 to 8 meters with $r^2 = 0.78$ and RMSE = 0.08 for the model based on the 8 meter CHM. Performance declined again sharply for the 10 meter CHM for which $r^2 = 0.57$ and RMSE = 0.12 (Table 3-4).

3-5. Discussion

The CTRR and CTPR methods can be considered proxies for canopy closure because they consider an above-canopy planar view rather than an on-the-ground hemispherical FOV. These methods essentially measure the ability of LiDAR pulses to penetrate the canopy in an area that coincides with the approximate extent of the on-the-ground hemispherical FOV. One would expect these measures to have some degree of correlation with canopy closure and our data have provided empirical support for this expectation. As discussed in section 2.6.4, the analysis areas used by the CTRR and CTPR methods do not correspond well to a ground-based hemispherical FOV for zenith angles that approach the horizon. However, this is typically not a major concern for interior forest areas because lines-of-sight for the larger zenith angles are almost always obstructed by the canopy. Thus, for interior forest sites the FOV is typically limited to the smaller zenith angles for which the CTRR and CTPR methods are better suited. The two phase approach of the CTPR method allows it to adjust the analysis area, based on an initial closure estimate, to compensate for sites that are located in more open forest conditions. Broadening the FOV for more open forest sites allows the CTPR method to out-perform the CTRR method for sites located near forest edges. The HV method more directly simulates a ground-based hemispherical FOV and thus has the best performance, of the three models, for open forest sites.

The application of the CTRR method to leaf-off LiDAR data, in this study, has yielded a model with a performance similar to those achieved by other studies which applied the same method to leaf-on LiDAR data (Hopkinson and Chasmer 2009; Morsdorf 2006). Wasser et al. (2013), however, used a similar method to calculate canopy closure from leaf-off LiDAR data in a deciduous forest area but found no relationship between the LiDAR predictions and the field-

based measurements of canopy closure. The authors suggest that the lack of a significant relationship may be due to the narrow range of canopy closures (60-90%) sampled in their study. Our observations support this suggestion because we would have been unlikely to find a significant relationship in our CTRR model without the inclusion of sites with moderate and low canopy closure.

The CHM-based methods depend primarily on a CHMs capability to distinguish gaps from tree canopies and to a lesser degree on the accuracy with which the CHM estimates canopy height. Depending on the resolution of the CHM and the point spacing of the LiDAR dataset, the pixel values of a CHM may be determined from a single LiDAR return. Even though small-footprint LiDAR is likely to sample only a fraction of a given CHM pixel, it is sufficient because a forest canopy has a high degree of spatial auto-correlation as evident from hemispherical photographs[15]. Thus, if LiDAR detects canopy or a lack of canopy at a given location, then it is likely that the area in the immediate vicinity is the same. Canopy gaps that are smaller than the average spacing between LiDAR points, or smaller than the CHM resolution, cannot be resolved. However, it is the larger gaps that have the primary effect on the closure of the canopy as evident in the observation that temperate forest understories, beneath closed canopies, typically receive less than 5% of full sunlight (Dreiss and Volin 2013; Canham et al. 1990). Although a CHM is unlikely to detect the very small gaps that allow the light to penetrate closed canopies, these gaps have a minor contribution to overall canopy closure.

[15] We used the Moran's I metric, in ArcGIS, to test the spatial auto-correlation in the binary classifications of hemispherical photographs for a sample of forest edge and interior sites. The results confirmed that canopy and sky pixels were highly clustered, however, presenting the results of this analysis is beyond the scope of this paper.

The characteristics of LiDAR datasets can vary substantially depending on the parameters of the mission in which the data were acquired. The laser scanner frequency, aircraft altitude, and aircraft speed affect the ability of the laser pulses to penetrate the forest canopy as well as the spacing of the LiDAR returns (Gatziolis and Anderson 2008). Goodwin et al. (2006) found that aircraft altitude (1000-3000 m) and pulse footprint size (0.2-0.6 m) had no significant effect on canopy height profiles for topographically and structurally differing sites. Other studies have found that aircraft height, pulse power, scan frequency, and footprint diameter can have a significant effect on estimates of maximum canopy height but the reported differences have been relatively minor ranging from 0.1 to 0.6 meters (Nasset 2004, Chasmer et al. 2006, Hopkinson 2007). However, LiDAR mission parameters can significantly affect the spacing of the LiDAR returns which is a major practical consideration for modeling canopy height. Interpolation should typically be minimized in deriving a CHM from LiDAR point data because it has been shown to create artificially smoothed CHMs that are a poorer representation of the canopy top than CHMs created using non-interpolation techniques (Wasser et al. 2013). Minimizing interpolation requires that the CHM pixel size is somewhat larger than the maximum point spacing of the LiDAR dataset to ensure that the majority of CHM pixels contain at least one LiDAR point. Thus, with regard to CHMs, a primary consequence of the variations among LiDAR datasets is in limiting the maximum spatial resolution that can be attained.

The minimum size of the canopy gaps that can be detected by a CHM increases with the spatial resolution of the CHM and can be expected to affect the performance of CHM-based canopy closure models. However, the CHM-based methods that we presented have proven to be fairly robust when applied to CHMs with a coarse spatial resolution and good performance was maintained even with CHM pixels sizes of several meters. The robustness of these models

despite coarse CHM resolutions supports our suspicion that small canopy gaps are not of primary importance in estimating canopy closure. Furthermore, our findings suggest that the CHM-methods should be generally applicable for small-footprint LiDAR datasets.

The residual biases for each of the models fit our expectations for using leaf-off LiDAR data to model leaf-on canopy closure. Each of the three methods we discussed in this paper tended to underestimate canopy closure for compound-leaf species. The CTRR model also slightly underestimated closure for simple-leaf species and overestimated closure for coniferous species. Leaf-off LiDAR can be expected to underestimate closure for deciduous trees because laser pulses are more likely to pass between branches and reach the ground unobstructed than in a leaf-on canopy. The larger proportion of laser pulses in which the first-returns occur below the tree canopy creates false gaps that are due to the leaf-off condition rather than to an actual canopy gap. These false gaps make the canopy appear to have lower closure and the problem is magnified for species with compound leaves which tend to have a lower spatial density of branches as a result of their larger leaves (White 1983). The CHM-based closure models were less sensitive to false gaps because multiple LiDAR points typically fell into a single CHM pixel. The LiDAR pulses that would create false gaps are less likely to influence the pixel height because the maximum of the LiDAR points, in a given pixel, are used for the pixel value. The closure models based on a smoothed CHM had no residual bias regardless of whether species had simple- or compound-leaves or needles. Smoothing the CHM by averaging the values around a given pixel apparently removed the false gaps that resulted in underestimates of simple- and compound-leaved species. However, smoothing is unlikely to be appropriate for coarse resolution CHMs as information on true canopy gaps is likely to be lost.

A CHM based on leaf-off LiDAR data tends to underestimate the height of deciduous trees, compared to a leaf-on CHM, because of the lower density of canopy biomass. Orka et al. (2010) found that height estimates for aspen (*Populus tremula*) were an average of 55 cm lower when using leaf-off data as compared to leaf-on data whereas they found no significant difference for birch species (*Betula spp.*). Wasser et al. (2013) found that heights of deciduous trees estimated using leaf-off LiDAR were an average of 1.4 meters lower than estimates from leaf-on LiDAR. Underestimates of height in a CHM are likely to have a negligible effect on the performance of CHM-based closure models when applied to mature forests. The height in the CHM is used simply to determine if a pixel is within the 0-75° FOV. In a forest where the canopy is substantially taller than 3 meters, there should be relatively few borderline pixels that would be affected by an underestimate in height. Height biases would be more problematic in very young forests where canopy heights are close to the 3 meter threshold that is used to distinguish between canopy and non-canopy pixels. The fairly small differences between leaf-on and leaf-off CHMs suggests that the CHM-based models would perform similarly well with leaf-on CHMs.

The relatively flat terrain of our study sites did not permit the development or testing of the models for uneven terrain. At present, the CHM-based techniques only account for height and, therefore, it is possible that the performance of these models will be negatively affected on or near steep slopes. The *hemispherical-viewshed* may be particularly susceptible because elevation would be an important factor in identifying which features are visible in the FOV. The minimum heights required to be in the FOV would be overestimated for upslope areas and underestimated for down-slope areas with the magnitude of the error directly related to the degree of slope. The minimum height equation (eqn. 4) should be easily modified to account for

terrain by adding a term that is the difference in elevation between the location of interest and a given pixel in the analysis area. However, further research is needed to assess the effect of terrain on the performance of the CHM-based models.

3-6. Conclusions

In this paper, we have evaluated three methods for modeling canopy closure, the proportion of the sky hemisphere obscured by vegetation when viewed from a single point (Jennings et al. 1999). Each of these methods have shown good potential for using leaf-off LiDAR data to predict leaf-on canopy closure in mature deciduous forests. The return-based method had the greatest biases with regard to leaf type although each of the models tended to underestimate closure for sites dominated by compound-leaf species. The biases in the CHM-based models were mitigated when the CHM was smoothed prior to use in the canopy closure model. However, smoothing the CHM is only likely to be effective when the CHM has a small pixel size. The CHM-based closure models proved to be fairly robust to the size of the CHM pixels with fairly gradual declines in performance as the CHM pixel size increased to 10 meters. The ability of the CHM-based methods to perform well with coarse resolution data and the consistencies that previous work has found between leaf-on and leaf-off CHMs suggest that these methods may be generally applicable to small-footprint LiDAR datasets acquired during leaf-off or leaf-on conditions. However, further research is needed to test the applicability of the CHM-based methods for a variety of discrete-return LiDAR datasets, CHM creation methods, forest types, and terrains. The ability to use leaf-off LiDAR in analyzing canopy structure would reduce the need for leaf-on data and thereby improve the efficiency with which forest resources can be monitored.

3-7. Acknowledgements

The authors would like to acknowledge Lindsay Dreiss, Jinwon Chung, and Thomas Meyer for the use of their field data in validating our models. We also acknowledge Qian Lei, Elliot Olivas, Michael Heyn, Kyle Arvisais, Mathew Solmo, Gabe Sipson, Bojan Bojic, Malcom Smith, Lindsay Chateauvert, and Michael Kelly for their work in field surveys during which data for this study were collected. Field work was supported, in part, by Northeast Utilities. We thank the Natural Resources Conservation Service for making their LiDAR data available to us. We also thank Qian Lei, Chadwick Rittenhouse, and Daniel Civco for their helpful reviews of this manuscript.

3-8. References

Anderson, M.C. (1964). Light Relations of Terrestrial Plant Communities and Their Measurement. Biological Reviews, 39(4): 425-481.

Arifuzzaman, K. (2010). Accuracy Assessment of GEOID09 and GEOID03 in Connecticut. University of Connecticut. ProQuest Dissertations & Theses (930241826). 84p.

Black, T.A., Chen, J.M., Lee, X.H., Sagar, R.M. (1991). Characteristics of shortwave and longwave irradiances under douglas-fir forest stand. Canadian Journal of Forest Research, 21: 1020-1028.

Bonan, G. B. (1993). Importance of leaf area index and forest type when estimating photosynthesis in boreal forests. Remote Sensing of Environment, 43(3): 303–314.

Brandtberg T, Warner TA, Landenberger RE, McGraw JB. (2003). Detection and analysis of individual leaf-off tree crowns in small footprint, high sampling density lidar data from the eastern deciduous forest in North America. Remote Sensing of Environment, 85: 290–303.

Canham C.D., A.C. Finzi, S.W. Pacala, D.H. Burbank. (1994). Causes and consequences of resource heterogeneity in forests: interspecific variation in light transmission by canopy trees. Canadian Journal of Forest Research, 24, 337–349.

Canham, C.D., J.S. Denslow, W.J. Platt, J.R. Runkle, T.A. Spies, P.S. White. (1990). Light regimes beneath closed canopies and tree-fall gaps in temperate and tropical forests. Canadian Journal of Forest Research, 20: 620–631.

Chasmer, L.E., Hopkinson, C., Smith, B., Treitz, P. (2006). Examining the influence of changing laser pulse repetition frequencies on conifer forest canopy returns. Photogrammetric Engineering and Remote Sensing. 72 (12) 1359-1367.

Chen, J.M. and T.A. Black. (1992). Defining leaf area index for non-flat leaves. Plant Cell and Environment, 15: 421-429.

Dewberry. (2011). Project Report for the U.S. Corp of Engineers High Resolution LiDAR Acquisition & Processing for Portions of Connecticut. USACE Contract W912P9-10-D-0534. Prepared by Dewberry. 71 pp.

Dreiss, L.M. and J.C. Volin. (2013). Influence of leaf phenology and site nitrogen on invasive species establishment in temperate deciduous forest understories. Forest Ecology and Management 296: 1-8.

Englund, S.R., O'Brien, J.J., Clark, D.B. (2000). Evaluation of digital and film hemispherical photography and spherical densiometry for measuring forest light environments. Canadian Journal of Forest Research, 30: 1999–2005.

Frazer, G.W., Canham, C.D., and Lertzman, K.P. (1999). Gap Light Analyzer (GLA), Version 2.0: Imaging software to extract canopy structure and gap light transmission indices from true-colour fisheye photographs, users manual and program documentation. Copyright © 1999: Simon Fraser University, Burnaby, British Columbia, and the Institute of Ecosystem Studies, Millbrook, New York.

Gatziolis, D., and Andersen, H. (2008). A Guide to LIDAR Data Acquisition and Processing for the Forests of the Pacific Northwest, USDA Forest Service. General Technical Report PNW-GTR-768.

Goodwin, N. R., Coops, N. C., & Culvenor, D. S. (2006). Assessment of forest structure with airborne LiDAR and the effects of platform altitude. *Remote Sensing of Environment, 103*(2), 140–152. doi:10.1016/j.rse.2006.03.003

Herbert, T.J. (1987). Area projection of fisheye photographic lenses. Agriculture and Forest Meteorology, 39: 215–223.

Hill, R. A. and R.K. Broughton (2009). Mapping the understorey of deciduous woodland from leaf-on and leaf-off airborne Lidar data: A case study in lowland Britain. ISPRS Journal of Photogrammetry and Remote Sensing, 64: 223–233.

Hopkinson, C. and L.E. Chasmer. (2009). Testing LiDAR models of fractional cover across multiple forest ecozones. Remote Sensing of Environment, 113: 275-288.

Hopkinson, C. and L.E. Chasmer. (2007). Modelling Canopy Gap Fraction from LiDAR Intensity. International Archives of Photogrammetry, Remote Sensing and Spatial Information Sciences 36 (Part 3), 190-194.

Hopkinson, C. (2007). The influence of flying altitude, beam divergence, and pulse repetition frequency on laser pulse return intensity and canopy frequency distribution. *Canadian Journal of Remote Sensing, 33*(1-4), 312–324.

Inoue, A., K. Yamamoto, N. Mizoue, and Y. Kawahara. (2004). Calibrating view angle and lens distortion of the Nikon fish-eye converter FC-E8. Journal of Forest Research, 9(2): 177-181.

Jennings S.B., Brown N.D., Sheil D. (1999). Assessing forest canopies and understory illumination: canopy closure, canopy cover and other measures. Forestry, 72(1), 59-74.

Jonckheere, I., K. Nackaerts, B. Muys, P. Coppin. (2005). Assessment of automatic gap fraction estimation of forests from digital hemispherical photography. Agricultural and Forest Meteorology 132: 96-114

Korhonen, L., I. Korpela, J. Heiskanen, M. Maltamo. (2011). Airborne discrete-return LiDAR data in the estimation of vertical canopy cover, angular canopy closure and leaf area index. Remote Sensing of Environment, 115: 1065-1080.

Kucharik, C. J., J.M. Norman, L.M. Murdock, S.T. Gower. (1997). Characterizing canopy non-randomness with a multiband vegetation imager (MVI). Journal of Geophysical Research 102: 29455-29473.

Lang, A.R.G. (1991). Application of some of Cauchy's theorems to estimation of surface areas of leaves, needles and branches of plants, and light transmittance. Agricultural and Forest Meteorology, 55: 191-212.

Lefsky, M. A., W.B. Cohen, S.A. Acker, G.G. Parker, T.A. Spies, D. Harding. (1999). LiDAR remote sensing of the canopy structure and biophysical properties of Douglas-fir Western hemlock forests. Remote Sensing of Environment, 70: 339-361.

Lieffers, V.J., Messier, C., Stadt, K.J., Gendron, F., Comeau, P.G. (1999). Predicting and managing light in the understory of boreal forests. Canadian Journal of Forest Research, 29: 796–811.

McLane, A.J., G. J. McDermid, M. A Wulder. (2009). Processing discrete-return profiling LiDAR data to estimate canopy closure for large-area forest mapping and management. Canadian Journal of Remote Sensing, 35(3): 217-229.

Morsdorf, F., B. Kötz, E. Meier, K. I. Itten, B. Allgöwer. (2006). Estimation of LAI and fractional cover from small footprint airborne laser scanning data based on gap fraction. Remote Sensing of Environment, 104: 50-61.

Naesset, E. (2005). Assessing sensor effects and effects of leaf-off and leaf-on canopy conditions on biophysical stand properties derived from small-footprint airborne laser data. Remote Sensing of Environment, 98: 356-370.

Nasset, E. (2004). Effects of different flying altitudes on biophysical stand properties estimated from canopy height and density measured with a small-footprint airborne scanning laser. Remote Sensing of Environment, 91(2), 243–255.

Pacala S, C. Canham, J. Silander, R. Kobe. (1994). Sapling growth as a function of resources in a north temperate forest. Canadian Journal of Forest Research, 24: 2172–2183.

Orka, H.O., E. Naesset, and O.M. Bollandsas. (2010). Effects of different sensors and leaf-on and leaf-off canopy conditions on echo distributions and individual tree properties derived from airborne laser scanning. Remote Sensing of Environment, 114: 1445-1461.

Riaño, D., F. Valladares, S. Condes, E. Chuvieco. (2004). Estimation of leaf area index and covered ground from airborne laser scanner (LiDAR) in two contrasting forests. Agricultural and Forest Meteorology, 124: 269–275.

Rich, P.M. (1989). A Manual for Analysis of Hemispherical Canopy Photography. Los Alamos National Laboratory. 80p.

Sang, Weiguo; Sha Chen; Guangqi Li. (2008). Dynamic of leaf area index and canopy openness of three forest types in a warm temperate zone. Frontiers of Forestry in China, 6: 416-421.

Smith, M., J. Anderson, M. Fladeland. (2008). Chapter 14: Forest Canopy Structural Properties, in C.M. Hoover, ed., *Media Field Measurements for Carbon Monitoring*, Springer Science + Business Media B.V., p. 179-196.

Tou, J. T. and R. C. Gonzalez. (1974). Pattern Recognition Principles. Reading, Massachusetts: Addison Wesley Publishing Company.

Turner, D.P., S.V. Ollinger, and J.S. Kimball. (2004). Integrating Remote Sensing and Ecosystem Process Models for Landscape- to Regional-Scale Analysis of the Carbon Cycle. BioScience, 54(6): 573-584.

Wasser L, Day R, Chasmer L, Taylor A. (2013). Influence of Vegetation Structure on Lidar-derived Canopy Height and Fractional Cover in Forested Riparian Buffers During Leaf-Off and Leaf-On Conditions. PLoS ONE 8(1): e54776. doi:10.1371/journal.pone.0054776

Weih Jr., R.C., M. Gilbert, J. Cross, and D. Freeman. (2009). Accuracy Assessment of Recreational and Mapping Grade GPS Receivers. Journal of the Arkansas Academy of Science, 63: 163-168.

Wharton, E.H., R.H. Widmann, C.L. Alerich, C.J. Barnett, A.J. Lister, T.W. Lister, D. Smith, and F. Borman. (2004). The Forest of Connecticut. USDA Forest Service. Resource Bulletin NE-160.

White, P.S. (1983). Corner's Rules in Eastern Deciduous Trees: Allometry and Its Implications for the Adaptive Architecture of Trees. Bulletin of the Torrey Botanical Club, 110 (2): 203-212.

Whitemore, T.C., N.D. Brown, M.D. Swaine, D. Kennedy, C.I. Goodwin-Bailey, W.K. Gong. (1993). Use of Hemispherical Photographs in Forest Ecology: Measurement of Gap Size and Radiation Totals in a Bornean Tropical Rain Forest. Journal of Tropical Ecology, 9: 131-151.

Chapter 4:

A fully-automated approach to land cover mapping with airborne LiDAR and high resolution multispectral imagery in a forested suburban landscape

4-1. Abstract

Information on land cover is essential for guiding land management decisions and supporting landscape-level ecological research. In recent years, airborne light detection and ranging (LiDAR) and high resolution aerial imagery have become more readily available in many areas. These data have great potential to enable the generation of land cover at a fine scale and across large areas by leveraging 3-dimensional structure and multispectral information. LiDAR and other high resolution datasets must be processed in relatively small subsets due to their large volumes; however, conventional classification techniques cannot be fully automated and thus are unlikely to be feasible options when processing large high-resolution datasets. In this paper, we propose a fully automated rule-based algorithm to develop a 1-meter resolution land cover classification from LiDAR data and multispectral imagery.

The algorithm we have developed uses a series of pixel- and object-based rules to identify eight vegetated and non-vegetated land cover features (deciduous tall vegetation, coniferous tall vegetation, medium vegetation, low vegetation, water, riparian wetlands, buildings, low impervious cover). The rules leverage both structural and spectral properties including height, LiDAR return characteristics, brightness in visible and near-infrared wavelengths, and normalized difference vegetation index (NDVI). Pixel-based properties were used initially to classify each land cover class while minimizing omission error; a series of

object-based tests were then used to remove errors of commission. These tests used conservative thresholds, based on diverse test areas, to help avoid over-fitting the algorithm to the test areas.

The accuracy assessment of the classification results included a stratified random sample of 3,198 validation points distributed across 30 1x1 km tiles in eastern Connecticut, USA. The sample tiles were selected in a stratified random manner from locations representing the full range of rural to urban landscapes in eastern Connecticut. The overall land cover accuracy was 93% with accuracies exceeding 90% for deciduous trees, low vegetation, water, buildings, and low impervious cover. Slight confusion occurred between coniferous and deciduous trees; major confusion occurred between water and riparian wetlands; and moderate confusion occurred between medium vegetation and other vegetation classes. The algorithm was robust for the forested suburban landscape of eastern Connecticut, which is typical for much of the northeastern U.S., and the algorithm shows promise for applications in similar landscapes with similar datasets. Further research is needed to test the applicability of the algorithm to more diverse landscapes as well as with different LiDAR and multispectral datasets.

4.2. Introduction

Land cover is the physical material on the surface of the earth including features such as water, vegetation, impervious cover, and bare soil. Land cover maps are fundamental to landscape analyses in wide-ranging fields including natural resource management, climate and hydrological modelling, biodiversity conservation, and environmental protection (Yu et al. 2014) as well as urban planning (Angel et al. 2012). Not surprisingly then, land cover mapping has been one of the most extensively studied applications of remote sensing (Yang et al. 2013; Running 2008; Tucker et al. 1985).

Land cover information is derived primarily from data collected by satellite and airborne sensors. Data from the Landsat series of satellites was used in more than 40% of the research papers published on land cover classification (Yu et al. 2014). The sensors on board these satellites collect solar reflectance information for the visible and infrared wavelengths with spatial resolutions of 30 meters. Techniques for extracting land cover information from these moderate-resolution multispectral images have been well-established techniques and include supervised, unsupervised, and object-based methods (Kamusoko and Aniya 2009; Lillesand and Kiefer 2000; Cross et al. 1988).

In recent years, data collected from satellite and airborne sensors with high spatial resolutions has become more widely available. These data include sub-meter resolution multispectral imagery as well as point clouds from active sensors such as light detection and ranging (LiDAR). LiDAR data provide a 3-dimensional view of the features on the earth's surface and have shown excellent promise for deriving high spatial resolution land cover classifications when used alone (Antonarakis et al. 2008; Im et al. 2008; Miliaresis and Kokkas 2007; Brennan and Webster 2006) or in conjunction with multispectral data (Arroyo et al. 2010; Koetz et al. 2008; Syed et al. 2005; Charaniya et al. 2004; Hodgson et al. 1999).

The majority of research on methods for classifying land cover from airborne LiDAR has used object-based approaches in which the study area is divided into object segments with homogenous properties (see Arroyo et al. 2010; Antonarakis et al. 2008; Im et al. 2008; Brennan and Webster 2006). A rule set is then developed which assigns the objects to particular land cover classes based on its spectral and spatial characteristics. Some studies have tested pixel-based supervised classification approaches in which training areas are used to identify the properties of pixels belonging to each land cover class (Koetz et al. 2008; Syed et al. 2005;

Charaniya et al. 2004; Hodgson et al. 1999). A maximum-likelihood or non-parametric algorithm is then used to assign all pixels to the class corresponding to the training area which has the most similar properties. Hodgson et al. (1999) also tested an unsupervised pixel-based method to classify impervious cover and compared the results to classifications made with supervised pixel-based and object-oriented methods. The unsupervised method used the iteratively self-organized data (ISODATA) algorithm to assign pixels into groups with homogenous properties; the groups are then manually assigned to the appropriate land cover class. Hodgson et al. (1999) found the object-based method yielded higher accuracies than either the supervised or unsupervised pixel-based methods. Studies that have used object-based methods generally report classification accuracies exceeding 90% (see Antonarakis et al. 2008; Im et al. 2008; Brennan and Webster 2006) whereas studies that used pixel-based methods report overall accuracies less than 85% (Koetz et al. 2008; Charaniya et al. 2004).

All previous studies that we have found reported in the literature used relatively small sample areas, often less than several square kilometers, to test methods of deriving land cover classifications from airborne LiDAR data and the ability of these methods to be applied efficiently over large areas has not yet been demonstrated. The object- and pixel-based methods described in the literature each require some degree of human interpretation. Object-based methods require the user to specify the parameters used to segment study area into objects as well as develop a rule set with which to classify the objects. Supervised pixel-based methods require training data to be provided which are unlikely to be applicable across large areas because of the variability in both the landscape and in spectral data. Unsupervised pixel-based methods require human interpretation to identify the land cover class to which each pixel group is assigned (Lillesand and Kiefer 2000). Thus, a fully automated approach to classifying land

cover has not yet been achieved. The requirement for human decision-making in the classification process becomes problematic as the extent of the classification area increases. The very large sizes of high resolution LiDAR and multispectral datasets limit the areal extent over which these data can be processed in a single iteration. High resolution datasets may need to be divided into hundreds or thousands of subsets to allow for efficient processing. Thus, even with semi-automated methods it is impractical to derive land cover from high-resolution data for areas spanning hundreds or thousands of square kilometers.

The primary objective of this research is to develop a fully-automated algorithm to derive land cover from high resolution airborne LiDAR and aerial orthophotographs that can be applied over a relatively large spatial area (e.g. eastern Connecticut). We aim to make the algorithm robust to the landscape heterogeneity found in eastern Connecticut which is likely similar to landscapes throughout the northeastern, USA. The algorithm will create a 1-meter resolution land cover classification depicting: 1) deciduous trees, 2) coniferous trees, 3) medium-height vegetation, 4) low vegetation, 5) water, 6) riparian wetlands, 7) buildings, and 8) low impervious cover (i.e. roads, parking lots). We propose to use a combination of pixel- and object-based rules to extract land cover information based on feature structural and spectral properties. We suspect that the combination of LiDAR and multispectral imagery will be sufficient to achieve an acceptable level of accuracy and robustness to the range of landscapes found in Connecticut.

4-3. Methods

The study area for this research was located in eastern Connecticut, located in the northeastern United States (Figure 4-1). The landscape is dominated by temperate deciduous and mixed forests with the built-up landscape ranging from urban to rural. Topography can be

characterized as hilly with elevations ranging from sea level in the south to 330 meters in the north.

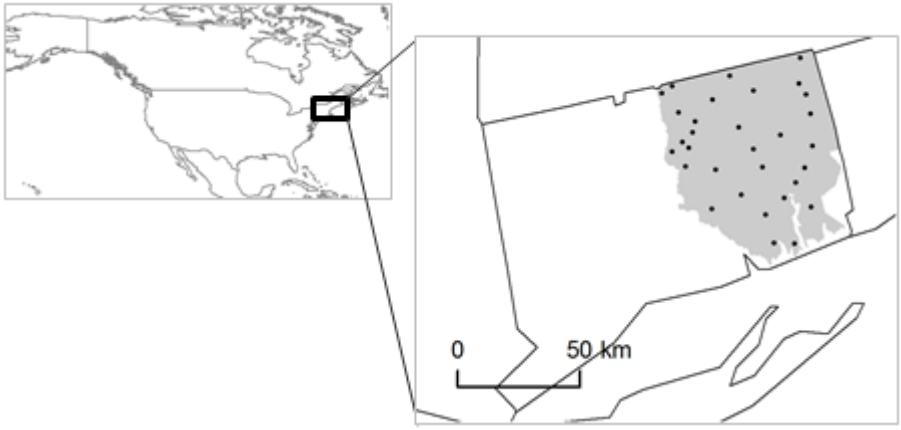

Figure 4-1: The study area consisted of 30 1x1 km tiles (black dots) distributed semi-randomly throughout eastern Connecticut, USA. The gray area shows the extent of the LiDAR dataset.

4-3.1. Data description and processing

All data layers derived from the LiDAR and multispectral orthophotos had a 1 meter spatial resolution and were aligned to the same reference grid. The LiDAR intensity imagery and the orthophotos were resampled to 1 meter using bilinear interpolation. All data processing was performed using scripts written in Python 2.7 with ArcGIS 10.2.

4-3.1.1. LiDAR

The LiDAR data used in this research were acquired for nearly 4600 km^2 in eastern Connecticut during leaf-off conditions from November 3 – December 11, 2010 (Dewberry 2011). The data were collected with a Leica ALS60 Airborne Laser Scanner[16] at an altitude of approximately 2000 meters above ground level. At this altitude, the ALS60's beam divergence of 0.22 millirads creates a footprint of roughly 44 cm on the ground. The scanner emitted a pulse

[16] see http://www.leica-geosystems.com/en/Leica-ALS60-Airborne-Laser-Scanner_57629.htm

wavelength of 1.064 µm at a rate of 117.9 kHz. The flight line overlap was 50% and the data provider eliminated data with gaps between the geometrically usable portions of the swaths. The maximum scan angle of the sensor was 16.5^0 from nadir and it recorded up to 4 returns per laser pulse. Returns were classified as ground, noise, water, or unclassified and the intensity of each return was recorded. The dataset has an overall density of 1.56 returns / m^2 with a maximum point spacing of 0.7 meters in areas without water bodies. The project's principle contractor processed the LiDAR data to create a bare-earth digital elevation model (DEM), at a 1-meter resolution, with building features removed. Dewberry (2011) evaluated the accuracy of the DEM using 62 surveyed ground control points distributed through unvegetated, grass, and forested terrains. The vertical RMSE for the DEM, based on the ground control points, was estimated at 5 cm in non-vegetated terrain, 17 cm for grassy terrain, and 21 cm in forest terrain. Dewberry (2011) also developed images showing the intensities of the returns with a spatial resolution of 0.3 meters. The primary purpose of the LiDAR dataset was to develop the bare-earth DEM for use in conservation planning, floodplain mapping, dam safety assessments, and hydrological modeling (Dewberry 2011).

The characteristics of a LiDAR return can provide important clues as to the feature that generated the return. Single-returns are generated when a pulse is reflected from a solid surface whereas multiple-returns are generated when a pulse filters through a porous medium such as a tree canopy. Ground returns are reflected from the bare-earth surface; we consider any return that is within 20 cm of the bare-earth DEM elevation to be a ground return[17]. We created a return type classification raster in which grid cells were assigned the following values based on the characteristics of LiDAR returns present in the cell: 0) other, 1) non-ground single returns only,

[17] 20 cm is the approximate RMSE value for Dewberry's DEM in forested areas.

2) multiple-returns with no ground returns, 3) multiple returns with ground returns, and 4) no returns or water returns (as classified by the data provider). Cells with non-ground single-returns (value = 1) can be indicative of buildings, evergreen trees, dense deciduous vegetation, or vegetation overhanging water. Cells with multiple returns but no ground returns (value =2) can indicate a solid structure beneath a tree canopy, water beneath a tree canopy, or simply a pulse that had insufficient energy to penetrate to the ground. Multiple-returns with ground returns (value = 3) most likely indicate a deciduous tree canopy. Cells with no returns or classified as water returns (value = 4) can indicate water or other features that are poor reflectors of near-infrared energy.

A maximum height model (H_{max}) can help to distinguish between trees, shrubs, and low vegetation. We derived H_{max} using the procedures described in Parent and Volin (2014). The height model was the difference in elevations between the bare-earth DEM, created by Dewberry (2011), and a maximum elevation digital surface model (DSM) that we created from the LiDAR data. The DSM was aligned to the DEM and had the same 1-meter resolution. We determined the cell values for the DSM grid by taking the maximum of all non-ground first-return points within a given cell. We filtered the first-return data to remove points that obviously did not correspond to features on the earth's surface (e.g. large birds in flight). These anomalous points were identified by comparing each first-return to all points within a 2.5 meter radius. Points were discarded if they were more than 30 meters taller than any other points within the neighborhood. We selected the 30 meter threshold because it approximates the upper limit of canopy heights in northeastern forests and thus it represented a reasonable maximum elevation difference for points along forest gaps and edges. A test of 52 1x1 km sample areas showed that an average of 12.9% (std. dev. = 3.4) of cells did not contain any first-return data. Continuous data gaps larger than 3

meters in radius are likely too large to have been missed by the laser scanner, thus we assumed that these gaps were due to water which tends to absorb near-infrared energy. We assigned the bare-earth DEM values to the cells that corresponded to the presumed water bodies. For the remaining non-water data gaps, the fractions of the small gap area with radii of ≤1, 1-2, and 2-3 meters were on average 0.91, 0.07, and 0.01, respectively. The values for cells in the DSM data gaps, smaller than 3 meters in radius, were interpolated by taking the median of the known values in the cells' eight nearest neighbors. Cells with fewer than three known nearest neighbors were filled using a 2^{nd} or 3^{rd} interpolation pass.

A minimum elevation height model (H_{min}) helps classify buildings that may be overtopped by the forest canopy and thus are not fully visible in the H_{max} model. The cells of the H_{min} raster were calculated by subtracting the cell's DEM elevation from the elevation of the lowest return in the cell. All returns, including ground, were considered in the selection of cell values. The very small percentage of grid cells that did not contain any returns were interpolated by taking the median value of the eight nearest neighbors using the same procedure as described above for the H_{max} raster.

LiDAR returns generated from solid surfaces tend to have little vertical variation when compared to shrub or tree canopies (Figure 4-2). We developed the vertical point density (VPD) metric to quantify this characteristic and used it to help distinguish buildings from vegetation. The VPD is calculated for each grid cell based on its 3x3 neighborhood. For each cell in the neighborhood, we extracted the returns that are less than 3 meters above H_{min} and assumed that they corresponded the surface of the lowest elevation feature. The upper limit of 3 meters was used to exclude returns generated by branches that may be overtopping a building. A second lower threshold above H_{min} was set, based on the slope of the H_{min} surface, and returns below the

threshold were considered to have potential to correspond to a solid surface. Assuming that a given cell contains a solid feature, the expected range of return elevations within the cell will increase as the slope increases. For example, a grid cell corresponding to a roof with a 45^0 slope would potentially have returns with elevation differences as large as 1 meter. Thus, we set the lower threshold for a given neighborhood based on the slope of the center grid cell; thresholds of 0.5, 0.75, and 1.0 meters above H_{min} were used for slopes < 15^0, 15-30^0, and >30^0, respectively. VPD for a given grid cell was calculated as:

$$VPD = \frac{number\ of\ returns\ in\ neighborhood\ with\ heights < lower\ threshold}{number\ of\ returns\ in\ neighborhood\ with\ heights < 3\ meters\ above\ Hmin} \quad (1)$$

Grid cells in a 3x3 neighborhood were excluded from the calculation if H_{min} was less than 2 meters. To help ensure VPD values are based on adequate sample of points, the metric was not calculated for a grid cell if more than 3 cells in its neighborhood had been excluded. Data gaps in the VPD raster were left as null values. High VPD values are indicative of roof tops and other solid surfaces whereas lower values indicate porous surfaces (i.e. vegetation).

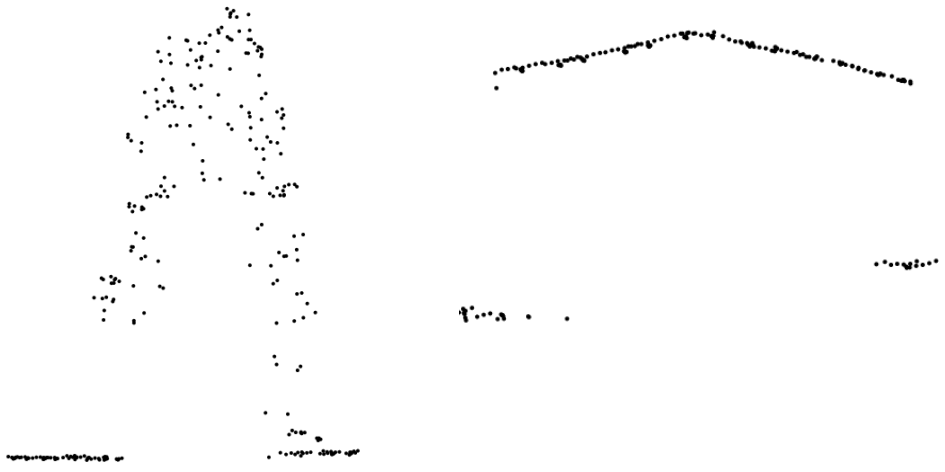

Figure 4-2: LiDAR point clouds for profile views of a coniferous tree (left) and a house (right). Vertical Point Density (VPD) values for the tree and house are 0.36 and 0.98, respectively.

Roads are often overtopped by the forest canopy which can complicate the detection of roads in forest areas. However, roads can be characterized by an absence of LiDAR returns below a height of several meters because vegetation would be excluded from this zone to allow adequate clearance for vehicles. This lack of returns should contrast with roadside forests which typically have ample returns generated from understory vegetation. Based on our observations, we assume that road features will have no LiDAR returns between 2 and 4.5 meters above the ground because this zone should be nearly free of vegetation and vehicles. We created the understory return count (URC) raster which is a count of LiDAR returns having heights from 2 to 4.5 meters within a 3x3 neighborhood around each grid cell.

4-3.1.2. Aerial orthophotographs

The aerial orthophotographs, available for the study area, had a spatial resolution of 0.3 meters with a 1.5 meter horizontal accuracy (USGS 2012). The imagery was acquired with Intergraph's Z/I Digital Mapping Camera system[18] which records reflectance in the blue, green, red, and near-infrared (NIR) bands with brightness values ranging from 0-255. The imagery was acquired, for the entire state, from March 18-30, 2012 before the bud-break or leaf-out of deciduous trees. We used the orthophotos to create 4 raster layers indicating: 1) normalized difference vegetation index (NDVI), 2) bright grid cells, 3) dark grid cells, and 4) moderately dark grid cells. NDVI is useful for distinguishing between vegetated and non-vegetated surfaces because photosynthetic elements (e.g. leaves) are adapted to reflecting near-infrared energy in order to reduce heat build-up (Campbell and Wynne 2011). NDVI is calculated as (Tucker 1979):

[18] See http://www.geospace.co.za/pdf/DMC%20Brochure.pdf

$$NDVI = \frac{(red - NIR)}{(red + NIR)} \quad (2)$$

In the leaf-off orthophotos, high NDVI corresponds to coniferous trees and grass which contain photosynthetic elements at the image acquisition time. Deciduous trees are leafless and thus have moderate NDVI values. We considered *bright cells* to have reflectance values greater than 150 in all visible and NIR bands and these cells indicate highly reflective surfaces that tend to be impervious cover such as concrete. *Dark cells*, with brightness < 75 in all bands, can indicate shadows whereas *moderately dark* cells, with brightness <100 in all bands, can indicate wetland areas. The thresholds used to define bright, dark, and moderately dark cells were determined based on our observations for the test areas.

4-3.2. Land cover classification

The classification developed in this study included eight land cover classes at 1m resolution: 1) deciduous trees, 2) coniferous trees, 3) medium vegetation, 4) low vegetation, 5) water, 6) riparian wetland, 7) buildings, and 8) low impervious cover. The classification algorithm used thresholds that we determined based on experimental observations using several test areas containing a diversity of landscapes. The general strategy of the algorithm was to use pixel-based characteristics to initially classify each land cover type with a minimum of omission errors. Smoothing operations, such as a majority filter, were then used to eliminate insubstantial objects. Finally, a series of object-based tests were used to remove commission errors from the classification. These tests were designed to be conservative and remove only relatively extreme error cases in order to avoid over-fitting the algorithm to the test areas.

4-3.2.1. Water classification

Water typically absorbs electromagnetic energy with the near-infrared wavelengths used by airborne LiDAR sensors in terrestrial applications (Campbell and Wynne 2011). Thus, in a LiDAR dataset, the absence of any returns over a significant area is typically an indicator of a water body. Some features associated with anthropogenic structures (e.g. sky lights and certain roof materials) may also cause an absence of LiDAR returns. Returns generated from areas containing water are likely the result of vegetation growing in or on the water. For the data used in this research, the data provider detected some of the returns associated with water bodies and classified them accordingly. In our initial classification of water, we considered *potential open water* to be grid cells that have H_{max} values less than 5 cm (the DEM RMSE for non-vegetated terrain) and contain either 1) no returns or 2) at least one return that the data provider classified as water. The height threshold excluded features with non-zero heights that did not generate any LiDAR returns. *Potential open water* cells were filtered to extract contiguous groups of cells that 1) had a center at least 1 meter from the edge of the group, and 2) covered an area of more than 50 m^2. We considered the selected groups to be *open water* and we used them as seeds to expand the water classification into neighboring grid cells that were also likely to be water.

Trees that overhang the shores of rivers and water bodies can obscure the water edge and cause these areas to have properties not characteristic of water. Areas in which water is overtopped by trees tend to contain LiDAR returns but have no ground returns because pulse energy that reaches the surface is absorbed by the water. Buildings are also characterized by an absence of ground returns but the VPD metric can help distinguish buildings from a tree canopy over water. To include forested water edges in the water classification more accurately, we grew contiguous groups in the *open water* layer to encompass neighboring *potential water* cells which

had 1) no ground returns, 2) NDVI < 0.15, and 3) VPD < 0.75 [19]. The growth of the *open water* groups was accomplished using a cost-distance operation which weights Euclidean distance measurements by a cost raster. In this case, the cost raster values were zero for *potential water* grid cells, and remaining cells had an impassable cost to prevent expansion from occurring into these cells. To remove spurious water cells, the *semi-final water* layer was smoothed with a majority filter[20] in a focal statistics operation using a circular neighborhood 4 meters in radius.

Narrow rivers tended to be lost from the *semi-final water* layer as a result of the smoothing operation. To help enhance the connectivity of rivers, we used an iterative series of least-cost path (LCP) analyses. A LCP analysis uses cost-weighted Euclidean distances to identify the least cost path between a source location and one or more destinations. These analyses were used to connect water groups in the *semi-final water* layer; the centers of each group were used, in turn, as the source point while the other centers served as destination points. Destination points were excluded if their elevations were higher than the source point. In the cost raster for the LCP analyses, *potential water* cells were assigned low costs which did not add significantly to the overall path costs. These costs were weighted such that cells closer to the exterior of a group had slightly higher costs than more interior cells which ensured that paths would avoid following the edges of *potential water* groups. Cells not considered *potential water* were assigned a high cost such that a path could contain at most 9 of these cells before exceeding its maximum allowed cost. The cost raster was modified, based on the source point of the current LCP iteration, such that cells were assigned impassable costs if they contained a destination point or had a DEM elevation higher than the source point's DEM elevation. Excluding these

[19] The VPD threshold of 0.75 was determined from observational experiments within the test area. Values above 0.75 tended to correspond to buildings whereas lower values were most likely to correspond to vegetation.
[20] The majority filter assigns the most frequently occurring value in the neighborhood to a given grid cell.

cells ensured that paths could not go uphill from the source point. Least cost paths were delineated between each source point and all of its destination points; paths that exceeded the maximum allowed cost were discarded. The remaining viable paths were buffered by 20 meters and used to extract *potential water* cells that fell within the buffers. Contiguous groups of the extracted *potential water* cells that intersected the path line were included in the *final water* layer. Two meter buffers around the paths were also included in the *semi-final water* layer to help ensure that narrow stream channels would be preserved. The *final water* layer was smoothed using focal statistics with a majority filter and a circular neighborhood with a 4 meter radius. Table 4-1 summarizes the rule set for classifying water.

Table 4-1: Classification rule set for water.

1) Extract *potential open water*: cells with H_{max} < 5 cm and with either no returns or a water return

2) Extract *open water*: *potential open water* groups with area > 50 m^2 and group center > 1 m from edge.

3) *Semi-final water*: created by expanding *open water* into neighboring *potential water* cells.

   a. *potential water:* cells with 1) no ground returns, 2) VPD < 0.75, and 3) NDVI < 0.15

4) *Final water* layer: created using least-cost path (LCP) analyses to connect *semi-final water* groups. Final layer includes 1) *potential water* groups that intersected a viable path, 2) a 2 m buffer around viable paths, and 3) *semi-final water*.

   a. For each LCP iteration, center of each *semi-final water* group is used, in turn, as source point; all other centers used as destination points. Destination points with DEM elevations lower than source point elevation are excluded.

   b. *Viable paths:* formed by *potential water* cells; may include up to 9 cells not considered *potential water*; cannot include cells with DEM elevations higher than source point DEM elevation.

4-3.2.2. Building classification

In our classification, we define buildings to be anthropogenic impervious structures with heights greater than 2.5 meters. A number of characteristics may be used to help identify buildings based on LiDAR data and orthophotos; however, many of these characteristics are shared by tall vegetation under certain conditions. LiDAR returns that intercept buildings are typically classified as non-ground returns, by the data provider, because they do not correspond to the bare-earth surface (Dewberry 2011). Forested water edges also tend to be characterized by the presence of LiDAR returns but with an absence of ground returns. The solid surfaces of buildings tend to generate single-returns except when overtopped by a deciduous tree canopy or when a laser pulse partially intercepts a roof edge. Coniferous trees also frequently generate single-returns because of their dense canopies. Buildings that are overtopped by trees may be expected to have limited heights and contain at most 2 or 3 floors, thus a maximum height threshold can help reduce commission errors with vegetation. Non-vegetated surfaces typically have very low NDVI, however, buildings overtopped by leaf-off deciduous trees may have NDVI values slightly higher than expected. Buildings typically occur on relatively level ground and thus DEM slope can reduce confusion with vegetation on slopes. Based on observations and experiments, we initially classify *potential building* grid cells based on the following attributes: 1) no ground returns; 2) not classified as water; 3) NDVI < 0.15; 4) height > 2.5 meters; 5) if multiple-returns then height < 8 meters; and 6) ground slope < 20^0.

The *potential building* classification was intended to err on the side of commissions; a series of object-based tests was used to reduce these errors. *Potential building* grid cells were first grouped into contiguous objects and the holes in these objects were filled. Objects were eliminated if the object center was less than 1 meter from the nearest edge or if the object had an area less than 15 m^2. Actual building objects should have relatively high VPD values because

they are solid structures; thus we eliminated objects with VPD values < 0.75. Buildings with small footprints are not likely to have more than 2-3 floors; therefore, we eliminated objects with average heights > 10 meters if the object had an area of < 50 m^2. Small objects that were adjacent to water tended to be misclassifications resulting from trees overhanging water; however, larger objects tended to be industrial buildings. Thus, we eliminated objects if they were adjacent to water and had an area < 50 m^2. Finally, we excluded objects if more than 2/3 of its area consisted of dark grid cells which we assumed to be shadows. This final test served to reduce possible commission errors caused by evergreen tree shadows that are cast onto lower vegetation. The final selection of building objects was smoothed by two iterations of expanding and then shrinking the objects by 1 meter. We found this smoothing approach to help prevent artificial rounding of the building objects. Table 4-2 summarizes the rule set for classifying buildings.

Table 4-2: Classification rule set for buildings.

1) Extract *potential buildings*: cells that 1) have no ground returns; 2) not classified as water; 3) NDVI < 0.15; 4) height > 2.5 m; 5) if multiple-returns, then height < 8 m; 6) DEM slope < 20^0.

2) Create *final building* layer using object-based tests to remove commission errors:
   a. Group *potential buildings* and fill holes.
   b. Remove groups with area < 15 m^2 or with centers < 1 m from the exterior.
   c. Remove groups adjacent to the *final water* layer with area < 50 m^2.
   d. Remove groups with VPD < 0.75.
   e. Remove groups with average heights > 10 m if area < 50 m^2.
   f. Remove groups for which more than 2/3 of the area is dark cells (i.e. shadow).

4-3.2.3. Low vegetation classification

The low vegetation class consisted of turf and natural grasses with heights less than approximately 1.5 meters. Low vegetation can be characterized by LiDAR returns with a high intensity because all pulse energy tends to be reflected in a single return and green vegetation has high reflectivity in the NIR band (Jensen 2007). Some non-vegetated features (e.g. vehicles) can generate returns with high intensities; thus, we also used NDVI to identify low vegetation. *Potential low vegetation* grid cells were classified based on the following: 1) LiDAR return intensity > 150 and NDVI > 0.1; or 2) LiDAR return intensity > 150 and is a dark cell (i.e. shadow). We assumed that shadows corresponded to low vegetation if the LiDAR return intensity was high. Based on our observations, vehicles are the most common non-vegetated features that can generate high return intensities. Thus, based on the prevalence of low vegetation, we assumed that the error from omitting actual low vegetation was likely to be greater than the error from incorrectly labelling vehicles as low vegetation. To help further reduce commissions of vehicles, contiguous groups of *potential low vegetation* cells were only included in the *final low vegetation* classification if they had an average $H_{max} < 1.5$ meters for either 1) the entire group or 2) the group excluding the cells forming the perimeter. These tests should eliminate most vehicle objects which typically have heights greater than 1.5 meters. The second test accounts for groups adjacent to forest land cover which may include tree cells along the edges that can inflate the average heights and cause these groups to be rejected. Shrinking the groups by one meter helps ensure that tree cells are not included in the average height. Although seemingly redundant, the first test was still needed to test patches of *potential low vegetation* that are less than or equal to 1 meter deep. Table 4-3 summarizes the rule set for classifying low vegetation.

Table 4-3: Classification rule set for low vegetation.

1) *Potential low vegetation*: cells with either: 1) intensity > 150 and NDVI > 0.1, or 2) intensity > 150 and is a dark cell.

2) *Final low vegetation*: contiguous groups of *potential low vegetation* for which average H_{max} < 1.5 for either: 1) the entire group, or 2) the group excluding the cells forming the outer perimeter.

4-3.2.4. Classification of wetlands adjacent to water

Wetlands were discernible in the spring-time leaf-off orthophotos as areas with relatively low reflectance in the visible and near-infrared wavelengths. In this study, we focused only on classifying wetlands that were adjacent to water bodies. We considered *potential wetlands* to be moderately dark cells that were not already classified as low vegetation. *Potential wetlands* cells were filtered by removing cells for which fewer than 2 out of 4 nearest neighbors where classified as *potential wetland*. This filtering served to eliminate error by removing cells that were isolated or weakly connected to each other. Groups of *potential wetland* cells that were adjacent to previously classified *final water* groups were extracted and considered to be the *final wetland* layer. These *final wetland* groups were identified using a cost-distance operation in which the cost raster assigned a cost of zero to *potential wetland* cells and an impassable cost to all other cells. Table 4-4 summarizes the rule set for classifying wetlands.

Table 4-4: Classification rule set for wetlands.

1) *Potential wetland*: cells that were moderately dark and not classified as low vegetation. Cells were excluded if fewer than 2 out of 4 nearest neighbors were *potential wetland*.

2) *Final wetland*: groups of *potential wetland* cells adjacent to *final water* cells.

4-3.2.5. Classification of low impervious cover

The low impervious cover (LIC) class included roads, parking lots, and other impervious surfaces that were not considered buildings. We attempted to classify LIC that is overtopped by forest canopies and thus our classification required the use of a number of LIC characteristics to reduce commission errors. LIC can typically be characterized by the presence of ground returns and low NDVI; however, vehicles may cause isolated occurrences of LIC with no ground returns and NDVI may be higher than expected for LIC overtopped by vegetation. Some concrete surfaces (e.g. sidewalks) may have very high reflectance in visible and NIR wavelengths. Low impervious cover should have no LiDAR returns in the zone between 2 and 4.5 meters; vehicles and low branches may cause returns below and above this zone, respectively. We established the following criteria for *potential LIC* cells: 1) not previously classified as water, low vegetation, or wetland; 2) NDVI < 0.075 if multiple returns are not present (i.e. no tall deciduous vegetation) or NDVI < 0.15 if multiple returns are present; 3) contains ground returns or if H_{max} < 2 meters, then ground returns may be absent; 4) no dark cells; and 5) no returns between 2 and 4.5 meters above the ground (URC = 0). Bright grid cells were considered *potential LIC* in addition to the cells meeting the previous criteria. Isolated or semi-isolated *potential LIC* cells were filtered out by eliminating cells for which fewer than 2 out of 4 nearest neighbors were considered *potential LIC*.

The *potential LIC layer* contained a large amount of commission errors which we attempted to reduce through a series of object-based tests. Contiguous groups of *potential LIC* were eliminated if they had 1) fewer 100 cells or 2) failed the *object solidity test*. The *solidity* test consisted of calculating, for each LIC cell, the fraction of the eight nearest neighbors that were considered *potential LIC*. A group failed the test if the average fraction of potential LIC neighbors was < 0.75. We found that intermediate-sized LIC groups, with areas from 100 to 500

m^2, tended to correspond to road segments but had high levels of commission error. Road segments should have linear shapes, thus we analyzed these groups using the normalized proximity and range indices (Angel et al. 2010)[21]. Values for both indices range from 0 to 1 with high values indicating compact shapes and lower values indicating elongated shapes. Based on experimental observations, we eliminated *potential LIC* groups if 1) the normalized proximity index was > 0.75 or 2) the normalized range index was > 0.5.

The size, solidity, and shape tests erred on the side of commissions to prevent the elimination of valid groups from the *potential LIC* layer. *Likely LIC* groups were identified using a second series of more restrictive object-based tests intended to minimize commission errors at the expense of omitting valid groups. To help recover the actual LIC cells that were omitted, we identified *potential LIC* groups that were semi-contiguous with the *likely LIC* cells and included these groups in the *semi-final LIC* layer. The *likely LIC* cells were defined as *potential LIC* groups that had 1) a mean NDVI < 0.1 or 2) a strongly linear shape with normalized range index values of < 0.3. We identified *potential LIC* groups that were semi-contiguous with *likely LIC* cells by using a cost-distance analysis. The cost raster for the analysis assigned: 1) a cost of zero to *potential LIC* cells, 2) an impassable cost to non-ground single-returns with heights > 2 meters, and 3) a cost of 1 to all other cells (i.e. unlikely LIC). The maximum cost in the analysis was set to allow up to 4 unlikely LIC cells to be used in traversing gaps between *likely LIC* and *potential LIC* cells. Expansion was not permitted to occur through cells with non-ground single-returns taller than 2 meters because they were likely to correspond to a feature not associated with LIC (e.g. coniferous canopy). The resulting *semi-final LIC* layer was smoothed by using focal statistics with a circular neighborhood with a 3 meter radius. Cells were eliminated if less

[21] Metrics were calculated using the Shape Metrics Tool http://www.clear.uconn.edu/tools/index.htm

than 75% of their neighborhood did not consist of *semi-final LIC*. We found this smoothing technique to fill in gaps in the LIC layer while minimizing the buffering effect that tends to be created when smoothing is done with a majority filter.

The *semi-final LIC layer* tended to omit roads that were in shadows or overtopped by coniferous trees and in general lacked the road connectivity that we intended to achieve. Thus, we performed a least-cost path analysis to connect *semi-final LIC* segments that could be bridged using *potential LIC* cells and selected segments from Tele Atlas's 2003 streets dataset[22]. The accuracy of the Tele Atlas dataset was quite variable and often contained roads that either do not currently exist or have considerable offset from their true locations. Therefore, we first used the *potential LIC* layer to help identify streets in the network that seemed to correspond to actual road locations. The streets vectors were buffered by 0.5 meters; features were considered to be valid street segments if more than 75% of their buffer was comprised of *potential LIC* cells. Valid street segments were buffered by 3 meters and merged with the *semi-final LIC* layer, to create the *core LIC* layer, as well as appended to the *potential LIC* layer. The centroid of each *core LIC* group was used as the source and destination locations for the LCP analyses; each centroid was iteratively used as the source point and the remaining centroids were used as destination points. A cost raster was created which assigned a range of very low values to *potential LIC* cells and a very high value to all other cells. The *potential LIC* cells were weighted such that paths would avoid following the outside edges of groups of cells; however, the weights had no significant effect on the overall path costs. A cost-distance analysis was used to calculate the cost from the current source point to each of the destination points. The LCP analysis was then used to identify viable paths that joined a given source point to its destination points. A path

[22] The dataset was enhanced by ESRI and provided with the ESRI Data & Maps

was considered viable if it contained a maximum of 30 cells that were not classified as *potential LIC*. The *final LIC* layer contained: 1) *core LIC* groups, 2) *potential LIC* groups that intersected a viable path, and 3) a 4 meter buffer around viable paths. The *final LIC* layer was smoothed using focal statistics with a majority filter and a circular neighborhood with a 4 meter radius. Table 4-5 summarizes the rule set for classifying LIC.

Table 4-5: Classification rule set for low impervious cover (LIC).

1) Identify *potential LIC* cells:
   a. *Potential LIC*: cells that were either bright or met each of the following criteria:
      i. not previously classified as water, low vegetation, or wetland
      ii. NDVI < 0.075 if multiple returns are not present (i.e. no tall deciduous vegetation) or NDVI < 0.15 if multiple returns are present
      iii. contains ground returns or if H_{max} < 2 meters, then ground returns may be absent
      iv. no dark cells
      v. no returns between 2 and 4.5 meters above the ground (URC = 0)
   b. *Potential LIC* filtered to remove isolated or semi-isolated cells – cells with fewer than 2 out of 4 nearest neighbors considered *potential LIC*
   c. Groups eliminated from *potential LIC* if:
      i. area < 100 m^2
      ii. failed solidity test (on average fewer than 75% of 8 nearest neighbors were *potential LIC*)
      iii. area 100-500 m^2 and failed shape test (proximity > 0.75 or range > 0.5)
2) Create *semi-final LIC* layer: consists of *likely LIC* cells and semi-contiguous *potential LIC* cells. *Potential LIC* groups included if within 4 meters of a *likely LIC* cell.
   a. *Likely LIC*: potential LIC groups (step 3) with either 1) NDVI < 0.1 or 2) range index < 0.3
   b. Cost-distance analysis to expand *likely LIC* into semi-contiguous *potential LIC*.
3) Create *final LIC* layer: least-cost path analysis used to connect *semi-final LIC* cells with

potential LIC and Tele Atlas street data.

a. Eliminate invalid Tele Atlas streets (<75% of street segment length overlays *potential LIC* cells).

b. Buffer valid streets by 3 meters and append to *potential LIC* as well as merge with *semi-final LIC* (i.e. *core LIC*)

c. Iterative least-cost path analyses use each centroid of *core LIC* groups as a source point and other centroids as destination points. *Potential LIC* used to connect source points to destinations – paths avoid perimeters of potential LIC groups; viable path may include a maximum of 30 cells that are not *potential LIC*

d. *Final LIC* consists of 1) core LIC groups, 2) potential LIC groups that intersect a viable path, and 3) a 4 meter buffer around viable paths.

4-3.2.6. Classification of medium and tall vegetation

Vegetation is characterized mainly by a relatively high NDVI, even for deciduous vegetation during the early spring time leaf-off conditions during which the orthophotos were acquired. For our data, we found than NDVI > 0.15 corresponds well to vegetation with evergreen trees having a higher NDVI than deciduous trees during these leaf-off conditions. We consider vegetation taller than 3 meters to be trees and lower vegetation to be shrubs or tree saplings. Specifically, we classify medium vegetation as grid cells that 1) have H_{max} between 0.5 and 3 meters and 2) have NDVI values > 0.15. We smoothed the medium vegetation layer using focal statistics with a circular 4m radius neighborhood and a majority filter.

We selected the NDVI threshold to err on the side of omitting actual vegetation in order to reduce the occurrence of buildings misclassified as trees when they are overtopped by deciduous vegetation. Thus, NDVI and height alone were insufficient to obtain a good classification for trees. We initially classified grid cells as *potential trees* if 1) H_{max} was greater than 3 meters, 2) they contain multiple-returns or non-ground single-returns, and 3) they are not within 3 meters of a classified building cell. Cells near building edges are excluded initially

because they tend to contain multiple-returns caused by the laser footprint partially intercepting a roof top rather than the result of vegetation. *Potential tree* cells that have NDVI > 0.15 are considered *likely tree* cells. Cost-distance analysis was used to grow likely tree cells into contiguous and adjacent potential tree cells. The cost raster for the analysis considered *potential tree* cells to have zero cost while all other cells had an impassable cost. The resulting *tall vegetation* classification included both deciduous and coniferous trees.

Coniferous tall vegetation was sub-classified from the *tall vegetation* layer (Table 4-6). *Potential coniferous* cells consisted of *tall vegetation* cells with NDVI > 0.25 and contained only non-ground returns. Similarly, *likely coniferous* grid cells were tall vegetation cells with NDVI > 0.3 and contained only non-ground returns; contiguous groups of remaining cells were excluded if the area was less than 10 m^2. The *final coniferous* classification was created using a cost-distance analysis to grow the *likely coniferous* cells into adjacent contiguous groups of *potential coniferous* cells. *Deciduous* cells consisted of *tall vegetation* cells that were not classified as coniferous cells. Table 4-6 summarizes the rule set for classifying medium and tall vegetation.

Table 4-6: Classification rule set for vegetation.

1) *Medium height vegetation*: cells with NDVI > 0.15 and H_{max} between 0.5 and 3 meters.

2) *Tall vegetation*: *likely tree* cells and adjacent contiguous groups of *potential tree* cells.

   a. *Potential trees*: cells with 1) H_{max} > 3 meters, 2) multiple returns or non-ground single-returns, and 3) not within 3 meters of a *final building* cell.

   b. *Likely trees*: *potential tree* cells with NDVI > 0.15

3) *Coniferous vegetation*: *likely coniferous* cells and adjacent contiguous groups of *potential coniferous* cells.

   a. *Potential coniferous*: tall vegetation with NDVI > 0.25 and contains only non-ground returns.

b. *Likely coniferous*: tall vegetation with NDVI > 0.3 and contains only non-ground returns. Contiguous groups removed if area < 10 m^2.

4) *Deciduous vegetation*: *tall vegetation* cells not classified as *coniferous vegetation*.

4-3.2.7. Combining land covers into a single classification

Grid cells had the potential to receive conflicting designations from the eight individual land cover classifications due to overlapping feature characteristics and smoothing of the classifications. The final class layers were given the following priority in creating the final land cover classification: 1) water, 2) building, 3) low vegetation, 4) wetland, 5) low impervious cover, 6) medium height vegetation, 7) tall coniferous vegetation, and 8) tall deciduous vegetation (Table 4-7). The priorities reflect our observations of certain errors that the individual classifications may be prone to. For example, the building classification can generate erroneous features along forested water edges because trees overhanging the water can have some similar properties to buildings; thus water superseded buildings. Wetlands superseded LIC because the LIC classification occasionally mislabeled wetlands as LIC, whereas the wetland classification seldom committed LIC. Vegetation tended to have little confusion with other classes. LIC took priority over buildings in the cases of bridges which were identified as buildings that intersected a valid Tele Atlas street segment. All classes except water and buildings were combined into the initial land cover classification. The six class raster was then smoothed by four passes with a focal statistics majority filter with a 4-meter radius neighborhood. Water and buildings were added to the final land cover raster after the smoothing to reduce the loss of narrow water features and to prevent excess rounding of building features. The eight class land cover raster was smoothed by two passes with a majority filter using a 1-meter radius neighborhood.

Table 4-7: Rules for combining land covers into a single classification.

Individual land cover layers combined into the final classifications with the following order of priority: 1) water, 2) building, 3) low vegetation, 4) wetland, 5) final LIC, 6) medium vegetation, 7) coniferous vegetation, and 8) deciduous vegetation.

4-3.3 Accuracy assessment

Accuracy assessment of the land cover classification was performed using a sample of 30 1x1 km tiles distributed throughout eastern Connecticut. We ensured that the sample tiles covered the full gradient of rural to urban landscapes by using the Connecticut's Changing Landscape (CCL) land cover dataset[23]. For a grid of 1x1 km tiles covering eastern Connecticut, we calculated the fractions of each tile that was classified as developed land in the CCL dataset. Tiles with developed land fractions of 0-0.33, 0.33-0.66, and 0.66-1 were considered to be low, medium, and high development, respectively. Ten tiles were selected semi-randomly from each of the 3 levels of urban development. Semi-random selection was performed within each stratum to ensure that sample tiles were geographically separated within eastern Connecticut. Tiles were excluded from the selection if they had been used in developing the rule set for the algorithm.

The accuracy assessment of each sample tile was performed using a stratified random sampling approach with approximately 100 point locations tested per tile. The number of points tested for each land cover class was proportional to the relative area of the class. Validation points were randomly distributed within each land cover class with a minimum of 10 meters separating points. The points were not permitted to occur within 3 meters of the boundary of a

[23] The Connecticut's Changing Landscape (CCL) land cover data is a 30-meter resolution land cover product derived from Landsat imagery and ancillary data. It was developed by the University of Connecticut's Center for Land use Education and Research (CLEAR). See http://clear.uconn.edu/projects/landscape/index.htm

given land cover class to account for geo-registration errors between the "ground-truth" data as well as minimize the occurrence of ambiguous sample points that fall close to the boundaries. The "ground truth" land cover for each validation point was determined from the 2012 leaf-off orthophotos and the 2010 LiDAR intensity imagery. A confusion matrix was created to show the commission and omission errors for each land cover class based on comparisons between our classification and the validation data. Accuracies were assessed in terms of the user accuracy, defined as the probability that a cell labelled as a certain class actually is that class, and the producer accuracy which is defined as the probability a cell of a given class is correctly labelled as that class (see Campbell and Wynne 2011).

4-4. Results

A total of 3,198 validation points were used in assessing the accuracy of the land cover classification. The overall accuracy for the 8 category classification was 93.1% with a kappa statistic = 0.90 (Table 4-8). The building class achieved the highest accuracies with user and producer accuracies of 98.7% and 97.4%, respectively. The deciduous tree class also had very high accuracies with user and producer accuracies of 94.5% and 95.6%, respectively. Low vegetation and LIC both had user and producer accuracies that exceeded 90%. The water class had user and producer accuracies of 95.7% and 84.8%, respectively, with omission errors tending to be misclassified as wetlands. The coniferous tree class had a user accuracy of 89.7% with a producer accuracy of 76.3%. The omissions and commissions in this class were almost entirely due to confusion with the deciduous tree class. Medium vegetation had relatively low accuracies with both user and producer accuracies of approximately 60%. Nearly all omissions and commissions occurred from confusion with either the tall vegetation or low vegetation classes. The wetland class had relatively few validation points and poor accuracies with user and

producer accuracies of 26.1% and 35.3%, respectively. Errors in this class tended to be due to confusion with water and low vegetation.

Table 4-8: Confusion matrix for the 8 land cover type classification.

	Reference Data									
Classification	Decid trees	Conif trees	Med. veg	Low veg	Water	Wetland	Bldg	LIC	Total	User acc. (%)
Decid trees	1364	33	7	21	2	1	3	12	1443	94.5
Conif trees	14	122	0	0	0	0	0	0	136	89.7
Med. veg	11	1	37	10	0	0	0	2	61	60.7
Low veg	19	3	17	763	1	8	2	23	836	91.3
Water	1	0	0	0	67	1	1	0	70	95.7
Wetland	4	0	0	3	9	6	0	1	23	26.1
Building	0	0	0	2	0	0	223	1	226	98.7
LIC	14	1	1	11	0	1	0	375	403	93.1
Total	1427	160	62	810	79	17	229	414	3198	
Producer acc. (%)	95.6	76.3	59.7	94.2	84.8	35.3	97.4	90.6		93.1

Overall classification accuracy was improved when the deciduous and coniferous trees were merged with medium vegetation and water was merged with wetland. The overall accuracy in the 5-class land cover map was 94.8% with a kappa = 0.92 (Table 4-9). Notably, user and producer accuracies exceeded 85% with all but one > 90% in the 5-class land cover type confusion matrix. The tall\medium vegetation class had user and producer accuracies of 96.9% and 96.4%, respectively. The water/wetland class had user and producer accuracies of 89.2% and 86.5%, respectively.

Table 4-9: Confusion matrix for the 5 land cover type classification.

	Reference Data						
Classification	Tall / med veg	Low veg	Water/ wetland	Bldg	LIC	Total	User acc. (%)
Tall / med veg	1589	31	3	3	14	1640	96.9
Low veg	39	763	9	2	23	836	91.3
Water/wetland	5	3	83	1	1	93	89.2
Bldg	0	2	0	223	1	226	98.7

LIC	16	11	1	0	375	403	93.1
Total	1649	810	96	229	414	3198	
Producer acc. (%)	96.4	94.2	86.5	97.4	90.6		94.8

The land cover classifications for two sample areas are shown in Figure 4-3. We used visual inspections of the 30 sample tiles to evaluate further the classification and we made several observations that were not evident in the quantitative accuracy assessment. The classification had relatively good success in identifying man-made structures that were partially obscured by tree cover. The connectivity of narrow streams and LIC was lost when features were less than a few meters across. Clusters of large vehicles (e.g. tractor trailers in a parking lot) and trees overhanging water were occasionally misclassified as buildings. Bridges were also misclassified as buildings when the corresponding road at that location was not depicted in the Tele Atlas street data. Buildings were occasionally misclassified as tall vegetation when adjacent to trees with heights approximately equal to the building height. Buildings were also misclassified as tall vegetation when they were completely obscured by the forest canopy, contained rooftop vegetation (i.e. a green roof), or the roof material caused an unusually high NDVI. Certain roof materials resulted in substantial voids in the LiDAR point cloud which the algorithm incorrectly interpreted as water. Roads under coniferous tree cover, having dark asphalt, or in the shade tended to be omitted unless they were represented in the Tele Atlas street data. Finally, wetland areas that were adjacent to LIC features were occasionally misclassified as LIC.

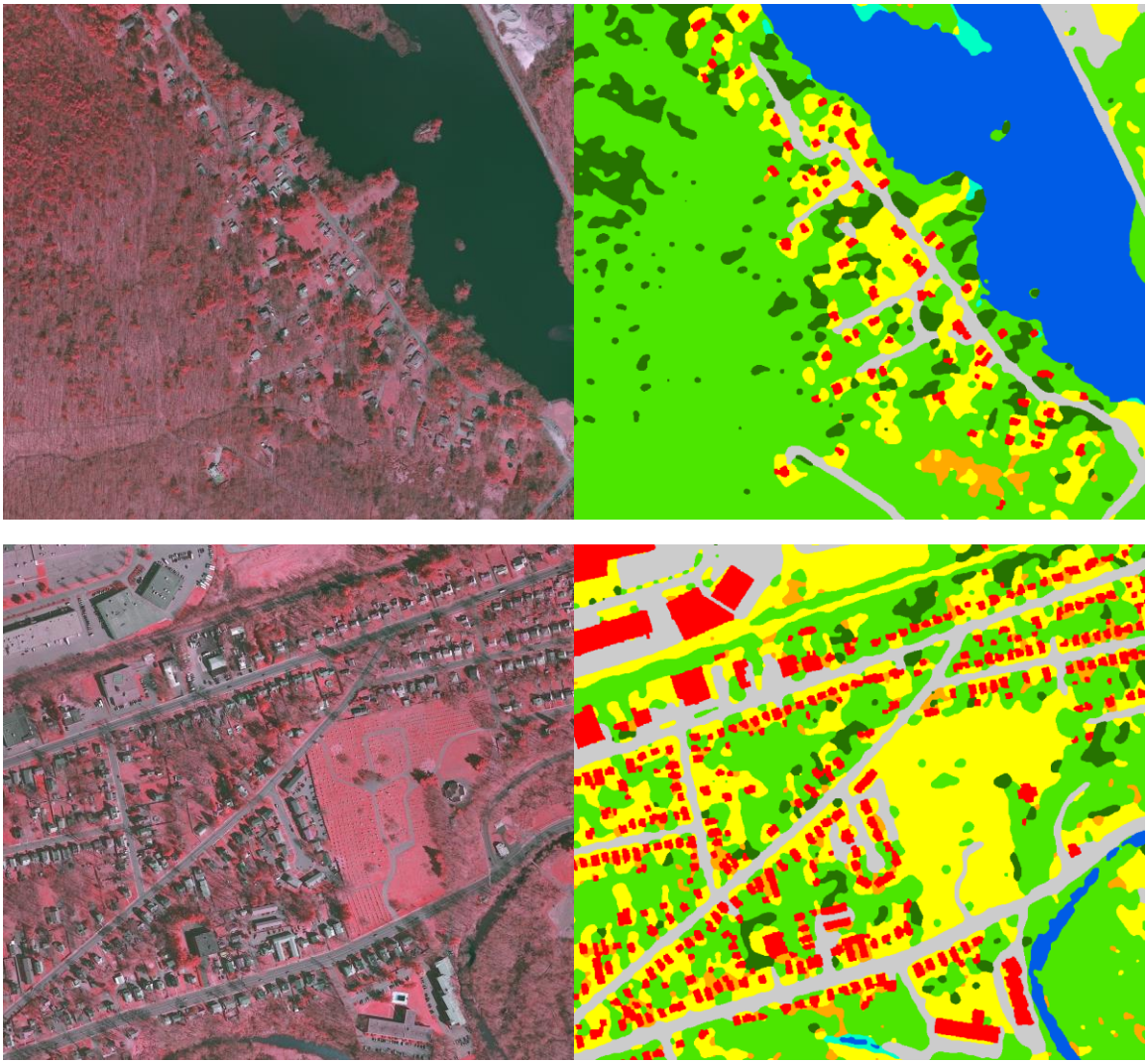

Figure 4-3: Color-infrared imagery (left) and 1-meter resolution land cover classifications (right) for two sample areas showing deciduous trees (green), coniferous trees (dark green), medium vegetation (orange), low vegetation (yellow), water (blue), wetland (cyan), buildings (red), and low impervious cover (gray).

4-5. Discussion

This study showed that our proposed algorithm can efficiently derive high spatial resolution land cover over an area of several thousand square kilometers without the need for human interaction. In contrast, previous studies have proposed semi-automated methodologies

that require human interpretation and we have found no study that demonstrated the feasibility of applying the proposed methods across large areas. Furthermore, our accuracy assessment used sample tiles distributed across the full range of rural to urban landscapes found in the 4800 km^2 region of eastern Connecticut, USA. In contrast, previous studies used single study areas ranging in size from approximately one to several square kilometers with relatively limited landscape diversity (see Arroyo et al. 2010, Antonarakis et al. 2008, Im et al. 2008; Koetz et al. 2008; Miliaresis and Kokkas 2007; Brennan and Webster 2006, Syed et al. 2005). However, further research will be needed to assess the effectiveness of the algorithm for diverse landscapes and with differing LiDAR and multispectral datasets.

The overall accuracy of our classification was on par with the results of methods reported by other studies that produced classifications of natural and artificial land cover features using LiDAR data (Im et al. 2008, Brennan and Webster 2006). In these studies, accuracies for individual land cover classes were also quite similar with our results. Im et al. (2008) achieved user and producer accuracies that typically exceeded 90% for the 5 land cover features (building, tree, grass, road/parking lot, and other artificial objects) included in their classification. Brennan and Webster (2006) also typically achieved accuracies well over 90% for the 10 land cover types in their classification (bright and dark structures, arid and saturated low vegetation, deciduous and coniferous trees, roads, water, arid intertidal, and saturated intertidal). As in our study, their coniferous tree class tended to have confusion occurring only with deciduous trees. Also similar to our study, Brennan and Webster (2006) found the classification to be unsuccessful for saturated low vegetation with confusion occurring mainly with the lush low vegetation class. They also found a lower ability to detect dark structures; however, we did not observe a tendency to omit dark buildings in qualitative assessments of our classification.

The accuracy assessment of our land cover classification was complicated by the fact that the spatial resolution we attempted to achieve was approximately equal to the horizontal registration error of the LiDAR and aerial images. Furthermore, the boundaries of tall and medium vegetation features are difficult to define precisely from orthophotos and LiDAR intensity images. Thus, the actual land cover occurring at the boundaries of features tended to be uncertain. To increase confidence in our validation points, we excluded sampling within 3 meters of a classified feature boundary. Although this restriction reduced uncertainty in the actual land cover type of the validation points, it did not allow for the inclusion of very small or narrow features (i.e. streams, sidewalks) in the accuracy assessment.

Several issues are likely to have affected the quality of our land cover classification as well as the assessment. Shadows and the off-nadir view in the aerial imagery created uncertainty in the identification of coniferous vegetation both for the classification algorithm as well as for ground-truthing the validation points. Medium height vegetation was not always readily determined based on the multispectral and LiDAR intensity images. The apparent extent of wetlands and water was not consistent between the seasons and years of the acquisition times of the LiDAR and multispectral imagery. The smoothing operations, used to filter out "salt and pepper" effects and fill gaps in the classification, were likely to have altered the boundaries between land cover features. Finally, changes in land cover that occurred between the LiDAR and orthophoto acquisitions created confusion in the classification; however, given the short time period, this is likely to account for a relatively small number of errors overall.

The objective of developing an algorithm that is robust to the heterogeneity commonly found in the forested suburban landscape in the northeastern U.S. required a relatively complex rule set for certain land cover features. Thresholds were set to be conservative and based on

training areas containing diverse landscapes within the study area. A given rule was likely to remove only a small portion of commission errors and a number of rules were typically required to achieve an acceptable accuracy. Thus, our rule sets tended to be substantially more complex than was typically used in land cover classifications involving LiDAR (see Arroyo et al. 2010; Antonarakis et al. 2008; Im et al. 2008; Miliaresis and Kokkas 2007). NDVI, derived from the multispectral imagery, was an important supplement to the rule sets for almost all land cover types by helping to distinguish vegetated from non-vegetated features and coniferous trees from deciduous trees. Leaf-off multispectral images had the advantage of aiding classification of artificial structures partially obscured by tree cover. However, the requirement for leaf-off images that are relatively concurrent with the LiDAR acquisition can limit the general applicability of our proposed algorithm. This requirement may be mitigated with the use of summer time leaf-on imagery which the National Agriculture Inventory Program (NAIP) acquires nationwide on a biannual basis. These data include information for the visible and near-infrared wavelengths with a spatial resolution of 1 meter. Our preliminary work with NAIP data showed that it is an effective supplement to LiDAR although the resulting classification was less effective at detecting roads and buildings obscured by tree cover (data not shown).

4-6. Conclusions

This study proposed a rule-based algorithm for classifying artificial and natural land covers from airborne LiDAR and high resolution multispectral imagery. The algorithm used a combination of pixel- and object-based rules which achieved an overall accuracy well over 90%. The accuracy of our classification was on par with other published studies; however, our

approach differed in that it was fully automated and thus has the potential to be applied efficiently over large extents. Furthermore, visual inspection of our classification showed that it was relatively effective at classifying building and impervious cover features that were obscured by tree cover. Accuracy assessments showed that the algorithm was robust throughout the range of rural to urban forested landscapes commonly found in the northeastern United States. Further research is needed to test the performance of the algorithm in more varied landscapes and with different LiDAR and multispectral datasets.

4-7. Acknowledgements

The authors would like to thank Chadwick Rittenhouse for his review of this manuscript. The author also acknowledges the Natural Resources Conservation Service and the University of Connecticut's Center for Land use Education and Research for providing us with the LiDAR and orthophoto data, respectively.

4-8. References

Angel, S., Parent, J.R., Civco, D.L. (2012). The Fragmentation of Urban Landscapes: Global Evidence of a Key Attribute of the Spatial Structure of Cities, 1990-2000. Environment and Urbanization 24(1): 249-283.

Angel, S., J. Parent, and D.L. Civco. (2010). Ten Compactness Properties of Circles: A Unified Theoretical Foundation for the Practical Measurement of Compactness. Canadian Geographer, 54 (4), 441-461.

Antonarakis, A.S., Richards, K. S., and Brasington, J. (2008). Object-based land cover classification using airborne LiDAR. Remote Sensing of Environment, 112(6), 2988–2998. doi:10.1016/j.rse.2008.02.004.

Arroyo, L. a., Johansen, K., Armston, J., and Phinn, S. (2010). Integration of LiDAR and QuickBird imagery for mapping riparian biophysical parameters and land cover types in Australian tropical savannas. Forest Ecology and Management, 259(3), 598–606. doi:10.1016/j.foreco.2009.11.018.

Brennan, R., and Webster, T. L. (2006). Object-oriented land cover classification of lidar-derived surfaces. Canadian Journal of Remote Sensing, 32(2), 162–172. doi:10.5589/m06-015.

Campbell, J.B. and R.H. Wynne. (2011). Introduction to Remote Sensing (Fifth Edition). The Guilford Press. New York, NY. p.483-484.

Charaniya, a. P., Manduchi, R., and Lodha, S. K. (2004). Supervised Parametric Classification of Aerial LiDAR Data. 2004 Conference on Computer Vision and Pattern Recognition Workshop, 30–30. doi:10.1109/CVPR.2004.446.

Cross, A.M., D.C. Mason, and S.J. Drury. (1988). Segmentation of remotely sensed images by a split-and-merge process. International Journal of Remote Sensing, 9(8), 1329–1345.

Dewberry. (2011). Project Report for the U.S. Corp of Engineers High Resolution LiDAR Acquisition & Processing for Portions of Connecticut. USACE Contract W912P9-10-D-0534. Prepared by Dewberry. 71 pp.

Hodgson, M. E., Jensen, J. R., Tullis, J. A., Riordan, K. D., and Archer, C. M. (1999). Synergistic Use of Lidar and Color Aerial Photography for Mapping Urban Parcel Imperviousness. Photogrammetric Engineering and Remote Sensing 69(9): 973–980.

Im, J., Jensen, J. R., and Hodgson, M. E. (2008). Object-Based Land Cover Classification Using High-Posting-Density LiDAR Data. GIScience & Remote Sensing, 45(2), 209–228. doi:10.2747/1548-1603.45.2.209.

Jensen, J.R. (2007). Spectral Characteristics of Vegetation. Remote Sensing of the Environment: An Earth Resource Perspective (2nd Edition). Pearson Prentice Hall. Upper Saddle River, New Jersey. 355-408.

Kamusoko, C. and M. Aniya. (2009). Hybrid classification of Landsat data and GIS for land use/cover change analysis of the Bindura district, Zimbabwe. International Journal of Remote Sensing 30(1): 97-115.

Koetz, B., Morsdorf, F., van der Linden, S., Curt, T., and Allgöwer, B. (2008). Multi-source land cover classification for forest fire management based on imaging spectrometry and LiDAR data. Forest Ecology and Management, 256(3), 263–271. doi:10.1016/j.foreco.2008.04.025.

Lillesand, T.M. and Kiefer, R.W. 2000. Remote Sensing and Digital Image Interpretation, Wiley, New York, 724 p.

Miliaresis, G., and Kokkas, N. (2007). Segmentation and object-based classification for the extraction of the building class from LIDAR DEMs. Computers & Geosciences, 33(8), 1076–1087. doi:10.1016/j.cageo.2006.11.012.

Parent, J. R., and J.C. Volin. (2014). Assessing the Potential for Leaf-off LiDAR Data to Model Canopy Closure in Temperate Deciduous Forests. ISPRS Journal of Photogrammetry and Remote Sensing 95: 134-145. DOI: 10.1016/j.isprsjprs.2014.06.009.

Running, S. W. (2008). "CLIMATE CHANGE: Ecosystem Disturbance, Carbon, and CLIMATE." Science 321: 652–653. doi:10.1126/science.1159607.

Syed, S., Dare, P., and Jones, S. (2005). Automatic Classification of Land Cover Features With High Resolution Imagery and LiDAR Data: an Object-Oriented Approach. Proceedings of SSC2005 Spatial Intelligence, Innovation and Praxis. 512-522. ISBN 0-9581366-2-9.

Tucker, C. J., J. R. Townshend, and T. E. Goff. (1985). African Land-Cover Classification Using Satellite Data. Science 227: 369–375. doi:10.1126/science.227.4685.369.

Tucker, C. J. (1979). Red and photographic infrared linear combinations for monitoring vegetation. Remote Sensing of Environment 8(2): 127-150.

United States Geological Survey (USGS). (2012). 2012 Multispectral Color Orthophotography at 1 foot GSD, State Plane Zone 0600 (CT) projection, GeoTIFF file format for the entire state of Connecticut. Metadata. Reston, VA.

Yang, J., P. Gong, R. Fu, M. H. Zhang, J. M. Chen, S. L. Liang, B. Xu, J. C. Shi, and R. Dickinson. (2013). "The Role of Satellite Remote Sensing in Climate Change Studies." Nature Climate Change 3: 875–883. doi:10.1038/nclimate1908.

Yu, L., Liang, L., Wang, J., Zhao, Y., Cheng, Q., Hu, L., and Liu, S. (2014). Meta-discoveries from a synthesis of satellite-based land-cover mapping research, 35(13), 4573–4588. doi:10.1080/01431161.2014.930206.

Chapter 5: Validating Landsat-based Landscape Analyses with High Resolution Land Cover Data

5-1. Abstract

The spatial resolution of land cover data and the extent of the analysis are important considerations for landscape analyses. Spatial scale can strongly influence landscape metrics and understanding scale effects will help landscape ecologists interpret and possibly calibrate analysis results to better depict the landscape. In this study, we investigated the potential for Landsat-based land cover datasets to predict landscape metrics derived from 1-meter resolution land cover data for the forested suburban landscape of eastern Connecticut.

The 1-meter validation land cover was derived in previous work using Light Detection and Ranging (LiDAR) and high resolution multispectral data. We included three 30-meter land cover datasets in our study: 1) the 1-meter validation data resampled using nearest neighbors, 2) the Connecticut's Changing Landscape (CCL) land cover, and 3) the National Land Cover Database (NLCD) land cover. We include the following landscape metrics in our analysis: 1) land cover class fractions, 2) number of patches, 3) total edge length, 4) mean patch area, 5) largest patch index, and 6) forest fragmentation type class fractions. Metrics were calculated for each of the land cover datasets for circular analysis plots ranging from 100 – 1,400 meters in radius. Plots were distributed semi-randomly across eastern Connecticut ensuring that a wide range of rural to urban landscapes was included.

The Landsat based datasets tended to be successful in predicting the class fraction metrics but had less success in predicting patch-level metrics (i.e. number of patches, total edge length,

etc.). Model performance tended to improve as the analysis area was increased which suggests that larger sample areas can help compensate for lower spatial resolutions. The Landsat-based datasets tended to have similar model performances; however, the resampled land cover data consistently out-performed the CCL and NLCD data and had different relationships to the validation data. Previous literature reported that many landscape metrics have predictable responses to changes in spatial resolution; however, these studies were based solely on moderate-resolution land cover data that were resampled to generate each of the coarser datasets used in the analysis. Our findings suggest that the use of resampled land cover may not be appropriate for inferring whether data based on coarse resolution sensors are suitable as a proxy for finer resolution data in terms of deriving landscape metrics. Thus, it seems inadvisable to use model relationships, derived from resampled data, to calibrate coarse resolution landscape metrics or to infer whether coarse data can serve as a proxy for finer resolution data.

5-2. Introduction

Landscape ecology seeks to quantify patterns in the landscape in order to understand ecological processes and to manage natural resources more effectively. Maps of the physical land cover on the earth's surface are fundamental to analyzing ecosystems at the landscape level (Yu et al. 2014). The scales of these analyses, including spatial resolution and extent, are important considerations and have been shown to have major effects on landscape metrics (Alhamad et al. 2011; Liu and Weng 2009; Wu 2004; Wu et al. 1997; Turner et al. 1989). Data that are too coarse may not adequately represent landscape features that are relevant for a particular analysis (see Akasheh et al. 2008; Gilmore et al. 2008; Goetz et al. 2003). However, land cover datasets vary widely in their spatial resolutions, which are usually constrained by the remote sensing data from which they are derived, and analysis extents vary widely based on the objectives of the

study. Thus, it is critical to understand the effect of spatial resolution and extent in interpreting analyses at the landscape level.

Land cover data are typically mapped using data from satellite or airborne sensors that measure the brightness of solar radiation reflected by features on the earth's surface. The Landsat series of satellites provides the data most commonly used in land cover research (Yu et al. 2014). These data have a spatial resolution of approximately 30 meters and thus products derived from these images typically have a similar resolution. Land cover datasets based on Landsat imagery are likely to dominate landscape analyses for the foreseeable future because the Landsat satellite provides global coverage with more than 30 years of temporal continuity.

In the past decade, data from high resolution sensors have become more widely available and researchers have successfully created land cover maps with spatial resolutions as fine as 1 meter (Parent et al. 2014; Arroyo et al. 2010; Antonarakis et al. 2008; Im et al. 2008; Koetz et al. 2008; Miliaresis and Kokkas 2007). However, processing high resolution data is challenging for large areas and the limited spatial and temporal availability of these data makes it unlikely to become prevalent in landscape analyses in the near future. Thus, at present, the broader impacts of high resolution land cover may be in providing a greater understanding of how landscape metrics are affected by changes in spatial resolution and analysis extent. This information would help landscape researchers to interpret analyses based on moderate or coarse resolution data and perhaps allow them to calibrate metric results in order to represent the landscape more accurately.

The primary objective of this paper is to investigate whether landscape metrics based on 30-meter resolution land cover data can effectively predict metrics based on 1-meter resolution

validation data. We include a selection of metrics calculated for circular analysis areas ranging from 100 to 1,400 meters in radius. The 1-meter resolution land cover dataset was based on 2010 Light Detection and Ranging data and 2012 high resolution multispectral imagery (see Parent et al. 2014). The 30-meter resolution land cover datasets included: 1) the 1-meter data resampled to 30 meters, 2) the 2010 Connecticut's Changing Landscape (CCL) land cover, and 3) the 2011 National Land Cover Database (NLCD) land cover. The CCL and NLCD datasets were derived independently from Landsat satellite imagery.

A number of studies have shown spatial resolution and extent to have major effects on the results of landscape metrics; however, these effects have been shown consistently to be predictable for certain types of metrics (Simova and Gdulova 2012; Alhamad et al. 2011; Liu and Weng 2009; Wu et al. 2002; Wu et al. 1997). These studies typically used Landsat-based land cover to provide the finest level of data and these data were resampled, using either nearest neighbor or majority algorithms, to provide a series of coarser resolution datasets. We are not aware of any study that included data with spatial resolutions finer than 15 meters nor are we aware of any studies that used independent land cover datasets of differing resolutions. However, we suspect that resampled land cover data may not a suitable proxy for independent land cover data and may generate misleading conclusions in terms of the ability of coarse resolution data to predict successfully the fine resolution data. Thus, a secondary objective of this study is to investigate how the use of a resampled dataset differs from the use of independent land cover data in evaluations of spatial scale on landscape metrics.

Previous studies tended to focus on metrics derived using the FRAGSTATS software which includes dozens of metrics that characterize patches and landscape heterogeneity (see McGarigal 2002). We selected five metrics that were reported by several studies to have

predictable responses to changes in the spatial resolution and extent of the analysis (Simova and Gdulova 2012; Alhamad et al. 2011; Liu and Weng 2009; Wu 2004; Wu et al. 2002): 1) land cover class fraction, 2) number of patches, 3) total edge length, 4) mean patch area, and 5) the largest patch index (LPI). The land cover class fraction is simply the fraction of the analysis area occupied by the land cover type of interest. The LPI is the percentage of the analysis area occupied by the largest patch of the land cover type of interest. In addition, we assess class fractions for a model that characterizes forest fragmentation based on an algorithm presented by Vogt et al. (2007) and modified for use in ArcGIS by Parent and Hurd (2008). The model uses the concept of an edge disturbance zone to classify forest grid cells as: 1) *core* cells unaffected by edge disturbance, 2) *perforated* cells within the edge disturbance zone but around a relatively small gap within a larger forest tract, 3) *edge* cells within the disturbance zone and around large openings along the outside of a forest tract, and 4) *patch* cells in small forest patches that are entirely within the edge disturbance zone. The edge disturbance zone consists of forest grid cells that are in close proximity to non-forest land cover. The edge zone has been documented in numerous studies as having altered microclimate (Broadbent et al. 2008; Chen et al. 1999), degraded wildlife habitat (Broadbent et al. 2008), and increased susceptibility to non-native plant invasions (Broadbent et al. 2008; Yates et al. 2004; Brothers and Spingarn 1992). The depth of this zone into the forest edge can vary depending on the issue of interest; however, a review of the literature found the median reported distance to be 100 meters (Broadbent et al. 2008).

5-3. Methods

5-3.1. Study area

The study area for this research was located in eastern Connecticut, in the northeastern United States (Figure 5-1). The landscape is dominated by temperate deciduous and mixed

forests types with the built-up landscape ranging from urban to rural. Natural grasslands and shrublands are uncommon features in the landscape; however, turf grass and agricultural land can be substantial in some areas. Topography can be characterized as hilly with elevations ranging from sea level in the south to 330 meters in the north.

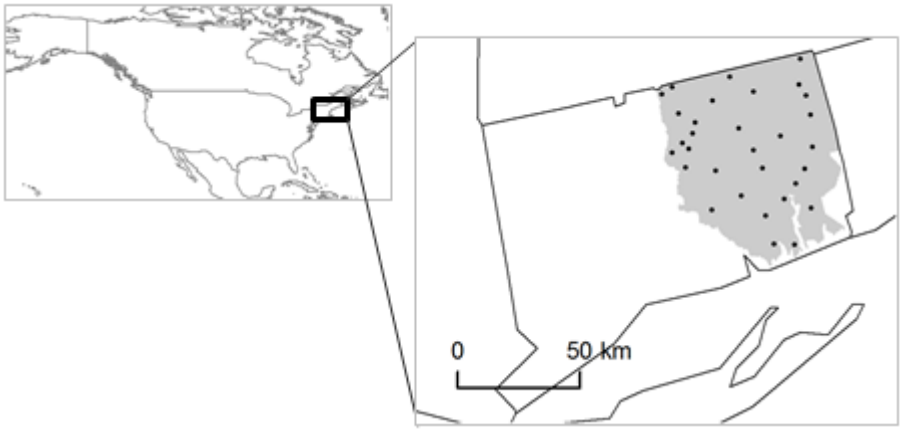

Figure 5-1: The study area consisted of 30 3x3 km tiles (black dots) distributed semi-randomly throughout eastern Connecticut (72.3^0 W, 41.7^0 N). The gray area shows the extent of the LiDAR dataset.

The analyses were performed using a sample of 30 3x3 km tiles distributed throughout eastern Connecticut (Figure 5-1). We ensured that the sample tiles covered the full gradient of rural to urban landscapes by using the Connecticut's Changing Landscape (CCL) land cover dataset. For a grid of 3x3 km tiles covering eastern Connecticut, we calculated the fractions of each tile that was classified as impervious land in the CCL dataset. Tiles with impervious land fractions of 0-0.33, 0.33-0.66, and 0.66-1.0 were considered to be low, medium, and high intensity development, respectively. Ten tiles were selected manually, but in a semi-random manner, from each of the 3 levels of urban development. Manual selection was performed within each stratum to ensure that sample tiles were geographically separated within eastern Connecticut.

5-3.2. Data description and processing

This study utilized four datasets: 1) a 1-meter resolution land cover, 2) the 1-meter land cover resampled to a 30-meter resolution, 3) the 2010 CCL land cover dataset, and 4) the 2011 National Land Cover Database (NLCD) land cover dataset. The land cover grids were projected into the UTM zone 18 coordinate system and spatially aligned to the CCL grid for all analyses. All data processing was done using scripts with ArcGIS 10.2.

The 1-meter resolution land cover data were derived using a classification algorithm that we developed in previous work (Parent et al. 2014). The algorithm used a series of pixel- and object-based rules to classify land cover from leaf-off Light Detection and Ranging (LiDAR) data and high resolution multi-spectral orthophotographs acquired in the November of 2010 and March of 2012, respectively. Structural and spectral characteristics were used to classify the following land cover types: tall deciduous, tall coniferous, medium height vegetation, low vegetation, water, riparian wetlands, buildings, and low impervious cover. The algorithm was tested for a sample of locations distributed throughout eastern Connecticut and had an overall accuracy of 93% with user and producer accuracies both exceeding 90% for all classes except tall coniferous, medium height vegetation, and riparian wetlands (Parent et al. 2014). Tall coniferous and medium vegetation tended to be confused with tall deciduous vegetation. Riparian wetlands were confused with water, which was due in part to the inconsistencies in the extent of the wetlands between the acquisition dates of the LiDAR and multispectral datasets. The overall land cover accuracy was increased to 95% when the thematic resolution of the classification was reduced to five classes: tall/medium vegetation, low vegetation, water/wetlands, buildings, and low impervious cover (Parent et al. 2014). In this study, we applied the classification algorithm to the 30 sample tiles using the same LiDAR and multi-

spectral datasets as we used in our previous work and we reduced the thematic resolution to four classes: 1) forest, including medium and tall vegetation; 2) low vegetation; 3) water and wetland; and 4) impervious cover, including buildings and low impervious cover.

The 4-class land cover data were resampled to a 30-meter spatial resolution using the nearest neighbor method in ArcGIS 10.2. Nearest neighbors is a common resampling method which assigns the value of the closest cell in the input image to the output cell value (Avery and Berlin 1992). Majority resampling is another commonly used method, for degrading the spatial resolution of thematic data, which assigns the most frequently occurring value of the input cells to the output cell (Avery and Berlin 1992). However, we compared majority and nearest neighbor resampling methods for our 30 3x3 km^2 sample tiles and found that both methods generated nearly identical results - on average, 98.3% of the output cells had the same values (data not shown). Thus, our selection of resampling technique is likely to have had little effect on the analysis.

The Connecticut's Changing Landscape (CCL) 2010 land cover data were developed by the Center for Land Use Education and Research (CLEAR)[24] based on Landsat ETM satellite imagery. The classification process used the ISODATA algorithm in an unsupervised image classification technique with any apparent errors eliminated through on-screen digitizing (CLEAR 2010). The dataset had a spatial resolution of 30 meters and included 12 land cover classes: developed, turfgrasses, other grasses, agricultural field, deciduous forest, coniferous forest, water, non-forested wetland, forested wetland, tidal wetland, barren land, and utility corridor. Accuracy assessments showed the data to have an overall accuracy of approximately

[24] See http://clear.uconn.edu/index.htm.

90% (James Hurd personal communication). For this study, we reclassified the land cover data into the four classes corresponding to the 1-meter land cover.

The National Land Cover Database (NLCD) 2011 land cover dataset was developed, by the Multi-Resolution Land Characteristics Consortium, based on Landsat ETM satellite imagery and covers the entire United States. The classification was developed using primarily a decision tree method (Jin et al. 2013) and is based on a modified Anderson land cover classification System (see Anderson et al. 1976). The land cover dataset was reclassified into the four classes that most closely corresponded to the 1-meter land cover. The developed open space class contained both tall and low vegetation and thus was excluded from the four class land cover.

The Landscape Fragmentation Tool (LFT), developed by Parent and Hurd (2008)[25] and based on Vogt et al. (2007), was applied to each of the four land cover datasets. Forest was used as the *fragmented* class and low vegetation and impervious cover were used as the *fragmenting* classes. The water/wetlands class was not considered to have a fragmenting effect on forest. For this study, we used an edge disturbance zone width of 50 meters and excluded from analysis the small forest gaps in which centers were less than five meters from the gap's edge.

5-3.3. Landscape metrics

Landscape metrics were calculated for each of the four land cover datasets within circular plots with radii of 100, 400, and 1,400 meters. The 1,400-meter plots were centered in the 3x3 km sample areas creating a total of 30 plots. For the smaller plots, the 3x3 km tiles were divided into 9 1x1 km tiles and the plots were positioned at the center of each tile; thus a total of 270 plots were created with 100- and 400-meter radii. The following metrics were calculated for each

[25] See Landscape Fragmentation Tool v2.0 at http://clear.uconn.edu/tools/lft/lft2/index.htm

plot: 1) land cover class fractions ($CF_{impervious}$, CF_{forest}, and CF_{lowVeg}); 2) number of forest patches (P_{count}); 3) total length of forest edges ($F_{perimeter}$); 4) mean patch area ($P_{meanArea}$); 5) the largest patch index (LPI); and 6) forest fragmentation class fractions (CF_{core}, $CF_{perforated}$, CF_{edge}, and CF_{patch}). The land cover fraction metrics were only calculated for the 100- and 400-meter radius plots.

The land cover composition of CCL impervious grid cells was analyzed to help explain the patterns, in terms of the landscape metrics, observed in the relationships between the Landsat-based land cover data and the validation data. Five impervious and five forest CCL grid cells were randomly selected from each of the 270 1x1 km tiles. The 1-meter data were used to determine the $CF_{impervious}$, CF_{forest}, CF_{lowVeg}, and CF_{water} within each 30x30 meter sample grid cell.

Regression analyses were performed using SAS's JMP 11.2 software[26]. The 30-meter resolution land cover datasets were used to predict the metric values derived from the 1-meter resolution dataset.

5-4. Results

The study area was dominated by forest cover with low vegetation and impervious cover also comprising significant portions of the landscape (Figure 5-2). Water was a minor component which occupied only 2 percent of the sample area. Forest, low vegetation, and impervious cover occupied an average of 59, 25, and 14 percent of the sample area, respectively.

[26] See http://www.jmp.com/software

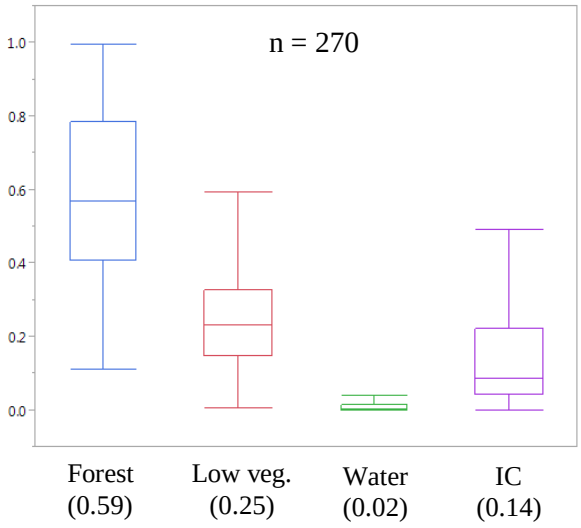

Figure 5-2: Boxplots showing proportions of areas, within the 400-meter radius analysis plots, that were comprised of forest, low vegetation, water, and impervious cover. Sample means are indicated in parentheses.

Images of the four land cover datasets are shown for a sample urban area in Figure 5-3. Qualitative assessments showed that the CCL and NLCD data tend to overestimate impervious cover while underestimating forest and low vegetation. The resampled 30-meter land cover did not appear to have the same bias toward impervious cover as the Landsat-based data. Substantial areas of low vegetation and forest were omitted from the NLCD land cover for urban landscapes. These omissions corresponded to the NLCD's developed open space class, which we excluded because it did not distinguish between forest and low vegetation.

In general, the 30-meter land cover CF metrics became increasingly better predictors of the 1-meter CF metrics as the plot size was increased (Figure 5-4). The resampled CF metrics had 1:1 linear relationships with the 1-meter metrics and regression models had nearly perfect correlations ($r^2 \geq 0.97$) regardless of land cover type or plot radius. Models based on CCL predictions were intermediate in performance with r^2 values ranging from 0.85-0.89, 0.83-0.92, and 0.71-0.78 for $CF_{impervious}$, CF_{forest}, and CF_{lowVeg}, respectively. The NLCD-based models were

on par with CCL-based models for $CF_{impervious}$ and CF_{forest} which had r^2 values ranging from 0.79-0.87 and 0.72-0.86, respectively. The NLCD-based models for CF_{lowVeg} performed poorly with r^2 values ranging from 0.41 - 0.51. The CCL- and NLCD-based models for $CF_{impervious}$ were exponential while models for CF_{forest} and CF_{lowVeg} were linear; these models tended to overestimate $CF_{impervious}$ while underestimating CF_{forest} and CF_{lowVeg}.

The regression models estimating CF_{core}, $CF_{perforated}$, CF_{edge}, and CF_{patch} also tended to improve as the plot size was increased (Figure 5-5a,b). The resampled land cover metrics had 1:1 linear relationships with the 1-meter metrics and the models had nearly perfect correlations ($r^2 \geq 0.99$) except for CF_{edge} and CF_{patch} with the 100-meter plots which had r^2 values of 0.94 and 0.88, respectively. The CCL-based models generally performed better than the NLCD-based models although performances were considerably poorer than for the models based on the resampled land cover data. The CCL- and NLCD-based CF_{core} models were exponential with r^2 values ranging from 0.70-0.95 and 0.56-0.93, respectively. Both CCL- and NLCD-based data tended to overestimate CF_{core}. The CCL- and NLCD-based $CF_{perforated}$ had no correlation with the 1-meter metrics regardless of plot size and models of CF_{edge} had relatively poor performances except for the 1,400-meter plot with a CCL-based model which had an $r^2 = 0.77$. The CCL-based models of CF_{patch} performed well for the 400- and 1,400-meter plot sizes with r^2 values of 0.81 and 0.92, respectively; however, CCL-based CF_{patch} models were not successful for the 100-meter plots. The NLCD-based CF_{patch} models were successful for the 1,400-meter plot size ($r^2 = 0.84$); however, the models had little or no success for the smaller plot sizes.

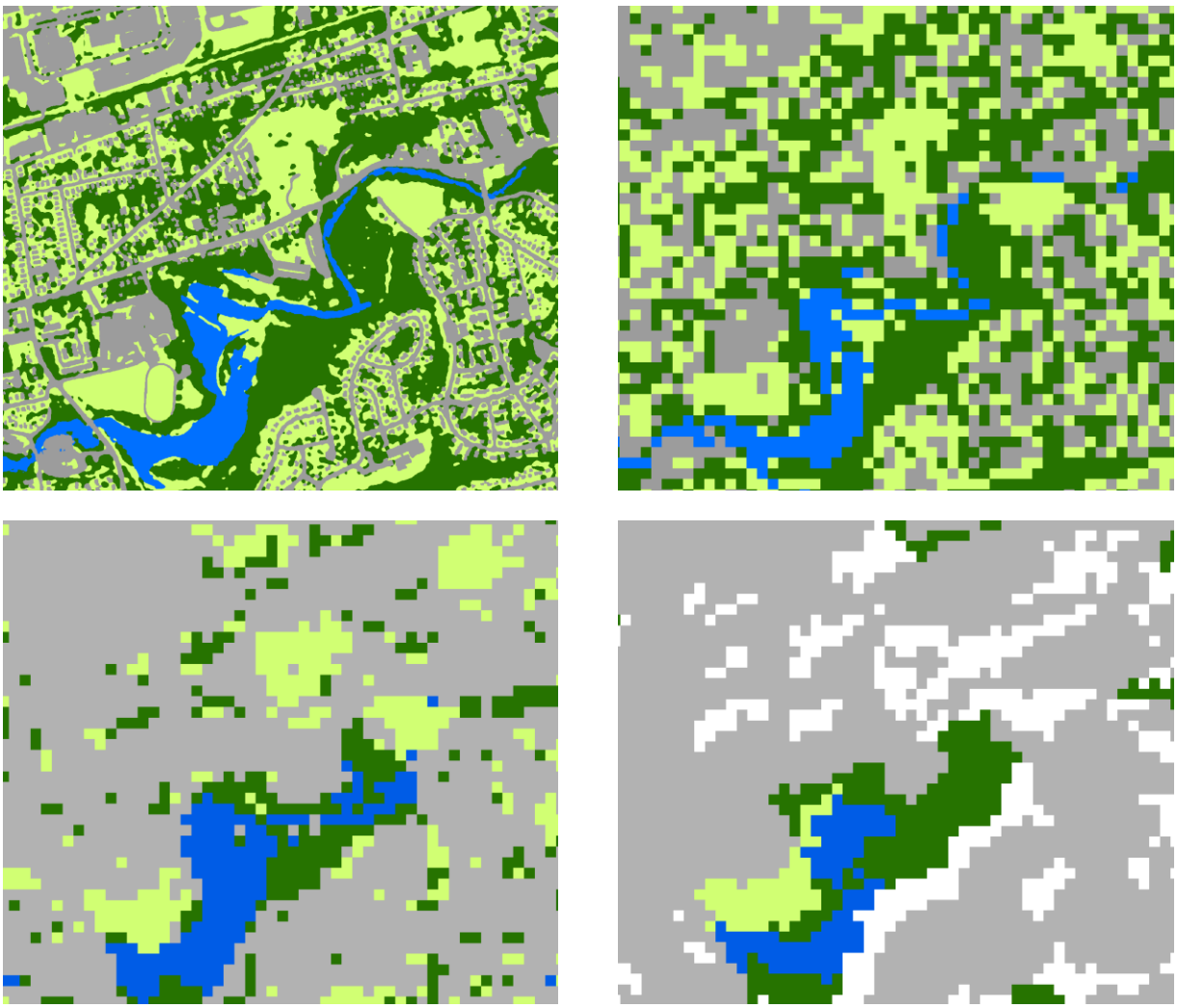

Figure 5-3: Land cover maps for a sample area for the 1 meter (top left), resampled (top right), CCL (bottom left), and NLCD (bottom right) land cover datasets. Land cover classes include forest (green), low vegetation (light green), impervious cover (gray), water (blue), and no data (white).

The models based on 30-meter land cover datasets tended to be less successful in predicting P_{count}, $F_{perimeter}$, $P_{meanArea}$, and LPI than for the CF metrics (Figure 5-6a,b). As before, the resampled land cover metrics tended to perform better than the metrics based on the CCL or NLCD datasets. The predictability of P_{count} and $F_{perimeter}$ tended to increase with plot size; however, only the resampled land cover was successful in predicting $F_{perimeter}$ (Figure 5-6a). Models based on the resampled land cover had r^2 values ranging from 0.46-0.93 and 0.60-0.95

for P_{count} and $F_{perimeter}$, respectively. The CCL-based P_{count} model was only successful for the 1,400-meter plot size ($r^2 = 0.75$) while the NLCD-based P_{count} was not successful for any plot size. The $P_{meanArea}$ models tended to decline in performance as plot size increased except for the 1,400-meter plots which had r^2 values of 0.96, 0.81, and 0.82 for the resampled-, CCL-, and NLCD-based metrics, respectively (Figure 5-6b). The performance of the resampled land cover LPI declined from 0.94 to 0.75 as the plot size was increased from 100 to 1,400 meters. The LPI for the CCL- and NLCD-based models had similar performances across different plot sizes with r^2 values ranging from 0.73-0.85 and 0.73-0.80 for CCL- and NLCD-based models, respectively.

Analyses of the actual land cover compositions (based on 1-meter resolution land cover) of cells that were classified as impervious in the CCL land cover data showed that the impervious cover tended to comprise only a minority of the area for cells classified as impervious (Figure 5-7). The average composition of CCL impervious grid cells was 42% forest, 30% low vegetation, and 28% impervious. On the other hand, CCL forest cells tended to be dominated by forest cover with average compositions of 86% forest, 10% low vegetation, and 4% impervious cover. Water was not a significant component of either impervious or forest CCL cells.

	Impervious CF		Forest CF		Low vegetation CF	
	100	400	100	400	100	400
Resampled land cover	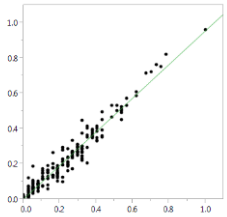	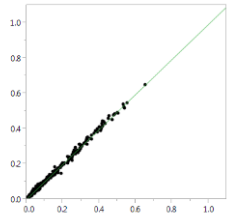	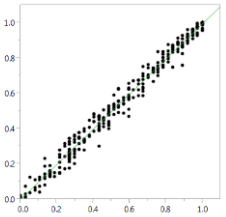	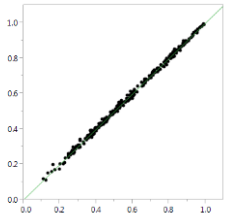	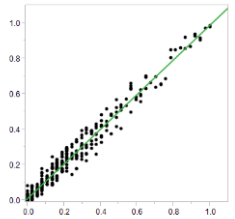	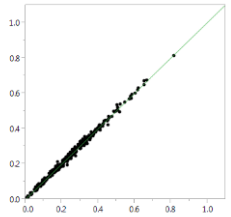
	$y = 0.95x + 0.00$ $r^2 = 0.97$ RMSE = 0.03	$y = 0.99x + 0.00$ $r^2 = 1.00$ RMSE = 0.01	$y = 1.00x + 0.00$ $r^2 = 0.98$ RMSE = 0.04	$y = 1.00x - 0.00$ $r^2 = 1.00$ RMSE = 0.01	$y = 0.98x + 0.01$ $r^2 = 0.97$ RMSE = 0.04	$y = 1.00x + 0.00$ $r^2 = 0.99$ RMSE = 0.01
CCL	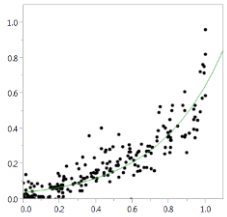	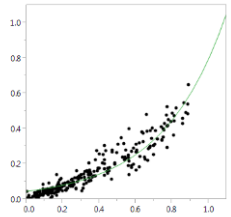	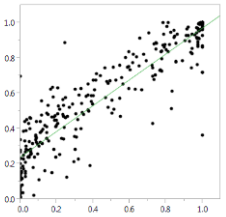	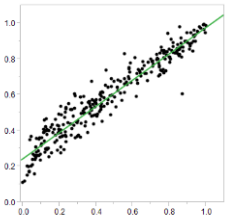	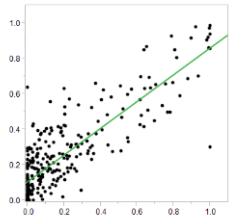	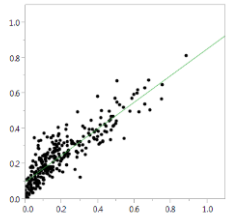
	$y = 0.04e^{2.79x}$ $r^2 = 0.85$ RMSE = 0.07	$y = 0.05e^{2.86x}$ $r^2 = 0.89$ RMSE = 0.05	$y = 0.73x + 0.24$ $r^2 = 0.83$ RMSE = 0.12	$y = 0.73x + 0.24$ $r^2 = 0.92$ RMSE = 0.06	$y = 0.75x + 0.11$ $r^2 = 0.71$ RMSE = 0.12	$y = 0.75x + 0.10$ $r^2 = 0.78$ RMSE = 0.07
NLCD	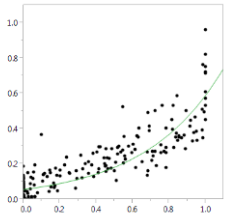	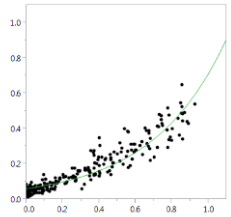	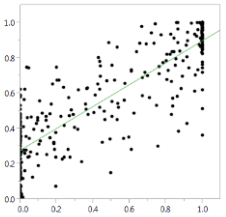	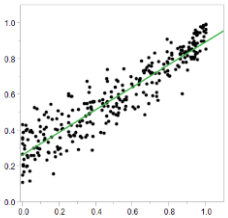	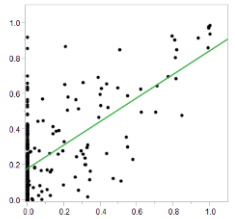	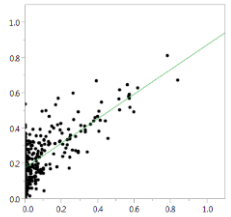
	$y = 0.06e^{2.35x}$ $r^2 = 0.79$ RMSE = 0.08	$y = 0.06e^{2.46x}$ $r^2 = 0.87$ RMSE = 0.05	$y = 0.62x + 0.28$ $r^2 = 0.72$ RMSE = 0.16	$y = 0.63x + 0.27$ $r^2 = 0.86$ RMSE = 0.08	$y = 0.67x + 0.18$ $r^2 = 0.41$ RMSE = 0.18	$y = 0.70x + 0.18$ $r^2 = 0.51$ RMSE = 0.10

Figure 5-4: Regression models predicting class fraction (CF) for impervious, forest, and low vegetation land cover. The 30-meter land cover metric value (x-axis) was used to predict the 1-meter metric value (y-axis) for plots with100- and 400-meter radii.

	Core forest CF			Perforated forest CF		
	100	400	1400	100	400	1400
Resample	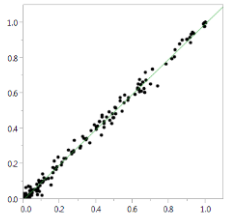	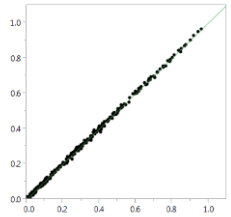	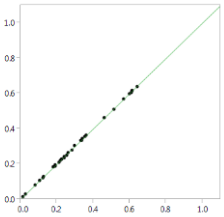	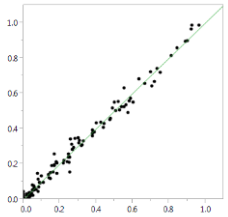	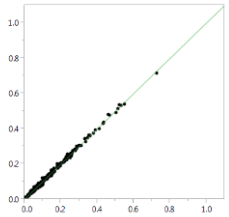	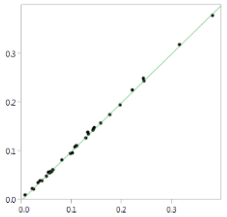
	$y = 1.00x - 0.00$ $r^2 = 1.00$ RMSE = 0.02	$y = 1.00x - 0.00$ $r^2 = 1.00$ RMSE = 0.01	$y = 1.00x - 0.00$ $r^2 = 1.00$ RMSE = 0.00	$y = 1.00x - 0.00$ $r^2 = 1.00$ RMSE = 0.01	$y = 1.00x - 0.00$ $r^2 = 1.00$ RMSE = 0.01	$y = 1.00x - 0.00$ $r^2 = 1.00$ RMSE = 0.00
CCL	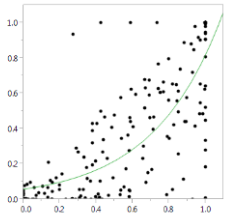	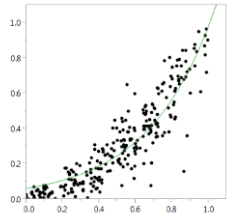	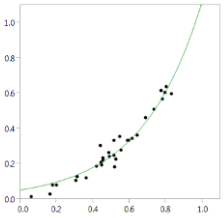	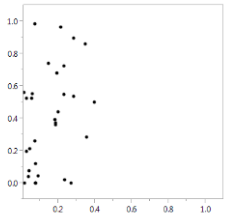	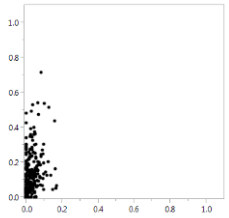	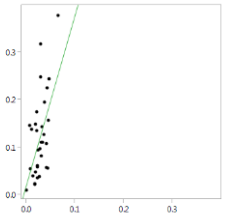
	$y = 0.06e^{2.65x}$ $r^2 = 0.70$ RMSE = 0.18	$y = 0.06e^{2.75x}$ $r^2 = 0.84$ RMSE = 0.10	$y = 0.05e^{3.04x}$ $r^2 = 0.95$ RMSE = 0.04	$y = --$ $r^2 = --$ RMSE = --	$y = --$ $r^2 = --$ RMSE = --	$y = 3.60x + 0.02$ $r^2 = 0.31$ RMSE = 0.07
NLCD	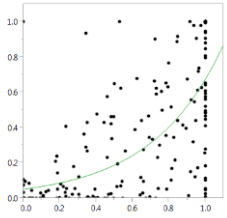	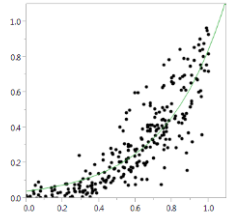	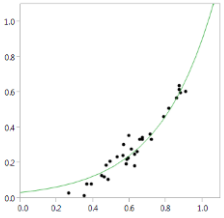	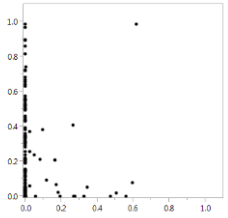	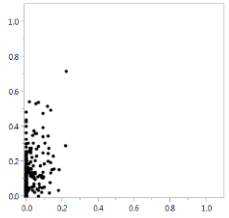	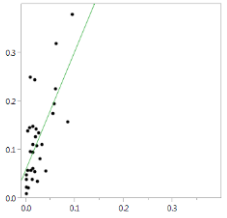
	$y = 0.05e^{2.56x}$ $r^2 = 0.56$ RMSE = 0.22	$y = 0.04e^{3.00x}$ $r^2 = 0.79$ RMSE = 0.12	$y = 0.03e^{3.29x}$ $r^2 = 0.93$ RMSE = 0.05	$y = --$ $r^2 = --$ RMSE = --	$y = --$ $r^2 = --$ RMSE = --	$y = 2.43x + 0.07$ $r^2 = 0.47$ RMSE = 0.07

Figure 5-5a: Regression models predicting class fraction (CF) for core and perforated forest cover. The 30-meter land cover metric value (x-axis) was used to predict the 1-meter metric value (y-axis) for plots with100- and 400-meter radii.

	Edge forest CF			Patch forest CF		
	100	400	1400	100	400	1400
Resample	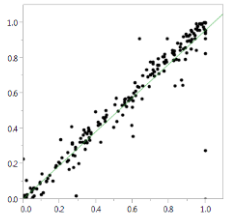	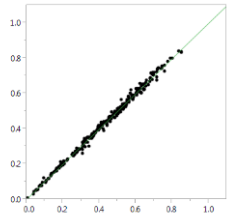	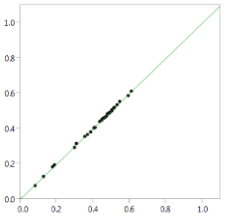	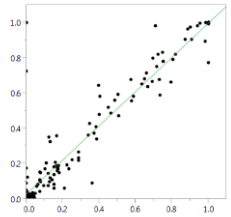	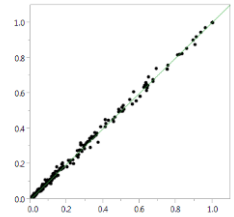	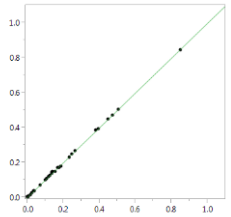
	y = 0.95x + 0.01 r^2 = 0.94 RMSE = 0.09	y = 1.00x - 0.00 r^2 = 1.00 RMSE = 0.01	y = 1.00x + 0.00 r^2 = 1.00 RMSE = 0.00	y = 0.97x + 0.03 r^2 = 0.88 RMSE = 0.13	y = 1.00x + 0.00 r^2 = 1.00 RMSE = 0.01	y = 1.00x + 0.00 r^2 = 1.00 RMSE = 0.00
CCL	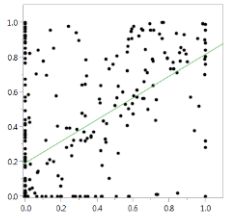	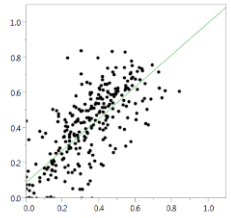	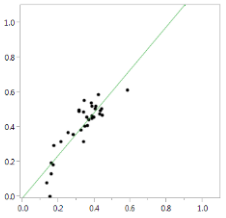	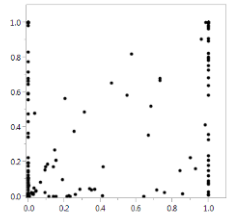	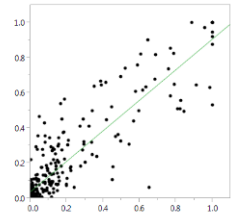	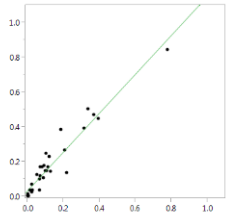
	y = 0.62x + 0.20 r^2 = 0.33 RMSE = 0.30	y = 0.91x + 0.09 r^2 = 0.56 RMSE = 0.15	y = 1.23x – 0.01 r^2 = 0.77 RMSE = 0.07	y = -- r^2 = -- RMSE = --	y = 0.87x + 0.04 r^2 = 0.81 RMSE = 0.11	y = 1.12x + 0.03 r^2 = 0.92 RMSE = 0.05
NLCD	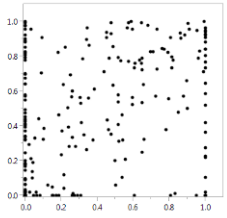	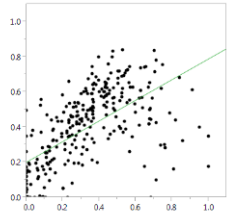	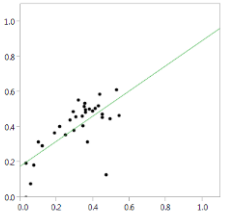	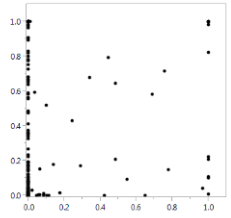	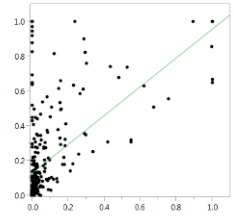	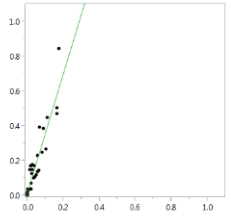
	y = -- r^2 = -- RMSE = --	y = 0.59x + 0.20 r^2 = 0.38 RMSE = 0.17	y = 0.72x + 0.18 r^2 = 0.49 RMSE = 0.11	y = -- r^2 = -- RMSE = --	y = 0.83x + 0.13 r^2 = 0.32 RMSE = 0.21	y = 3.43x + 0.02 r^2 = 0.84 RMSE = 0.08

Figure 5-5b: Regression models predicting class fraction (CF) for edge and patch forest cover. The 30-meter land cover metric value (x-axis) was used to predict the 1-meter metric value (y-axis) for plots with100- and 400-meter radii.

	Number of patches			Total edge length		
	100	400	1400	100	400	1400
Resample	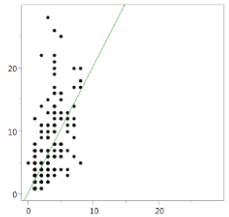	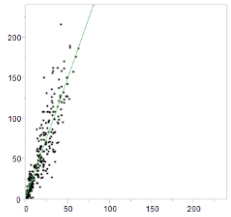	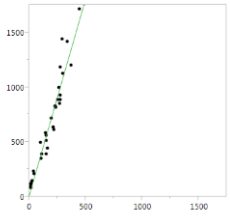	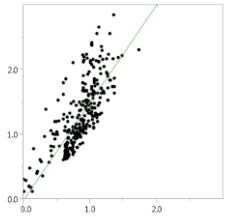	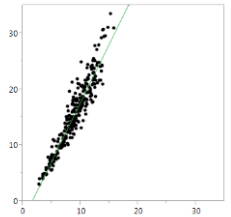	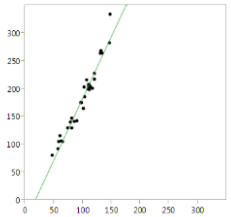
	$y = 2.02x + 0.48$ $r^2 = 0.46$ RMSE = 3.85	$y = 2.95x + 4.66$ $r^2 = 0.81$ RMSE = 20.22	$y = 3.60x + 11.53$ $r^2 = 0.93$ RMSE = 118.51	$y = 1.51x – 0.01$ $r^2 = 0.60$ RMSE = 0.34	$y = 2.10x – 3.37$ $r^2 = 0.89$ RMSE = 1.97	$y = 2.22x – 38.44$ $r^2 = 0.95$ RMSE = 13.60
CCL	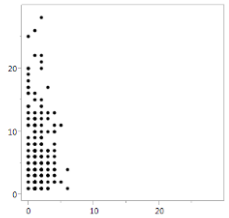	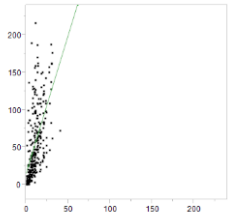	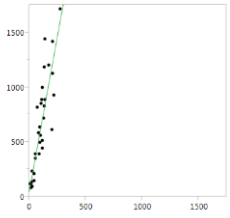	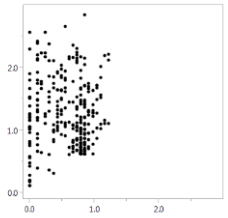	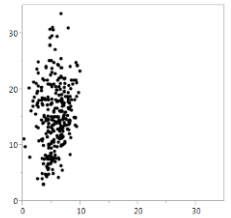	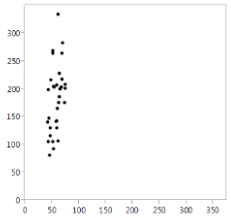
	y = -- r^2 = -- RMSE = --	$y = 3.68x + 16.06$ $r^2 = 0.34$ RMSE = 37.62	$y = 5.69x + 48.47$ $r^2 = 0.75$ RMSE = 224.75	y = -- r^2 = -- RMSE = --	y = -- r^2 = -- RMSE = --	y = -- r^2 = -- RMSE = --
NLCD	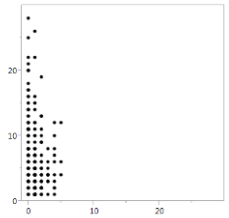	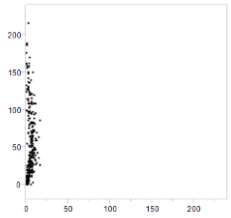	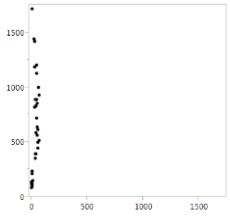	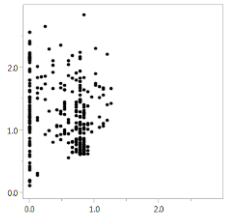	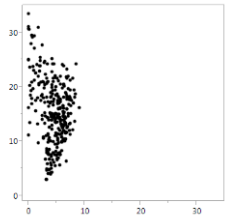	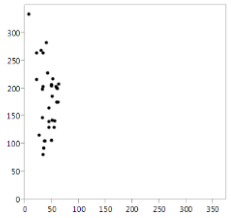
	y = -- r^2 = -- RMSE = --	y = -- r^2 = -- RMSE = --	y = -- r^2 = -- RMSE = --	y = -- r^2 = -- RMSE = --	y = -- r^2 = -- RMSE = --	y = -- r^2 = -- RMSE = --

Figure 5-6a: Regression models predicting number of forest patches and total forest patch edge length. The 30-meter land cover metric value (x-axis) was used to predict the 1-meter metric value (y-axis) for plots with100- and 400-meter radii.

	100	400	1400	100	400	1400
Resample	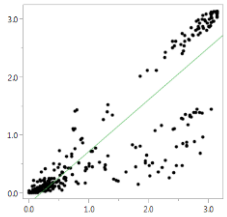	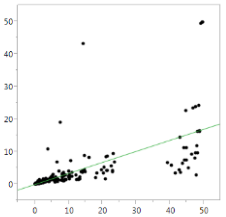	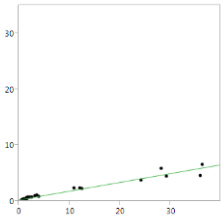	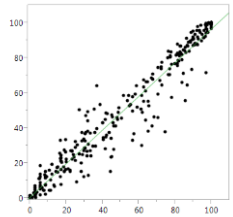	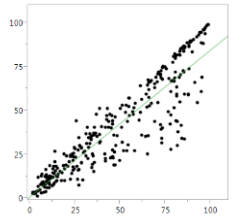	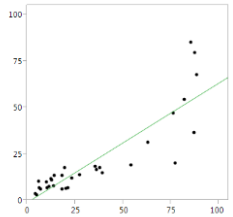
	$y = 0.89x – 0.16$ $r^2 = 0.80$ RMSE = 0.55	$y = 0.34x - 0.02$ $r^2 = 0.47$ RMSE = 4.77	$y = 0.16x + 0.22$ $r^2 = 0.96$ RMSE = 0.38	$y = 0.96x + 0.69$ $r^2 = 0.94$ RMSE = 8.07	$y = 0.84x + 0.88$ $r^2 = 0.82$ RMSE = 11.38	$y = 0.64x – 1.19$ $r^2 = 0.75$ RMSE = 11.03
CCL	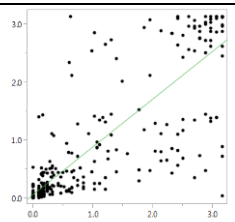	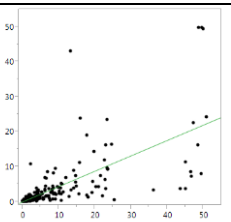	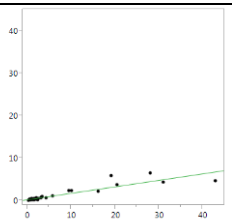	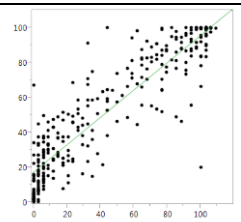	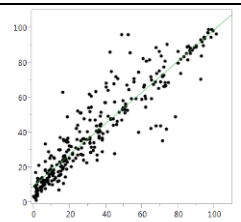	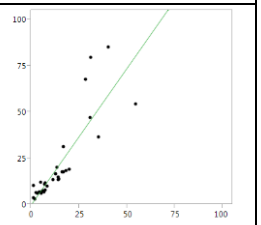
	$y = 0.82x + 0.08$ $r^2 = 0.73$ RMSE = 0.63	$y = 0.44x - 0.06$ $r^2 = 0.49$ RMSE = 4.70	$y = 0.15x + 0.28$ $r^2 = 0.81$ RMSE = 0.78	$y = 0.78x + 17.61$ $r^2 = 0.83$ RMSE = 13.98	$y = 0.89x + 9.85$ $r^2 = 0.85$ RMSE = 10.44	$y = 1.48x – 0.27$ $r^2 = 0.73$ RMSE = 11.54
NLCD	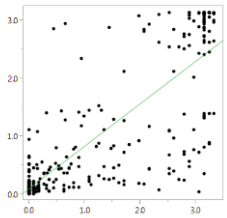	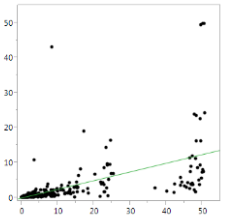	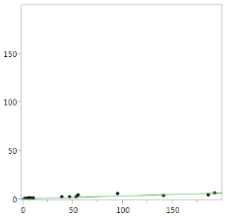	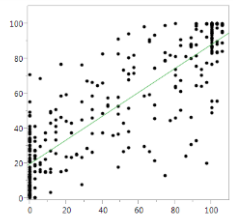	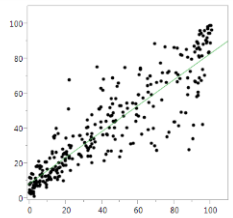	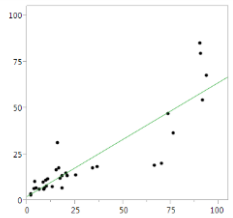
	$y = 0.73x + 0.10$ $r^2 = 0.66$ RMSE = 0.71	$y = 0.25x - 0.09$ $r^2 = 0.33$ RMSE = 5.37	$y = 0.03x + 0.45$ $r^2 = 0.82$ RMSE = 0.76	$y = 0.68x + 20.00$ $r^2 = 0.73$ RMSE = 17.50	$y = 0.74x + 8.88$ $r^2 = 0.80$ RMSE = 12.16	$y = 0.62x + 2.21$ $r^2 = 0.78$ RMSE = 10.51

Figure 5-6b: Regression models predicting number of forest mean patch area and forest largest patch index. The 30-meter land cover metric value (x-axis) was used to predict the 1-meter metric value (y-axis) for plots with100- and 400-meter radii

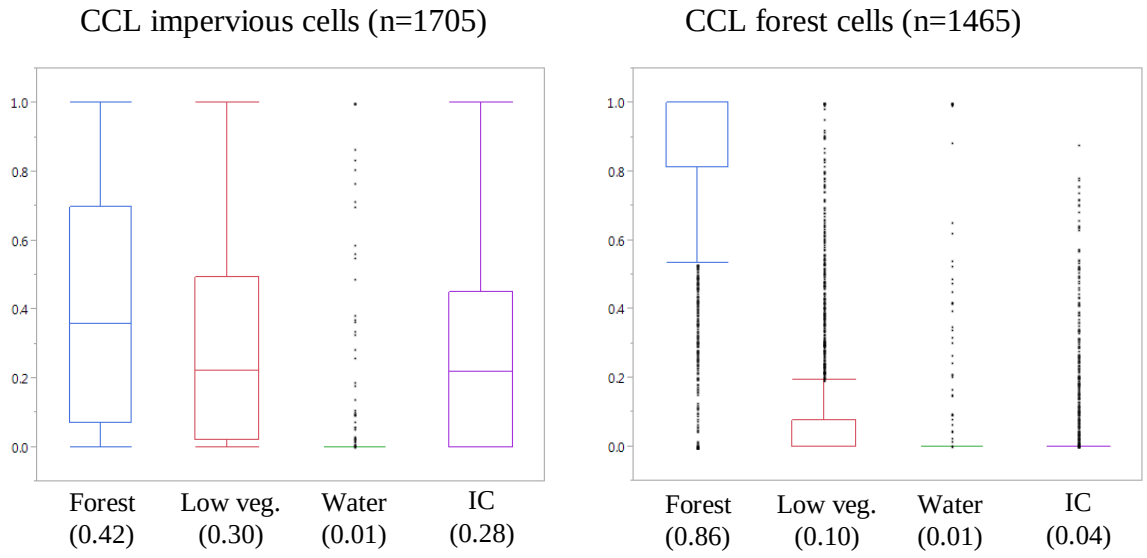

Figure 5-7: Boxplots showing the actual land cover compositions (based on 1-meter resolution land cover) of cells classified as impervious and forest grid cells in the CCL data. Mean values are indicated in parentheses.

5-5. Discussion

In this study, we investigated the ability of Landsat-based land cover data to predict landscape metrics derived from an independent high resolution validation dataset. In contrast, previous studies have used moderate resolution land cover data as the finest resolution dataset and they resampled these data to generate the coarser datasets needed to investigate the effect of scale (see Simova and Gdulova 2012; Alhamad et al. 2011; Liu and Weng 2009). One of the primary needs for studying scale effects is to determine whether coarse resolution land cover, which are readily obtainable for large extents, can be used as a proxy for finer resolution datasets which provide greater detail at the cost of limited spatial and temporal availability. Our study has important implications for the findings of previous research because we found that metrics based on the resampled land cover data tended to behave quite differently from metrics based on independent land cover data of the same resolution. The metrics based on resampled land cover data were excellent predictors of most of the metrics that we tested; however, the metrics derived

from the Landsat-based datasets tended to be much less successful predictors and had different relationships to the validation data. Thus, although previous studies have reported that many landscape metrics, including land cover class fractions, P_{count}, $F_{perimeter}$, $P_{meanArea}$, and LPI, had highly predictable responses as spatial resolution and extent were decreased (Simova and Gdulova 2012; Alhamad et al. 2011; Liu and Weng 2009; Wu 2004; Wu et al. 2002), our findings suggest caution should be used in attempting to calibrate metrics based on trends found in resampled datasets.

The predictability for most of the metrics we tested improved as plot size increased which suggests that the larger analysis area is able to compensate for a coarser cell size. With Landsat-based land cover an analysis area of 3 hectares (100 meter radius) was sufficient for predicting $CF_{impervious}$; however, analysis areas of 50 hectares (400 meter radius) were needed to obtain comparatively good predictions of, CF_{forest}, CF_{lowVeg}, and CF_{core} (Table 5-1). Relatively good predictions of $CF_{perforated}$, CF_{edge}, CF_{patch}, $P_{meanArea}$, and LPI were achieved with analysis areas of roughly 616 hectares (1,400 meter radius). The P_{count} was predicted successfully for the 1,400 meter radius plots with the CCL data but not the NLCD data. We found the CCL and NLCD land cover had a poor ability to predict $F_{perimeter}$ even with the largest analysis area and showed little improvement as the analysis area increased in size.

Table 5-1: Minimum recommended analysis window sizes for landscape metrics

Minimum window size	CCL	NLCD
100 m radius (3.1 ha)	$CF_{impervious}$	$CF_{impervious}$
400 m radius (50.2 ha)	CF_{forest}; CF_{lowVeg}; CF_{core}	CF_{forest}; CF_{lowVeg}; CF_{core}
1400 m radius (615.7 ha)	$CF_{perforated}$, CF_{edge}, CF_{patch}; P_{count}; $P_{meanArea}$; LPI	$CF_{perforated}$, CF_{edge}, CF_{patch}; $P_{meanArea}$, and LPI
Unknown	$F_{perimeter}$	P_{count}; $F_{perimeter}$

The Landsat-based land cover data tended to overestimate $CF_{impervious}$, which was likely due to the tendency of impervious cover to dominate mixed pixels even when impervious surfaces comprised only a minority of the pixel. Cells classified as impervious by CCL tended to be mixed pixels containing significant areas of forest and low vegetation; thus, the vegetation classes tend to be underestimated by the Landsat-based land cover data. Although a larger portion of impervious CCL grid cells tended to be forest rather than low vegetation, the CF_{lowVeg} was less predictable because it comprised a smaller fraction of the overall study area and thus was more strongly affected by the omissions due to mixed pixels. The ability for impervious cover to dominate mixed pixels may be explained by the typically high reflectivity of impervious surfaces in the visible wavelengths. A key spectral characteristic used to identify vegetation in multispectral imagery is its much higher reflectivity of near-infrared (NIR) wavelengths than in red wavelengths (Jensen 2007). However, the presence of impervious cover in a pixel tends to result in relatively high brightness in the red wavelength, which may mask the spectral signature of vegetation even when it dominates the pixel.

The exponential regression models for $CF_{impervious}$ with CCL and NLCD data may be explained by the mixed pixel issue. Once the impervious cover in a pixel is sufficient to dominate the spectral properties, the Landsat-based land cover can no longer register any further increases in the $CF_{impervious}$ for that pixel. Thus, impervious cover is overestimated for areas with low to moderate actual impervious cover; the overestimation declines as the cells become increasingly impervious. Core forest cover is the only other metric that showed a clear exponential relationship between the CCL and NLCD metrics and the validation data. This relationship may be explained by the limited ability of the Landsat to detect small forest gaps caused by features such as rural roads and houses. As the proportion of core forest in the

landscape increases, the relatively small areas of these gaps become less significant compared to the large area of core forest; thus the overestimation from Landsat-based data becomes smaller. In addition, it is possible that these rural roads and houses become less prevalent as the landscape becomes increasingly rural.

The CF_{edge}, $CF_{perforated}$, and CF_{patch} metrics required larger analysis areas in order for the Landsat-based data to be successful in predicting the validation data. The larger analyses areas helped to mitigate the errors resulting from omissions of these forest classes; the omission errors tended to become less significant as the overall class area increased. The CCL and NLCD land cover data had a low ability to detect roads and houses when obscured by the forest canopy and thus the small forest gaps that indicated perforated forest tended to be omitted. The CCL and NLCD data were more effective at identifying the larger gaps that indicate edge forest. Patch forest was likely to be more affected by omissions from mixed pixels because of the small patch sizes and close proximity to impervious land cover. The NLCD data further omitted patch forest because it tended to be classified as developed open space which we excluded from the analysis.

The Landsat-based land cover data had lower success in predicting patch metrics (i.e. P_{count}, $F_{perimeter}$, $P_{meanArea}$, and LPI) than for CF type metrics. The patch metrics are heavily influenced by small forest patches, which were not well represented in the CCL and NLCD data. In addition, the 30-meter land cover datasets tended to overestimate the size of patches because they omit the small forest gaps that would fragment the patches. As the analysis area is increased, the influence of small patches and gaps becomes less significant and the 30-meter land cover data is better able to predict the validation data. Surprisingly, the ability of the resampled land cover data to predict LPI actually declined as the analysis area increased which may indicate that the smaller analysis areas artificially constrained the size of the largest patch; as the

plot area increased, the tendency of the 30-meter data to overestimate patch sizes become more pronounced. This trend was less clear for the Landsat-based datasets possibly because of their tendencies to overestimate impervious cover which may help offset the tendency of coarser data to omit fragmenting features.

The NLCD-based models generally performed more poorly than the CCL-based models for metrics involving vegetated land cover classes. The lower performance is mainly due to our omission of the NLCD developed open space class because it did not distinguish between forest and low vegetation and thus was not comparable to the other datasets. However, NLCD-based models performed on par with the CCL-based models for $CF_{impervious}$, CF_{forest}, and CF_{core} because these metrics were less affected by the omission of the vegetation in the developed open space class. For these metrics, the similar performances between the two independent Landsat-based land cover datasets suggests that the results of this study are likely to be generally applicable to land cover datasets derived from similar sensors and representing forest-dominated rural to urban landscapes similar to those found in the study area.

5-6. Conclusions

This study investigated the potential of landscape metrics, derived from moderate resolution Landsat-based land cover data, to predict metrics based on 1-meter resolution validation data. We compared the performances of models based on two independently derived 30-meter resolution land cover datasets as well as a 30-meter resolution land cover dataset resampled from the validation data. The Landsat-based land cover data tended to be successful in predicting the class fraction type metrics but had less success in predicting patch-level metrics (i.e. number of patches, total edge length, etc.). For most metrics, the performance of models

based on the 30-meter land cover datasets improved as the analysis area was increased which suggests that larger sample areas can help compensate for lower spatial resolutions. The resampled land cover data substantially out-performed the independent 30-meter datasets for each of the landscape metrics we tested. Furthermore, the model relationships based on the resampled data tended to be quite different than the models based on the independent datasets. Previous studies have found that a number of landscape metrics have predictable responses to changes in spatial resolution; however, these studies were based on moderate-resolution land cover datasets that were resampled to generate each of the coarser datasets used in the analysis. Our findings suggest that the use of resampled land cover may not be appropriate for inferring whether data based on coarse resolution sensors are suitable as a proxy for finer resolution data in terms of deriving landscape metrics.

5-7. Acknowledgements

We would like to thank Chadwick Rittenhouse and John Silander for their helpful reviews of this manuscript.

5-8. References

Akasheh, O.Z., Neale, C.M.U., Jayanthi, H. (2008). Detailed mapping of riparian vegetation in the middle Rio Grande River using high resolution multi-spectral airborne remote sensing. Journal of Arid Environments 72(9): 1734-1744. doi:10.1016/ j.jaridenv.2008.03.014.

Alhamad, M., Alrababah, M., Feagin, R., and Gharaibeh, A. (2011). Mediterranean drylands: The effect of grain size and domain of scale on landscape metrics. Ecological Indicators, 11(2), 611–621. doi:10.1016/j.ecolind.2010.08.007

Anderson, B. J. R., Hardy, E. E., Roach, J. T., & Witmer, R. E. (1976). A Land Use and Land Cover Classification System for use with Remote Sensor Data. United States Geological Survey. Available from http://landcover.usgs.gov/pdf/anderson.pdf. Cited 1-Oct-2014.

Antonarakis, A.S., Richards, K. S., and Brasington, J. (2008). Object-based land cover classification using airborne LiDAR. Remote Sensing of Environment 112(6), 2988–2998. doi:10.1016/j.rse.2008.02.004.

Arroyo, L. A., Johansen, K., Armston, J., and Phinn, S. (2010). Integration of LiDAR and QuickBird imagery for mapping riparian biophysical parameters and land cover types in Australian tropical savannas. Forest Ecology and Management 259(3): 598–606. doi:10.1016/j.foreco.2009.11.018.

Avery, T.E., and G.L. Berlin, (1992). Fundamentals of Remote Sensing and Airphoto Interpretation, Prentice Hall, Upper Saddle River, New Jersey. 472 p.

Broadbent *et al.* (2008). Forest Fragmentation and edge effects from deforestation and selective logging in the Brazilian Amazon. Biological Conservation 141: 1745-1757.

Brothers, T. and A. Spingarn. (1992). Forest fragmentation and alien plant invasion of central Indiana old-growth forests. Conservation Biology 6:91–100.

Center for Land Use Education and Research (CLEAR). 2010. CCL Metadata. http://clear.uconn.edu/projects/landscape/data/metadata/2006lc_091508_v2-02_ctstp83.htm. Cited 4-Aug-2014.

Chen, J., S. C. Saunders, T. R. Crow, R. J. Naiman, K. D. Brosofske, G. D. Mroz, B.L. Brookshire, and J. F. Franklin (1999). Microclimate in Forest Ecosystem and Landscape Ecology. BioScience 49(4): 288–297.

Gilmore, M.S., Wilson, E.H., Barrett, N., Civco, D.L., Prisloe, S., Hurd, J.D., Chadwick, C. (2008). Integrating multi-temporal spectral and structural information to map wetland vegetation in a lower Connecticut River tidal marsh. Remote Sensing of Environment 112: 4048-4060.

Goetz, S.J., Wright, R.K., Smith, A.J., Zinecker, E., Schaub, E. (2003). IKONOS imagery for resource management: tree cover, impervious surfaces, and riparian buffer analyses in the mid-Atlantic region. Remote Sensing of Environment 88: 195-208.

Im, J., Jensen, J. R., and Hodgson, M. E. (2008). Object-Based Land Cover Classification Using High-Posting-Density LiDAR Data. GIScience & Remote Sensing, 45(2), 209–228. doi:10.2747/1548-1603.45.2.209

Jin, S., Yang, L., Danielson, P., Homer, C., Fry, J., and Xian, G. (2013). A comprehensive change detection method for updating the National Land Cover Database to circa 2011. Remote Sensing of Environment 132: 159-175.

Jensen, J.R. (2007). Spectral Characteristics of Vegetation. Remote Sensing of the Environment: An Earth Resource Perspective (2nd Edition). Pearson Prentice Hall. Upper Saddle River, New Jersey. 355-408.

Koetz, B., Morsdorf, F., van der Linden, S., Curt, T., and Allgöwer, B. (2008). Multi-source land cover classification for forest fire management based on imaging spectrometry and LiDAR data. Forest Ecology and Management 256(3): 263–271. doi:10.1016/j.foreco.2008.04.025.

Liu, H. and Weng, Q. (2009). Scaling Effect on the Relationship between Landscape Pattern and Land Surface Temperature : A Case Study of Indianapolis, United States. Photogrammetric Engineering & Remote Sensing 75(3): 291–304.

McGarigal, K., S. Cushman, M. Neel, and E. Ene. (2002). FRAGSTATS: Spatial pattern analysis program for categorical maps. Computer software program produced by the authors at the

University of Massachusetts, Amherst. Available from www.umass.edu/landeco/research/fragstats/fragstats.html. Cited 2-Sept-2014.

Miliaresis, G., and Kokkas, N. (2007). Segmentation and object-based classification for the extraction of the building class from LIDAR DEMs. Computers & Geosciences 33(8): 1076–1087. doi:10.1016/j.cageo.2006.11.012.

Parent, J., D. Civco, and J. Volin. (2014). A fully-automated approach to land cover mapping with airborne LiDAR and high resolution multispectral imagery in a forested suburban landscape. ISPRS Journal of Photogrammetry and Remote Sensing. In review (Sept. 2014).

Parent, J., and J. Hurd. (2008). Landscape Fragmentation Tool (LFT) v2.0. Center for Land Use Education and Research. Available from http://clear.uconn.edu/tools/lft/lft2/index.htm. Cited 3-Sept-14.

Simova, P. and K. Gdulova. (2012). Landscape indices behavior: A review of scale effects. Applied Geography 34: 385-394.

Turner, M., R. O'Neill, R. Gardner, and B. Milne. (1989). Effects of changing spatial scale on the analysis of landscape pattern. Landscape Ecology (3): 153–162.

Vogt, P., Riitters, K. H., Estreguil, C., Kozak, J., Wade, T. G., & Wickham, J. D. (2007). Mapping Spatial Patterns with Morphological Image Processing. Landscape Ecology 22(2): 171–177. doi:10.1007/s10980-006-9013-2

Wu, J., W. Gao, and P. Tueller. (1997). Effects of Changing Spatial Scale on Results of Statistical Analysis with Landscape Data: A Case Study. Geographic Information Sciences 3: 30–41.

Wu, J., Shen, W., Sun, W., & Tueller, P. T. (2002). Empirical patterns of the effects of changing scale on landscape metrics. Landscape Ecology 17: 761–782.

Wu, J. (2004). Effects of changing scale on landscape pattern analysis: scaling relations. *Landscape Ecology*, *19*(2), 125–138. doi:10.1023/B:LAND.0000021711.40074.ae

Yu, L., Liang, L., Wang, J., Zhao, Y., Cheng, Q., Hu, L., and Liu, S. (2014). Meta-discoveries from a synthesis of satellite-based land-cover mapping research. International Journal of Remote Sensing 35(13), 4573–4588. doi:10.1080/01431161.2014.930206.

Yates, E.D., D.F. Levia Jr. and C.L. Williams. (2004). Recruitment of three non---native invasive plants into a fragmented forest in southern Illinois. Forest Ecology and Management 190: 119-130.